Department of Biochemical Engineering

University College London

University of London

Imaging Antimicrobial Peptides in Action by Atomic Force Microscopy

Hasan Alkassem

Submitted in partial fulfilment of the requirements for the degree of Doctor of Engineering at University College London

January 03, 2018

I declare that the work presented in this thesis is my own. Where information has been obtained from other sources, I declare this has been clearly indicated in the thesis.

Abstract

Antimicrobial resistance is a challenge facing the world in the twenty-first century with an estimated 10 million deaths by 2050 if no actions are taken. Microbial resistance to drugs is a natural consequence when bacteria develop and adapt genetically to face new challenges including antibiotics. Currently, this development occurs at a higher rate than drug discovery. Hence there is a need for a new generation of antibiotics that kill pathogenic bacteria.

Nature itself provides inspiration for such new antibiotics. For example, our immune system secretes antimicrobial peptides (AMPs), which have been successful agents in killing pathogens with no reported bacterial resistance. Compared with conventional antibiotics, these peptides are larger and more sophisticated biological molecules, which disturb the bacterial membrane, leading to cell lysis.

It is currently costly to extract AMPs from natural resources to be used for fighting infections. Alternatively, synthetic AMPs that mimic natural ones could provide a sustainable cheap weapon against such thread. This also provides a unique opportunity to understand the structure–function relationships of such molecules to optimise these effective, non-toxic antimicrobial properties.

Our collaborators at National Physical Laboratory have designed and synthesised new AMPs from their essential building blocks (amino acids). This thesis describes the use of atomic force microscopy (AFM) as a nanoscale imaging technique for characterising and imaging membrane poration mechanisms of four new AMP systems.

Two of these systems are helical peptides, explained in chapter 3. The third system, explained chapter 4, is a triskelion with three arms of antimicrobial β-sheet peptide that co-assemble to form a hollow antimicrobial capsules. The latter has two possible functions: gene delivery and bactericidal effects. The fourth system, explained in chapter 5, contains two peptide monomers that are designed to co-assemble and form antimicrobial hollow capsids, inspired by the natural viral capsids.

Finally, chapter 6 is a plan for taking these AMPs a step closer to commercialisation, including a business plan for one potential application.

Acknowledgments

Firstly, I would like to heartedly thank my supervisor in London Centre for Nanotechnology, Prof Bart Hoogenboom, for his tireless and continued support and guidance. His scientific approach has made the journey of my PhD possible despite all the challenges and the ups and downs faced throughout the four-years project. I would also like to deeply thank my supervisor in the National Physical Laboratory, Dr Max Ryadnov, whose leadership, enthusiasm, and support was a great inspiration and encouragement for me to achieve this work. I am also grateful to my supervisor in the department of Biochemical Engineering, Prof Daniel Bracewell, for his advices, supervision and support.

I am also extremely grateful to my colleagues, partners and friends who directly helped and collaborated in my research and who showed a great deal of teamwork throughout the project, particularly Dr Angelo Bella, Adrian Hodel, Baptiste Lamarre, Dr James Noble, Dr Alice Pyne, Dr Emiliana de Santis and Alex Yon.

Many thanks also go to all past and present colleagues in my research groups at LCN and NPL for their advices and support including; Bernice Akpinar, Georgina Benn, Dr Aizhan Bestembayeva, Joseph Beton, Luke Davis, Kate Hammond, Philip Haynes, Dr Kwasi Kwakwa, Dr Carl Leung, Dr Dino Osmanović, Dr Edward Parsons, Dr Jascindra Ravi, Dr Santanu Ray, George Stanley and Dr Richard Thorogate.

Also many thanks to my friends and colleagues in the department of Biochemical Engineering who helped, collaborated with and supported me especially during the first year of the project including Tania Chilima, Dr Nicholas Field, Dr Joseph Newton, Dr Anand Radhakrishnan, Dr Gregorio Rodriguez, Dr Michael Sulu, Dr Alex Templar and Jordan Turnbull.

I would like to thank all people who helped me define a business dimension connected to my research, with special thanks to; Prof Simon Hulme, Prof Kamalini Ramdas, Issam Sultan, Yuliana Topazly, Dr Freek Vermeulen, William Woodruf and Haschem Zayed.

Also I deeply thank my flatmate Mr Stephen Constantinou with whom I lived during my PhD. He has provided a very warm incubating space to feel myself at home. His outstanding emotional intelligence to appreciate every single accomplishment I achieved has greatly influenced me, supported me and encouraged me.

I am also profoundly grateful to my family members who have been living with me moment by moment throughout the entire project. Thanks to my wonderful parents (Haytham & Hayfaa`) to whom I humbly dedicate this work, to my brothers Ahmed and Qassem with whom I share my dreams and passion, to my sisters Aisha, Asmaa`, Bayan, Eman, Khawlah and Zainab who were the source of courage and hope.

Finally, I thank Allah, the almighty God, for helping me, inspiring me and guiding me directly and indirectly to collaborate and work with successful people all way throughout my life. I ask him to keep me under his supervision and reward me with the prosperity of life and the hereafter, Ameen.

List of Publications

Valeria Castelletto, Emiliana de Santis, **Hasan Alkassem**, Baptiste Lamarre, James E. Noble, Santanu Ray, Angelo Bella, Jonathan R. Burns, Bart W. Hoogenboom and Maxim G. Ryadnov, Structurally plastic peptide capsules for synthetic antimicrobial viruses. *Chemical Science*, 2016. 7(3): p. 1707-1711.

Emiliana De Santis, **Hasan Alkassem**, Baptiste Lamarre, Nilofar Faruqui, Angelo Bella, James E. Noble, Nicola Micale, Santanu Ray, Jonathan R. Burns, Alexander R. Yon, Bart W. Hoogenboom and Maxim G Ryadnov, Antimicrobial peptide capsids of de novo design. *Nature Communications* 8, 2263 (2017).

Marc-Philipp Pfeil, Alice L. B. Pyne, Valeria Losasso, Jascindra Ravi, Baptiste Lamarre, Nilofar Faruqui, **Hasan Alkassem**, Peter J. Judge, Martyn Winn, Glenn J. Martyna, Jason Crain, Anthony Watts, Bart W. Hoogenboom and Maxim G. Ryadnov, Tuneable poration: host defence peptides as sequence probes for antimicrobial mechanisms. Submitted for publication.

Contents

List of Abbreviations

AFM	Atomic Force Microscopy
AMP	Antimicrobial Peptide
CD	Circular Dichroism
CL	Cardiolipin
DLPC	1,2-dilauroyl-sn-glycero-3-phosphocholine
DLPE	1,2-dilauroyl-sn-glycero-3-phosphoethanolamine
DLPG	1,2-dilauroyl-sn-glycero-3-phospho-(1'-rac-glycerol) (sodium salt)
HEAPS	4-(2-hydroxyethyl)-1-piperazineethanesulfonic acid
IM	Inner Membrane
LD	Linear Dichroism
LMV	Large Multilamellar Vesicle
LPS	Lipopolysaccharides
MALDI-MS	Matrix-Assisted Laser Desorption Ionization-Mass Spectrometry
MIC	Minimum Inhibitory Concentration
MOPS	3-(N-morpholino)propanesulfonic acid
NMR	Nuclear Magnetic Resonance
OM	Outer Membrane
PC	phosphocholine
PE	phosphoethanolamine
PFT	Peak Force Tapping
PG	Phosphatidylglycerol
RP-HPLC	Reversed Phase - High Performance Liquid Chromatography
SLB	Supported Lipid Bilayer
SPPS	Solid Phase Peptide Synthesis
SUV	Single Unilamellar Vesicles
WHO	World Health Organisation

List of Tables

List of Figures

Chapter 1

Introduction

1.1 Antimicrobial Resistance - a Global Challenge

Antimicrobial resistance is considered one of the global challenges facing the world in the twenty first century. The World Health Organization (WHO) has raised this issue as one of its main priorities to be worldly discussed and fought. Many governments, institutions and organisations are getting more engaged to face this major problem. The issue is that many pathogenic microorganisms that used to be killed by the available antibiotics to treat the infections, have become resistant [23]. This resistance shows a real possibility for very common infections and minor injuries to be a cause of death, which is referred to as an entry to a “post-antibiotic era”. In 2012 for instance, it was reported that 480,000 new cases of the multidrug-resistant tuberculosis (MDR-TB) have been identified in more than 100 countries [24]. The WHO and its worldwide partners have set a surveillance platform to track the antimicrobial effectiveness and any potential emergence of resistant microorganisms. The report shows that there are seven multi-drug resistant bacterial stains with global concerns and they are under a constant surveillance. These strains have been reported in more than 60 countries in the world [25].

In fact, microbial resistance to antibiotics is a natural occurrence acquired over time. Resistance against every single antibiotic drug, regardless of the drugs’ mechanisms of action, was reported very soon after the introduction of these drugs to clinical use [26]. Traditional antibiotics are small molecules that inhibit the growth of pathogens by blocking a key (bacterial) cellular pathway in order to prevent infections. The microbial immune system develops and adapts genetically to encounter these challenges. The acquisition of this resistance has been exacerbated due to the misuse and overuse of antibiotics in humans and animals. Some examples are the over-prescribing or the non-completion of the necessary prescribed antibiotic dosage for humans, animals or for farming. In addition, low hygiene standards contribute to spreading resistance to other bacterial strains and to other geographical areas. According the WHO, antimicrobial resistance is now increasing at a higher rate than the discovery of antimicrobial drugs.

The WHO has proposed a plan to tackle and control antimicrobial resistance. This includes a reduction of unnecessary prescriptions of antibiotics. It has also set a worldwide educational programme to eliminate antibiotics misuse by the lay public. In addition, a solution of this problem can be via two main strategies: (1) developing new antimicrobial

agents and (2) searching for smart strategies that can restore or preserve the efficacy of existing antimicrobial agents. Therefore, the WHO urges governments and responsible bodies to stimulate researches to promote antibiotic development.

There is a considerable responsibility on industry and pharmaceutical companies to invest and increase the pace of antibiotic research and discovery. Unfortunately however, antimicrobial development is still an unattractive investment [27]. One reason is that the antibiotics market is not stable and that alternative, commercially more interesting investment opportunities are available [28]. The unstable market of antibiotics, as mentioned in chapter 6, is associated with the waves of infections that target particular areas and the rapid cure of these infections with no continued treatment required. In contrast, chronic diseases and disorders such as hypertension require therapeutic drugs to be used (i.e., implying a continued demand) for decades. Furthermore, the nature of the antibiotic research, the uncertainty of the life cycle for new drugs, the regulatory issues that limit the pace of exploitation, all reduce the commercial attractiveness of the investment in antibiotic development [29].

For this reason, it is believed that the quickest developments of antimicrobial researches will be initiated from the academic and small-to-medium size research laboratories [30]. Consequently, the WHO has suggested a plan to include new ways for stimulating new researches and developments, as we are currently in a race between drug development and microbial evolution [24].

1.2 Bacterial Types and General Structures

Notwithstanding the threat from the pathogenic bacteria, some bacteria play a very useful role in maintaining the health of our planet. According to reported studies, probably only 1% of bacterial species are known and their morphologies vary in shape and size [31]. The most common two shapes are the rod shape and cocci shape. *Mycoplasmais* is a bacterium with a size near the lower end of the spectrum, with ~ 0.3 µm diameter [32]. On the other hand, *Oscillatora*, which is a photosynthesis bacterium, has a 7 µm width and a ~500 µm length [33]. *Escherichia coli (E coli)* is a rod shape bacterium with a typical width of 0.5 µm and length of 2 µm [34].

These bacteria are protected by a cell envelope, which is a quite complex multilayer structure that protects the organism from the external unpredicted environment. In 1884 Christian Gram developed a staining method for bacteria [35]. He found that most bacteria fall into one of the two categories according to the staining of their envelope, Gram-positive or Gram-negative [36].

1.2.1 Gram-negative Bacteria

In Gram-negative bacteria such as *E coli,* the membrane consists of three main layers; the outer membrane (OM), the peptidoglycan cell wall and the cytoplasm inner membrane (IM) [37], figure 1.1. The two membranes are separated by an aqueous space which is called periplasm [38].

The Outer Membrane

The OM in Gram-negative bacteria consists mainly of lipid bilayer like any other biological membrane. However, the study shows that phospholipids only construct the lower leaflet of the bilayer, while upper leaflet is composed of glycolipids, principally lipopolysaccharide (LPS) [39] figure 1.1. The phospholipids making the lower leaflet of the OM are mainly phosphatidyl ethanolamine (PE) and phosphatidyl glycerol (PG).

At physiological conditions, PE is neutral while PG is anionic (i.e., negatively charged at neutral pH). Additionally, LPS is excessively anionic at neutral pH comparing with phospholipids because of the exposed phosphoryl and carboxyl groups, which can readily be ionised [40].

This causes the overall charge of the OM in the gram-negative bacteria to be negative. In addition, the OM includes enzymes [41] and other proteins that are broadly classified into two categories, lipoproteins and β-barrel proteins, figure 1.1.

LPS plays a vital role in the OM as a functional barrier. It has been reported that LPS molecules bind each other avidly and tightly due to the large saturation of the acyl chains. The OM in the Gram-negative bacteria forms an effective and selective permeability barrier [42]. This is due to the role of the tightly packed LPS as a barrier for the hydrophobic molecules, coupled with the fact that proteins limit the diffusion of hydrophilic molecules larger than about 700 Dalton.

The Periplasm and Peptidoglycan Layer

Just underneath the OM, in the periplasm, there is a thin layer of one or two sheets thick called peptidoglycan. This peptidoglycan is composed of repeating units of the disaccharide N-acetyl glucosamine-N-actyl muramic acid cross-linked by pentapeptide side chains figure 1.1 [43] . Because of it rigidity, peptidoglycan has role in maintaining the cell shape. Overall, the periplasm has a higher viscosity than the cytoplasm [44], and it has a role in hiding away any potential harmful degradative enzymes from reaching the IM.

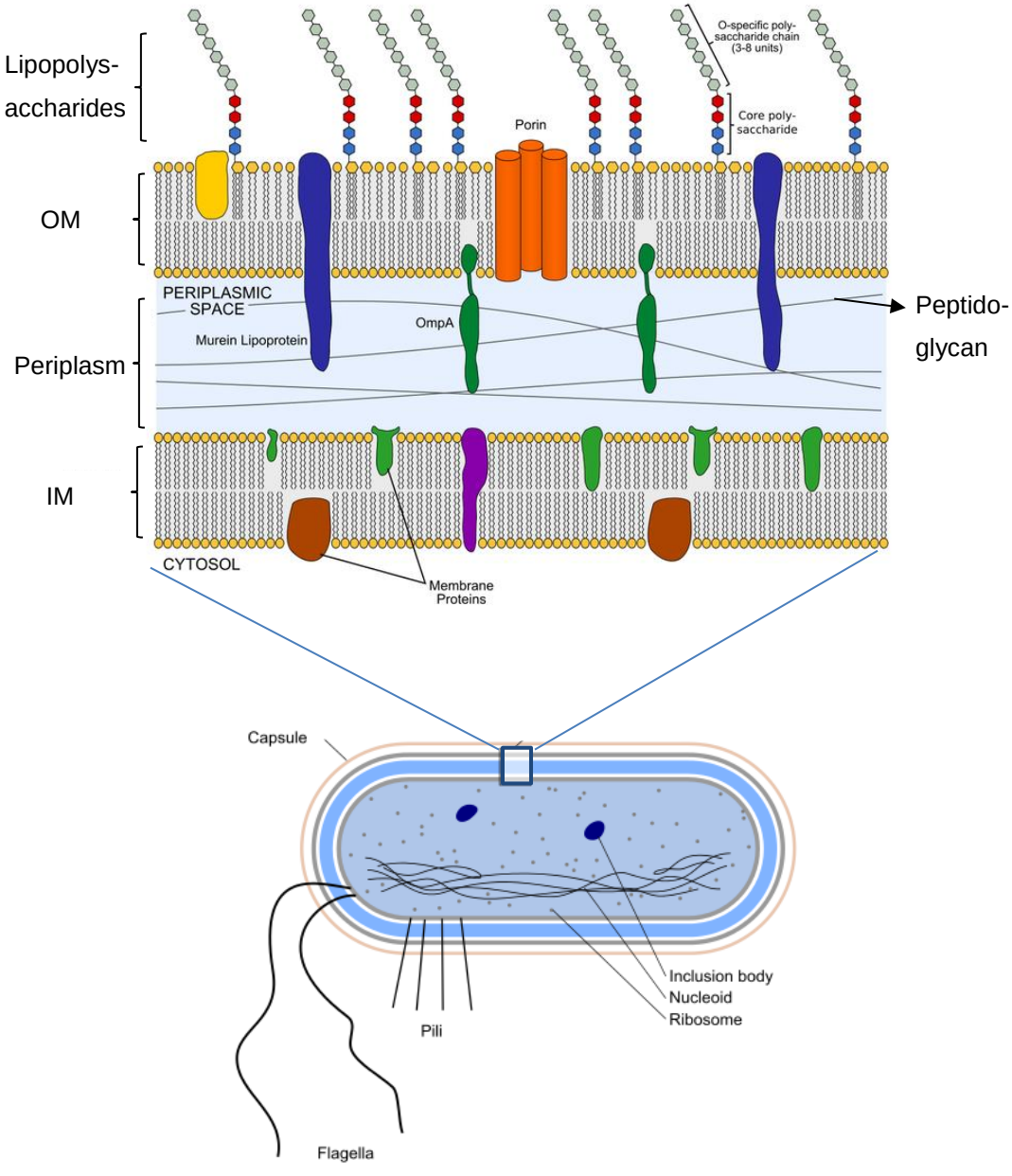

Figure 1.1: Diagram showing the structure of a Gram-negative bacterium with a magnified area on its cell wall. The magnified cell wall diagram highlights the main parts and components which are the outer membrane (OM), the periplasmic space, the inner membrane (IM), the lipopolysaccharides, and the peptidoglycan. Note that the yellow balls on the upper leaflet of the OM are either the phospholipids headgroups or the saccharide rings as parts of the lipopolysaccharides. Image was adapted from Wikipedia (author: Jeff Dahl).

The Inner Membrane

Phospholipids also constitute both leaflets of the IM in Gram-negative bacteria. Similar to the OM, the two main phospholipids making the IM In *E.coli* are PE and PG figure 1.3.

The composition of these two phospholipid types can respectively vary in the mass ratio (PE:PG) from 1:1 to 4:1 [45].

Bacterial cells lack many of the intracellular organelles that are present in eukaryotic cells. For this reason, membrane-associated functions in bacterial cells are performed in the IM. For example, membrane proteins that function in energy production, lipid biosynthesis, protein secretion, and transport are located in the IM [36].

1.2.2 Gram-positive Bacteria

Gram-positive bacteria differ from the Gram-negative by some key aspects. First and foremost, the cell envelope of Gram-positive bacteria only contains a single lipid bilayer. In addition, these bacteria protect themselves from the surrounding environment by a layer of peptidoglycan that is thicker than that found in the periplasmic space of Gram-negative bacteria figure1.2. However, the contents of the peptidoglycan layer in the Gram-positive bacteria *B. subtilis,* for example, is very similar to that found in *E.coli* [46].

Furthermore, there are long anionic polymers, called teichoic acids penetrating through these layers of peptidoglycan, figure 1.2. These are repeats of glycerol phosphate, glucosyl phosphate, or ribitol phosphate [47]. These anionic polymers give the overall anionic charge of the Gram-positive bacterial surface. Finally, the surfaces of Gram-positive microorganisms are decorated with a variety of proteins, some of which are analogous to proteins found in the periplasm of Gram-negative bacteria [48].

The cytoplasmic membrane in the Gram-positive bacteria is also a bilayer, with both leaflets formed mainly by phospholipids [49]. However, here the major phospholipids are phosphatidyl glycerol (PG) and cardiolipin (CL), the headgoups of which are anionic, giving an overall negatively charge to the membrane, figure1.3 [50, 51].

1.2.3 Pathogenic Bacteria

Pathogenic bacteria are highly adapted microorganisms that cause disease. This is due to their ability to survive, multiplicate and colonise host cells or tissues. Pathogenicity can be attributed to common factors, namely the entry, the finding a niche and the avoiding of host defence mechanisms [52]. For the entry, there is a belief that it is a matter of probability for pathogenic bacteria to enter the host, over which it has a little control.

Successful pathogen must find a suitable niche and multiply or at least survive there. There are many mechanisms employed by the bacteria for different environments and host

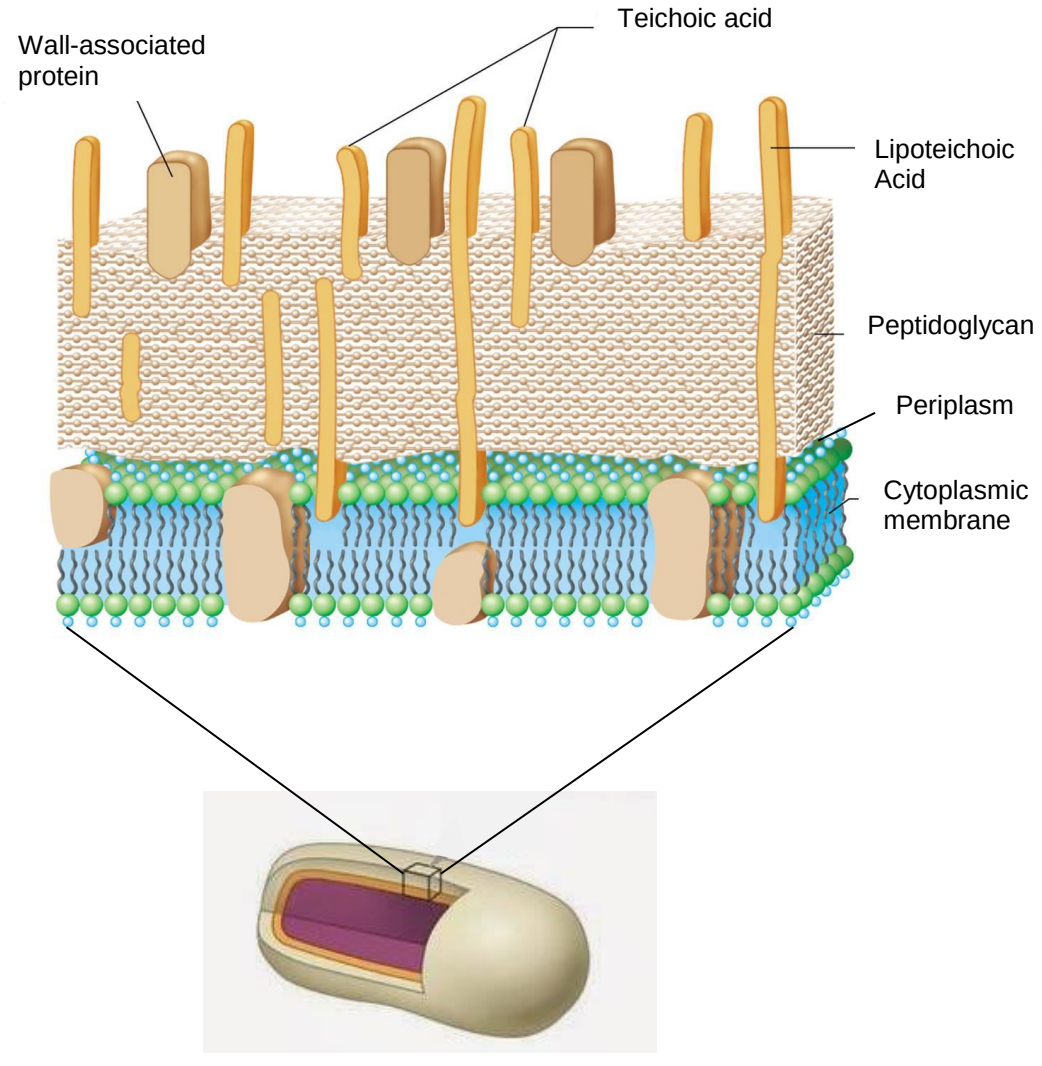

Figure 1.2: Diagram showing the structure of a Gram-positive bacterium with its cell wall magnified. The main parts and components of the cell wall are the peptidoglycan layer, the periplasmic space, the cytoplasmic membrane, lipoteichoic acids, teichoic acids and wall-associated proteins. Image reproduced from Pearson Education, Inc.

surfaces [53]. Host defence mechanisms are considered the most difficult for the pathogen to overcome. These mechanisms employ natural immune responses by the hosts to encounter any dangerous microorganism trying to invade or localise [54].

Pathogenic bacteria therefore possess a counterstrategy for these responses to avoid, disrupt or reverse these protective secreted agents. The longer the bacteria can protect itself to reach their niche and multiply, the more probable they are to succeed in multiplying and ultimately causing the disease. Some of the best known mechanisms for countering the host defences are antiphagocytic capsules, toxins that target host immune cells [52], and the synthesis of immunoglobulin-specific proteases [53].

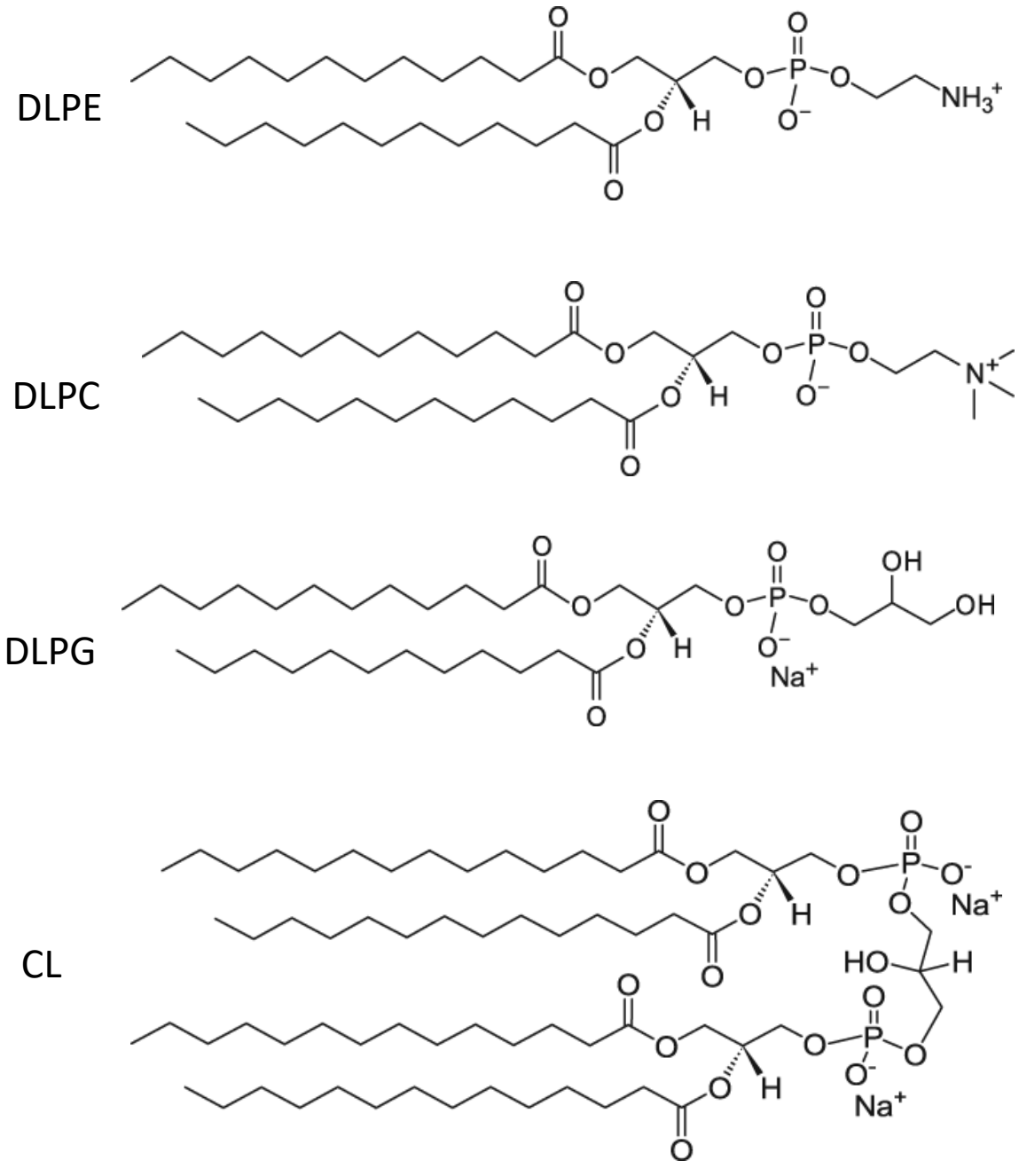

Figure 1.3: The chemical structure of the neutral and anionic phospholipids. DLPE and DLPC are neutral while DLPG and CL are anionic. Structures were taken from lipids catalogues of Avanti® Polar Lipids, Inc.

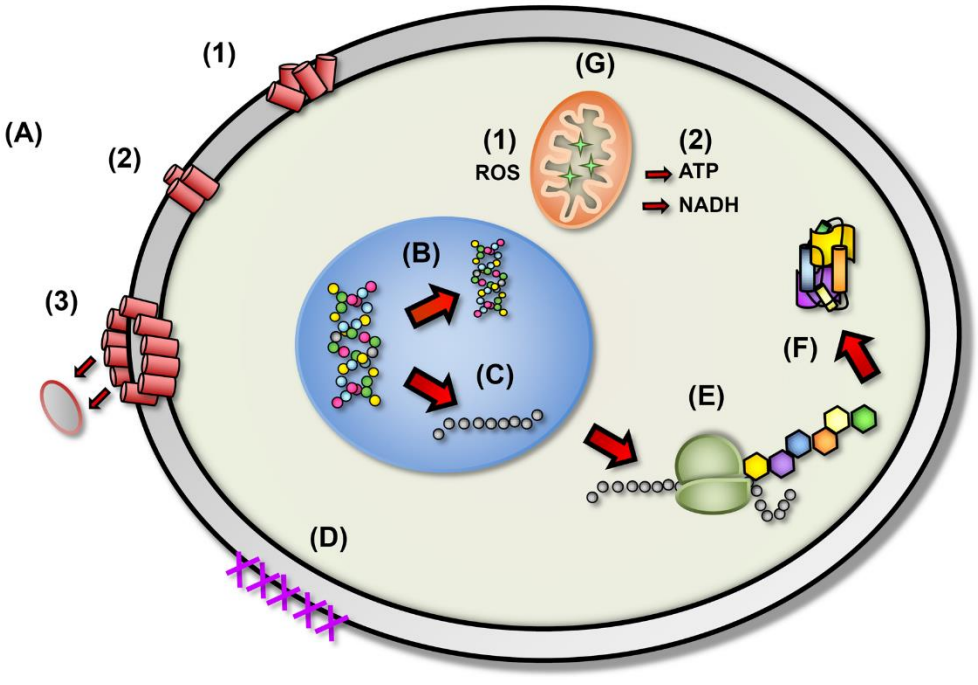

Figure 1.4: Mechanistic modes of action for antibiotics in bacterial cells. (A) Disruption of cell membrane. (B) Inhibition of DNA synthesis. (C) Blocking of RNA synthesis. (D) Inhibition of enzymes necessary for linking of structural proteins in the cell wall. (E) Inhibition of ribosomal function and protein synthesis. (F) Blocking of chaperone proteins necessary for proper folding of proteins. (G) Targeting of mitochondria. Figure was reproduced from reference [14].

1.3 Antibiotics Targets and Mechanisms of Bacterial Resistance

In 1904, Paul Ehrlich started a screening program to find a drug against syphilis, which was a widespread and almost incurable disease at that time.

The disease is caused by a bacterium called *Treponema pallidium.* In 1910, Ehrlich successfully discovered an effective drug to treat syphilis, called Salvarsan. Antibiotic discoveries then carried on with Josef Klarer and Fritz Mietzsch synthesising Prontosil in 1930s, followed by Penicillin in 1940s [55].

The discovery of these first three effective antimicrobials, Salvarsan, Prontosil and Penicillin, inspired for further discoveries of antibiotics between the 1950s and 1970s. However, no new classes of antibiotics have been discovered since then [55].

Generally, antibacterial therapeutics act upon bacteria by targeting a process that is essential for the bacterial cells survival or the growing cycle. Based on the effect on these functions, antibiotics can either kill bacteria (bactericidal drugs) or inhibit its growth (bacteriostatic drugs).

Most of the current bactericidal antimicrobials work by inhibiting DNA, RNA, cell wall or protein synthesis which are necessary for the bacterial cell life cycle [56]. In addition, peptide based antibiotics such as polypeptides or lipopeptides target the cell membrane leading the cell lysis [57]. Figure 1.4 summarises these antimicrobial targets within the bacterial cells. In addition, a list of the common classes of available antibiotics and their mode of actions are summarised in table 1.1 [58].

Bacteria are living and genetically dynamic organisms that have the ability to overcome new challenges caused by antibiotic treatment. In fact, resistant bacterial stains were found even before the antibiotics era, when heavy metals were used to treat infections [59]. Figure 1.5 shows a proposed resistance mechanisms employed by a Gram-negative bacterium to protect itself from antimicrobial attacks [6]. Whether the antimicrobial target is on the bacterial membrane or in the cytoplasm, bacteria have developed ways to deactivate such threats. For example, bacteria can change the composition of their membranes to make them more rigid or impermeable [60].

In addition, bacteria can develop a multidrug resistance efflux pumps. These pumps secrete antibiotics from the cell, figure 1.5b. For antibiotics that target organelles in the cytoplasmic, bacteria can make resistant mutations of the targeted receptors, which deactivate the antibiotic, figure 1.5c. Finally, bacteria can disable antibiotics by covalent modification to lose their active sites, figure 1.5d.

What exacerbates the bacterial resistance challenge is that these resistance genes are found to be horizontally transferable. This means that these genes can mobilise in between bacteria of the same or different species [61].

1.4 Alternatives to Traditional Antibiotics

It is clear that, with the rise of bacterial resistance, long-term alternative therapies to combat antibiotic-resistant bacteria are needed. These alternatives could be defined as non-compound approaches (products other than classic antibacterial agents) that target bacteria. There has been progress in developing approaches like antibodies, probiotics, and vaccines, which are currently in phases 2&3 clinical trials [62]. In addition, antimicrobial peptides (AMPs) which are also termed “host defence peptides” hold a great promise to counter the resistant bacteria. AMPs are produced by every living organism [63] and considered important natural defence strategy against invading pathogens [64, 65].

Antibacterial classes	Mode of action
Penicillins, cephalosporins, carbapenems, monobactems, glycopeptides, polypeptides	**Cell-wall construction inhibitors** of peptidoglycan synthesis or cross-linking functions, resulting in osmotic lysis
Lipopeptides, polypeptides	**Cell-membrane disrupters** altering the structure and function of the cell membrane, thus causing cellular leakage.
Aminoglycosides, tetracyclines	**Protein synthesis inhibitors** binding to the 30S ribosomal subunit, thus preventing translation initiation and tRNA binding
Macrolides, oxazolidinones, streptogramins, phenicols	**Protein synthesis inhibitors** binding to the 50S ribosomal subunit, thus disrupting translocation and peptidyl transferase activity
Rifampin	**RNA synthesis inhibitors** preventing the synthesis of mRNA by binding to DNA-directed RNA polymerase
Quinolones	**DNA synthesis inhibitors** preventing DNA replication by binding to the topoisomerase IV or DNA gyrase
Trimethoprim	**Folic acid metabolism inhibitors** preventing the synthesis of nucleotide bases by blocking the synthesis of tetrahydrafolate
Sulfonamides	**Folic acid metabolism inhibitors** inhibiting nucleic acids synthesis by preventing the synthesis of folate

Table 1.1: Antibiotics classes and their modes of action [58]

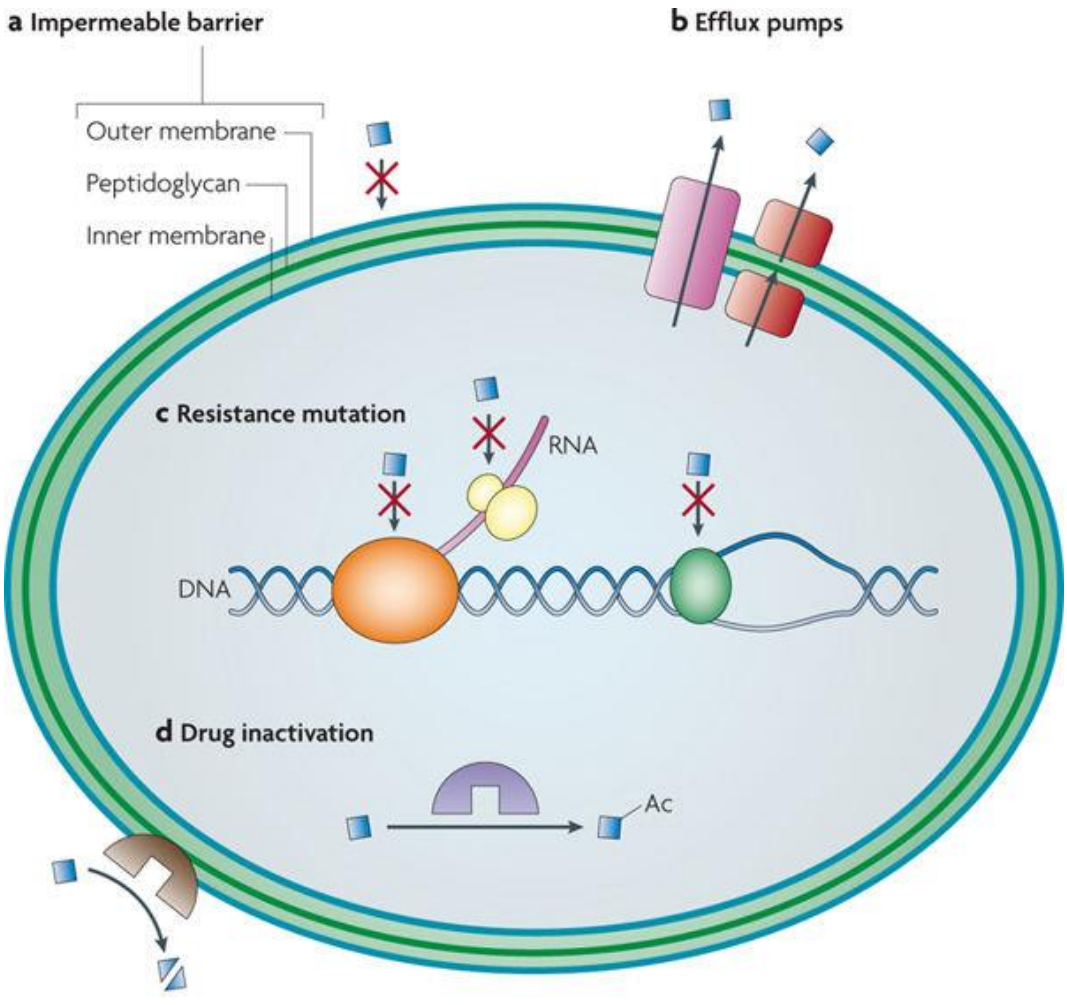

Figure 1.5: proposed mechanisms employed by bacteria to resist antibiotics. (a) Impermeable barriers. (b) Multidrug resistance efflux pumps. (c) Resistance mutations. (d) Inactivation of the antibiotic. Figure was reproduced from reference [6].

1.5 Antimicrobial Peptides

In 1980, two cationic AMPs, cecropin A and B, were isolated and identified in hemolymph of silk moths. They were considered as the moths' primary weapons of defence against pathogens. Over the last three decades, researchers have identified more than 2000 AMPs from animals, fungi, plants and bacteria [66].

Although these AMPs share a number of common features and a limited number of structural motifs, their sequences, activities, and targets differ considerably. In general, natural AMPs are ribosomally expressed and typically range from 12 to 50 amino acid residues [67]. They are often produced as an inactive form that can next be converted into an active antibacterial form [67]. While the majority of these peptides are characterised as cationic or amphipathic,

anionic peptides were also reported with a considerable antimicrobial activity under specific conditions [68].

All AMPs have an abundance of the cationic amino acids such as arginine (R) and lysine (K) [69]. These residues are responsible for the net positive charge on these molecules at neutral pH [70]. In addition, AMPs usually contain a high proportion (up to 50 % or more) of hydrophobic amino acids [71]. These two features (positivity and hydrophobicity) direct AMPs to fold into amphipathic secondary structures upon interaction with bacterial membranes. Their folded structures are characterised by the segregation of the hydrophobic residues into one face of the molecule and the cationic and polar ones into the opposite face [72].

AMPs are typically unstructured in aqueous solution, but they adopt the intended secondary structure when interacting with bacterial cell membranes or their mimetic [72]. As shown in figure 1.6, typical secondary structures of AMPs could be α-helical, β-sheet, extended and looped structures [4].

The adopted secondary structure of AMPs can be investigated by various techniques. The most frequently employed are circular dichroism (CD) [73], oriented circular dichroism (OCD) [74], linear dichroism (LD) [75] and solution state NMR [76, 77].

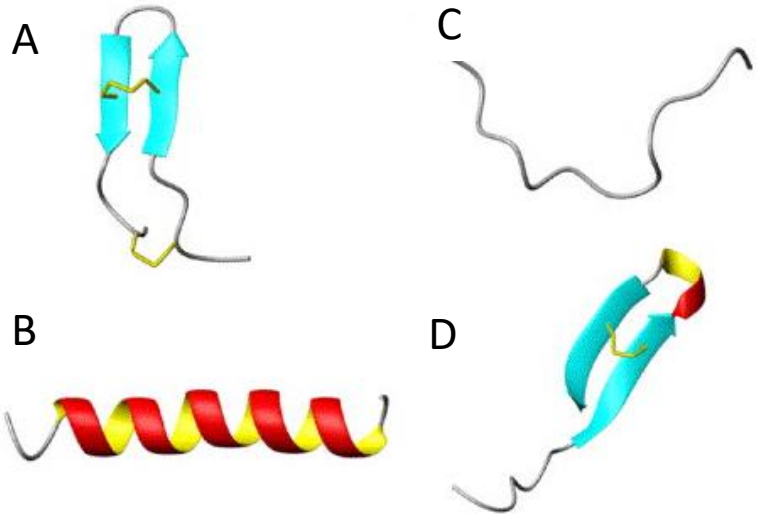

Figure 1.6: Structural classes of antimicrobial peptides: (A) β-sheet, tachyplesin I. (B) α-helical, magainin 2. (C) Extended, indolicidin. (D) Loop, thanatin [56]. Disulfide bonds are indicated in yellow. Figure reproduced from reference [4]

AMPs have been reported act in numerous, different ways, implying that there is no common mechanism for all AMPs. A common feature, however, is that cationic AMPs are electrostatically attracted to the anionic LPS and lipoteichoic acids found on the surface of Gram-negative and Gram-positive bacteria, respectively. Such interactions are considered the first contact which could lead AMPs to pass through this external cell walls and to reach the cytoplasmic membrane. Once AMPs pass though the external cell wall, they preferentially interact with the anionic phospholipids that form the cytoplasmic membrane, such as phosphatidylglycerol and cardiolipin [78].

When AMPs reach the bacterial cytoplasmic membrane, and due to their amphipathic structures, they are able to insert and disrupt the membrane via different mechanisms, as shown in figure 1.7. The common models describing such mechanisms are the “barrel-stave model” [79], the “toroidal-pore model” [79], the “aggregate model” [80] and the “carpet model” [81].

Toroidal and barrel-stave for example, are both pores forming models as shown in figure 1.7. The toroidal model differs from the barrel-stave model in that the peptides are always associated with the lipid headgroups even when they are perpendicularly inserted in the lipid

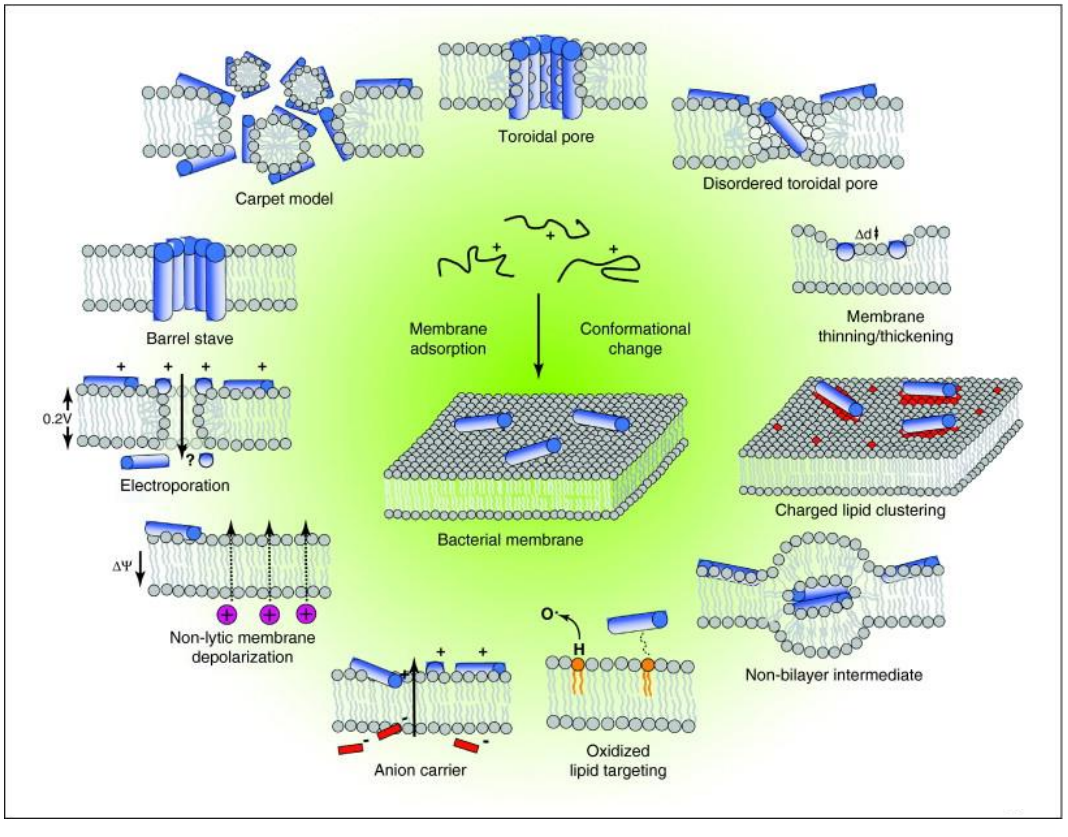

Figure 1.7: Events occurring at the bacterial cytoplasmic membrane following initial antimicrobial peptide (AMP) adsorption. Figure reproduced from reference [11]

bilayer. In forming such a pore via the toroidal model, the lipid monolayer bends continuously from the top to the bottom in the fashion of a toroidal hole. This makes the pore lined by both the peptides and the lipid headgroups.

Although AMPs commonly interact with and damage the bacterial external wall and cytoplasmic membranes of bacteria, it is yet not fully clarified how these interactions lead to bacterial cell death. Recently, there has been speculation that transmembrane pore formation is not the only mechanism of microbial killing. In fact, several observations suggest that translocated peptides can alter cytoplasmic membrane formation, inhibit cell-wall synthesis, inhibit nucleic-acid synthesis, inhibit protein synthesis or inhibit enzymatic activity [82-84]. In this context, it is worthwhile to note that, in bacteria, these activities take place on the membrane, as discussed earlier.

The diversity in membrane disrupting mechanisms and intracellular targets causes AMPs to be a rather generic threat for bacteria, not relying on too specific interactions that would facilitate evasion by few mutations [85]. For this reason, AMPs are considered to be excellent candidates for further development as a new class of antimicrobials to combat the emerging threat of multidrug-resistant bacteria [86].

1.7 Engineered and Synthesised Antimicrobial Peptides

Early studies of AMPs relied on the extraction and purification of peptides from natural sources, and then testing their antibacterial activity. The drawback of this approach is that it requires a large amount of raw biological sample to obtain modest quantities of peptides [87]. In addition, natural AMPs are usually translated as larger proteins which then are cleaved to produce the peptide in its active form [88, 89]. This post-translational process in secreting the natural AMPs makes it very challenging and costly to purify from natural sources as the desired peptide may not be present in a unique and/or active form.

Fortunately, chemical synthesis of peptides has quickly become an alternative method for obtaining AMPs at high purity and yield. As will be explained in chapter 2, solid-phase peptide synthesis (SPPS) is now widely employed to produce large quantities of peptide [90].

Since the antimicrobial action of these peptides is directly associated with its amino acid sequence, the effectiveness of synthetic peptides should be identical to the natural ones when the sequence is the same. In fact, this chemical synthesis enables the production at reasonable price.

In addition, chemically synthesised peptides have many additional advantages. Since the synthesis occurs gradually by sequentially adding amino acids to the growing peptide chain (as explained in chapter 2), the method allows researchers to precisely modify AMP sequences. Such modifications can lead to AMPs with modified antibacterial activity and more importantly, they help in investigating the structure-activity relationships that may guide the development of more potent antibiotics.

Such modifications are not limited to the use of the 20 naturally occurring amino acids; non-natural amino acids can also be added into the AMP sequence to improve the activity and stability. Furthermore, it is possible to include synthetic peptidomimics such as sequences consisting of β-amino acids [91] or D-forms of AMPs [92]. These peptidomimics retain the intended antimicrobial activity of the parent AMP molecule with additional imperviousness to proteolytic degradation by enzymes [93].

Over the last two decades, there has been significant progress in engineering and designing nanostructured materials with a clear potential for commercialisation [94]. Self-assembling peptides provide flexible solutions to devise such materials with programmed biological functions [95]. One function, beside antimicrobial action, could be gene and drug delivery as a promising solution to counter diseases and promote the longevity of human life [96]. Scientists revealed the possibility to program two functions such as gene delivery and bactericidal activity within one finely devised nanostructure [2].

1.8 Atomic Force Microscopy for Studying AMPs Mechanisms

As mentioned above, there are a number of tools to characterise the modes of action of AMPs. In that context (and in the context of this thesis), a particularly interesting characterisation tool is atomic force microscopy (AFM), as it can visualise the effect of AMPs on the bacterial or model membranes with ~1 nm spatial resolution. Compared to other imaging techniques, it also has the advantage of being able to image the biological samples in liquid, i.e. in similar conditions to their native environments, facilitating the study of AMPs in action.

1.8.1 Imaging AMPs and their Effects on Bacterial Cells by AFM

To date, AFM investigations of AMPs effect on bacterial cells have largely been conducted in air [10, 16, 97, 98]. The AFM images in such studies revealed changes in bacterial cell height and surface roughness upon incubation with AMPs. Figure 1.8 shows an example of a study conducted to investigate the effect of AMPs called Sushi peptides (S3) on *P. aeruginosa* bacterial cells [10]. In this study, different samples were prepared by mixing the cells with the S3 AMP at different concentrations or incubation times.

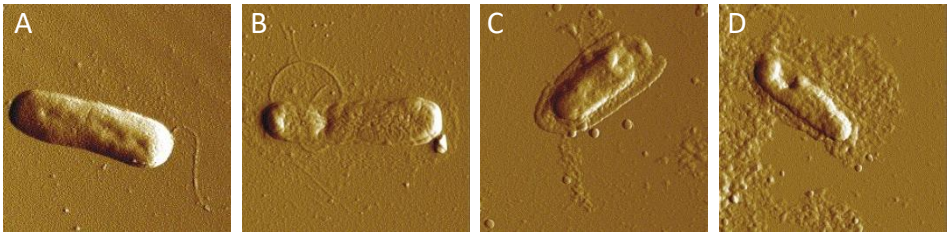

Figure 1.8: AFM images in air of *P. aeruginosa* bacterial cells treated with S3 AMP. (A) Image of untreated bacteria. (B) Indentations and outer membrane debris of *P. aeruginosa* treated with 0.25 μM of S3 for 15 min. (C) Small amount of leakage of periplasmic fluid of *P. aeruginosa* treated with 0.25 μM of S3 for 30 min. (D) Extensive leakage of cytoplasmic fluid of *P. aeruginosa* when exposed to 5 μM of S3 for 1 min. Figure reproduced from reference[10].

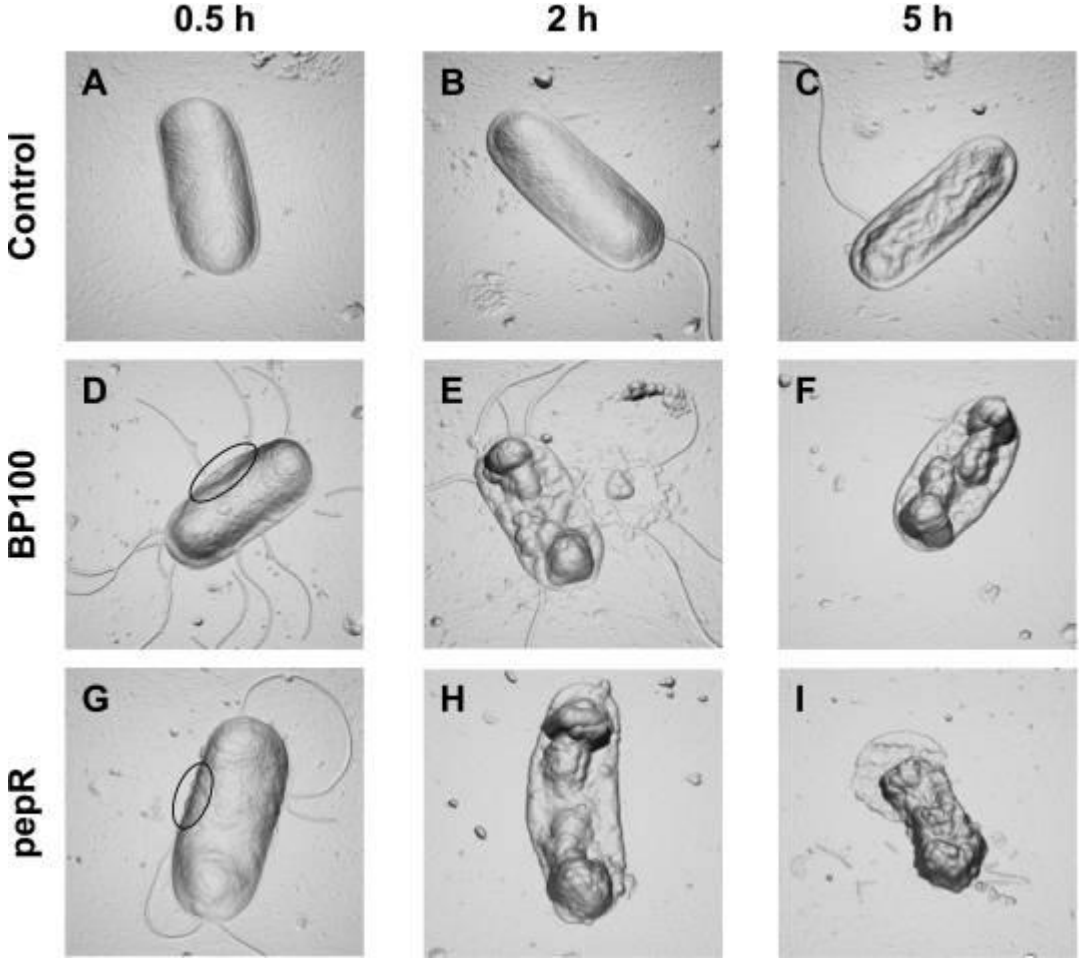

Figure 1.9: Time dependence of AMP effects on *E. coli* imaged by AFM. *A–I*, three-dimensional orthogonal projection images (derived from the height data) of untreated *E. coli* cells (*top row*), and *E. coli* cells treated with 3 μM BP100 (*middle row*), and 5 μM pepR (*bottom row*). Images were acquired following the treatment of the bacterial cells for 0.5 h (*first column*), 2 h (*second column*), and 5 h (*third column*). Total scanning area for each image: 4 × 4 μm. Figure reproduced from reference [16]

Next, bacterial cells were dried on the substrate to be imaged by AFM. In another study, shown in figure 1.9, an investigation of the effect of two AMPs (BP100 and pepR) was conducted on *E. coli* bacterial cells. Although the AFM images in both studies have revealed defects in the bacteria membranes and changes in the cells morphologies as the results of AMPs exposure, they only provided limited insight into AMP mechanisms. This is because sample drying can also affect the morphology of the bacterial cells and because in air AFM does not allow to track the effect of the AMPs while they attack the bacteria.

AFM has also been used to image bacterial cells in liquid [13, 99, 100]. Provided that such imaging is done as sufficient spatial and temporal resolution, this may answer many questions about the effect and mechanisms of AMPs and other antibacterial agents. However, high resolution in liquid AFM of bacterial cells is challenging. This is due to the difficulty in immobilising live bacteria on the AFM substrate, due to the large variation in morphology of the bacterial cell and due to the risk of contamination of the AFM tip during the imaging process or artefactual differences in bacterial height due to differences in the adhesion forces between the AFM tip and the bacterial surface [101].

Several methods have been used to immobilise and fix bacterial cells for imaging in liquid [102]. These include using glutaraldehyde, formalin, paraformaldehyde, methanol/acetone (1:1) and ethanol/acetic acid (3:1). It was reported that these agents can effectively preserve the bacterial cell morphology but they are also likely to change the cell wall structure [102].

As explained in section 1.2.1, the outer membrane of Gram-negative bacterial cells is an asymmetric bilayer composed of two leaflets. The inner leaflet is formed by phospholipids and the outer leaflet mainly by LPS which is the first target for antimicrobial agents. It was reported that the LPS layer can form phase separations as it exists in liquid-expanded (LE) and liquid-condensed (LC) domains.

Figure 1.10 shows time-lapse AFM imaging of *P. aeruginosa* in liquid to monitor the morphology change as a result of incubation with the antimicrobial aminoglycoside agent (neamine) [13]. The cell's height was reduced 50% over the course of experiment (35 min), shown in the lower panel of figure 1.10. However, the spatial resolution was insufficient to reveal information about the membrane disruption mechanism.

In 2010, Fantner et al. used high-speed AFM imaging to study the kinetics of cell death of individual *E. coli* bacterial cell after the exposure to the pore-forming and membrane-disrupting AMP CM15 figure 1.11 [12].

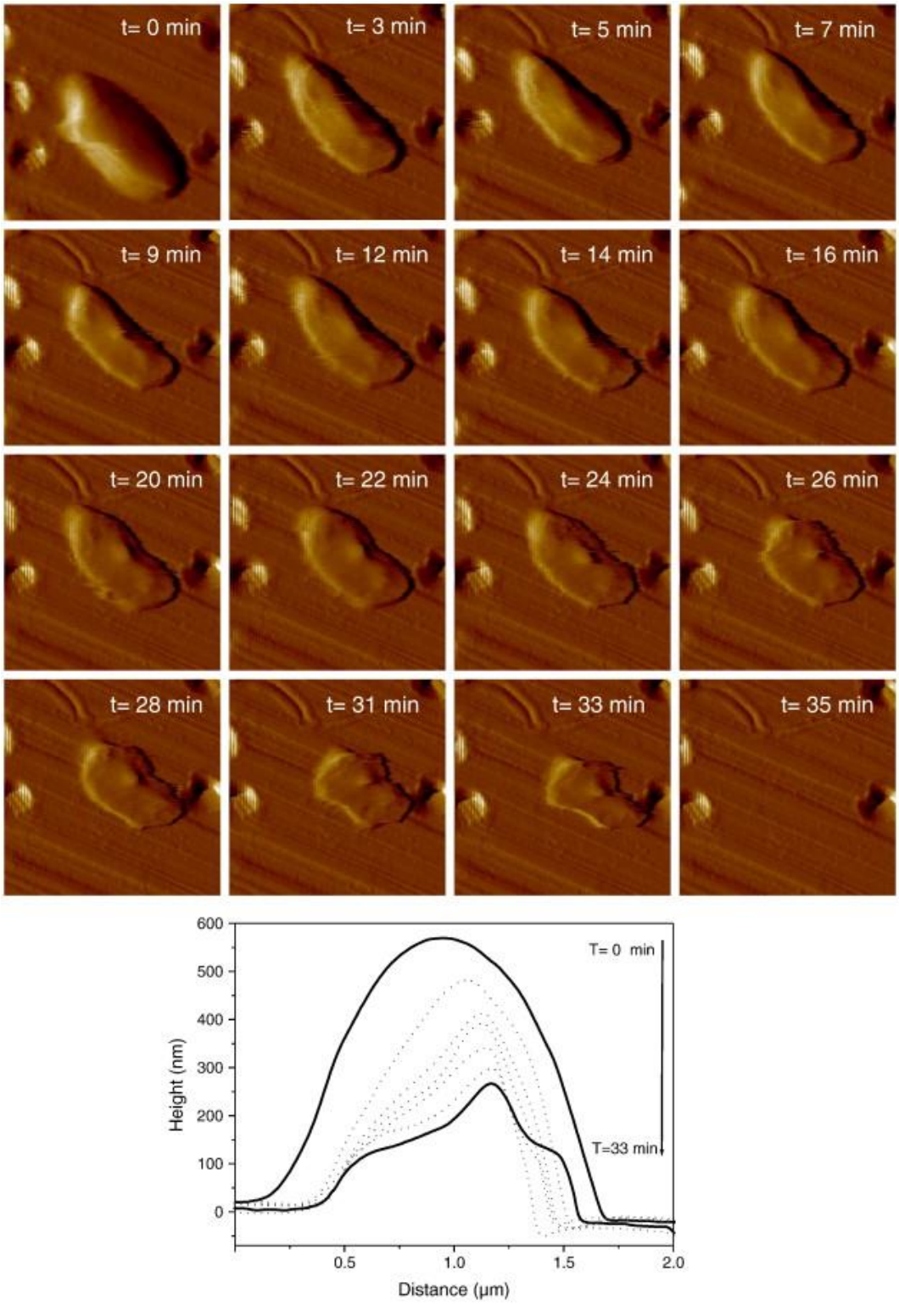

Figure 1.10: In liquid AFM imaging of single *P. aeruginosa* cell following incubation with 3′,4′,6-tri-2NM neamine at 0.5-fold MIC. Deflection images (3 μm × 3 μm) recorded in real time for a single cell prior and after treatment is shown. The lower panel compares vertical cross-sections.Figure was reproduced from reference [13]

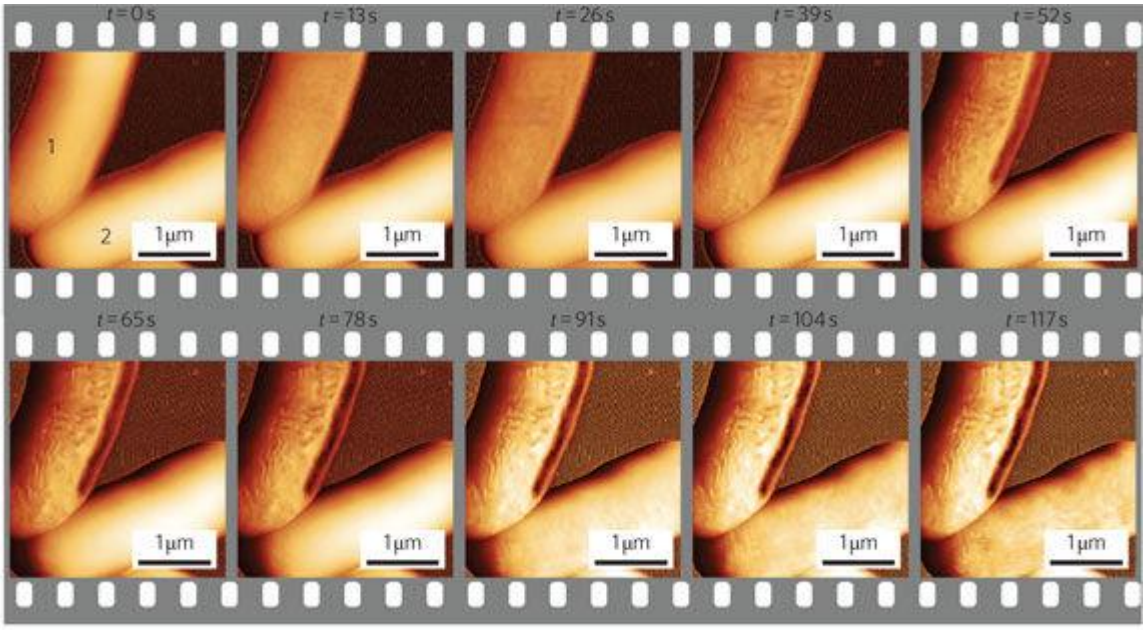

Figure 1.11: AFM imaging of *E.coli* incubated with CM15 antimicrobial peptide. CM15 injected at $t = -6$ s and images recorded every 13 s, with a resolution of 1,024 × 256 pixels and a rate of 20 lines s^{-1}. The surface of the upper bacterium (1) starts changing within 13 s. The lower bacterium (2) resists changing for 78 s. Images were recorded in liquid in tapping mode with a tapping frequency of 110 kHz. Phase images are shown here for high contrast. Figure was reproduced from reference [12].

The images show the gradual change in the bacterial membrane from smooth to corrugated. Their results suggested that the process of E. coli cell death is a combination of an incubation phase (taking seconds to minutes) and a more rapid execution phase. This mechanistic information is unattainable in traditional AFM imaging studies and is an exciting new approach to the study of AMPs. However, the spatial resolution again was not high enough to demonstrate details about the pores formed by the peptide such as the depth and whether they are static or expanded literally over time.

Recently on the other hand, Alice Pyne et al. acquired a better resolution imaging of live bacteria incubated with an AMP (tilamin) [22]. Figure1.12 shows time-lapse AFM images over ~ 10 min on *E. coli* bacterial surface when incubated with tilamin. The AFM images indicate local removal of the bacterial outer membrane over larger areas, and suggest the presence of few-nanometre diameter holes with 2 nm depth, consistent with poration of the upper leaflet of the lipid bilayer in each membrane [22].

The results were consistent with the effect of the same peptide on a supported lipid bilayers (bacterial model membrane) as will be explained in chapter 3. Taken together with data obtained by other techniques, the AFM images indicated a poration mechanism in which helical peptides adopt a tilted orientation within the membrane [22].

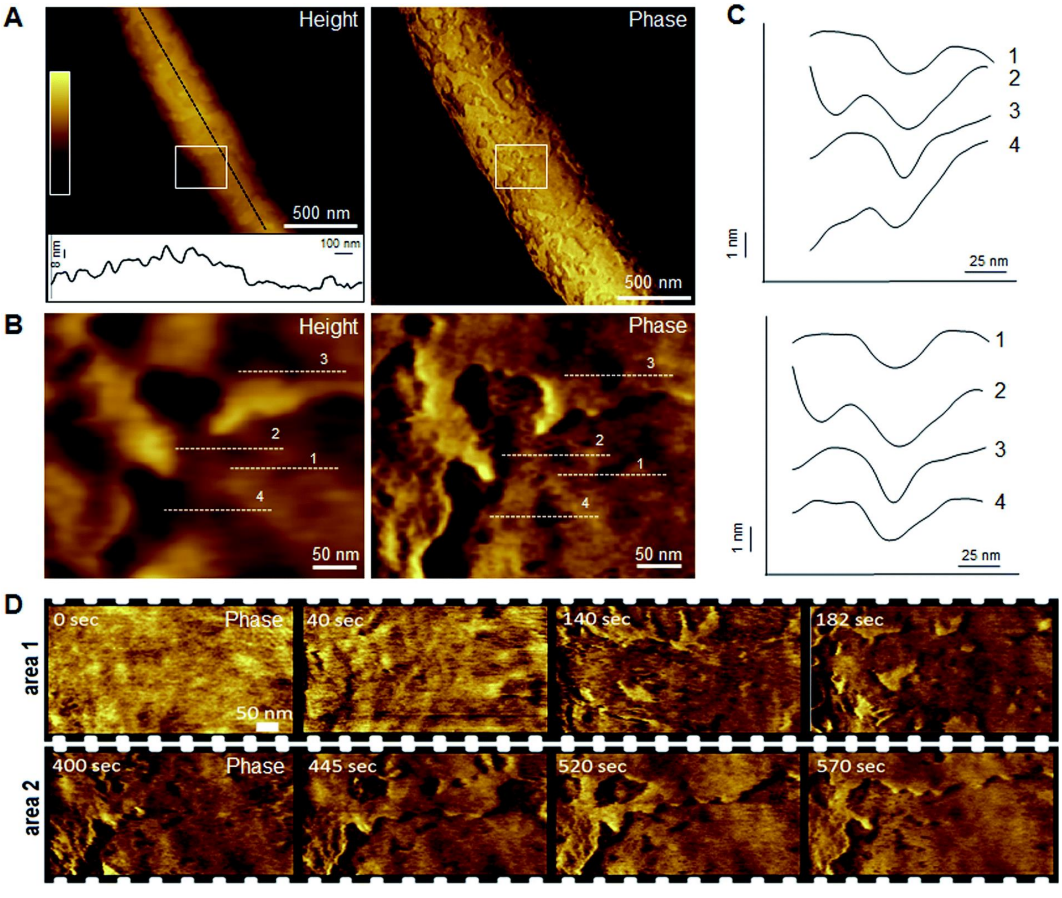

Figure 1.12: AFM imaging of progressive membrane removal in live bacteria incubated with tilamin AMP. (A) Topographic (height) and phase AFM images of live *E. coli* in water taken during the first 780 s of incubation with tilamin. Inset in height image: a height profile taken along the black dotted line on the back of the bacterium, showing 8 nm-deep steps from the outer cell-wall layer to the inner membrane. (B) High resolution topographic and phase images of the areas marked by white boxes in (A). (C) Height profiles taken along the highlighted lines in (B) (top), and after additional local background subtraction (bottom). These data show the depth profiles of individual pores. (D) High resolution phase images of *E. coli* during incubation with tilamin, as a function of time. Two different areas are shown. Time-point labels indicate time since injection. Colour scale for height data, see (A) 140 nm (A) and 19 nm (B). Incubation conditions: 3.5 μM, pH 7.4, room temperature. Figure reproduced from reference [22].

1.8.2 AFM Imaging of AMPs on Bacterial Model Membranes

As mentioned above, it is challenging to acquire high resolution AFM images in liquid on bacteria, and due to the complex composition of the bacterial cell wall, the interpretation of such images can be non-trivial. Hence model membranes can be useful alternative experimental systems, the composition of which can be tuned to mimic membranes of prokaryotic cells (such as bacterial cells) and eukaryotic cells (such as human cells).

The ideal mimetic membrane would have the same compositions of the material making up the real one. In addition, the location of these components within the membrane has to be the same as in the real one. In fact, scientists are still far from reaching this level of similarity in mimicking natural cell membranes. The challenge is mainly in characterising, synthesising and inserting the structurally complicated natural components of the membrane such as the membrane proteins and lipids, and controlling their precise position within the artificial membrane.

Such model membranes are often reconstituted from lipids alone. However, for example, it was mentioned before that LPS is the major component of the outer leaflet of the OM in gram-negative bacteria. To form a more realistic reconstituted bacterial membrane, membranes have also been formed by bacterial phospholipids (BPL) and LPS with a proportion (1:1) and (1:2) respectively [103]. The AFM images of such membranes, shown in figure 1.13, present the resulted membranes with phase separation, roughness and non-flat bilayer surfaces at two different temperatures 20 C^o and 40 C^o. Here, the height difference across the bilayer is due to the thickness difference between the two formed separated bilayers (LPS and BPL). The two temperatures 20 C^o and 40 C^o were chosen as LPS is either in gel or fluid phase respectively while BPL is in liquid crystalline phase in both temperatures [103]. At present, it is unclear how well these more complex model membranes represent the properties of bacterial membranes. In addition, natural bacterial membranes are asymmetric having LPS only on the outer leaflet, which further complicates the preparation of suitable biomimetics. On the other hand, lipid-only model membranes are readily prepared and have become very common model systems to at least represent lipid-related properties of bacterial (and eukaryotic) membranes.

Natural phospholipid extracts are now commercially available. For example, *E .coli* natural polar lipids extracts are available from Avanti® which are produced as a harvest from bacteria at specified growing phase. The datasheet specifies the lipids composition of this natural extract as PE 67%, PG 23.2%, CL 9.8% [104, 105]. This extract includes only the natural phospholipids making *E. coli* membranes and not the other contents like LPS or the membrane proteins.

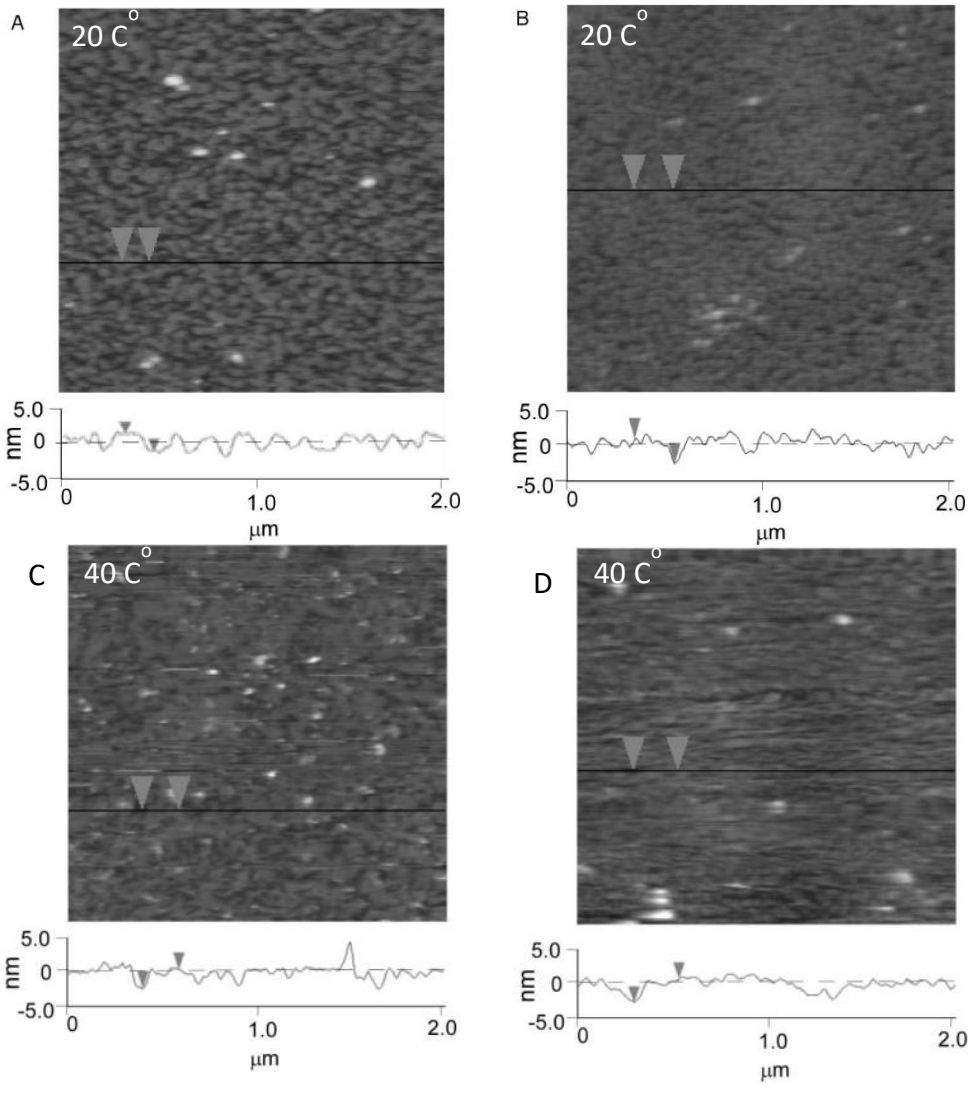

Figure 1.13: AFM images of Rd LPS/BPL supported membranes. (A) 1:1 Rd LPS/BPL* and (B) 2:1 Rd LPS/BPL formed on PEI-coated mica scanned in water at 20°C. (C) 1:1 Rd LPS/BPL and (D) 2:1 Rd LPS/BPL bilayers formed on PEI-coated mica, scanned in water at 40°C. The cross section profiles shows a non flat bilayer Image size, 2 μm2; z-scale, 20 nm.* BPL= Bacterial Phospholipids.

Gram-positive natural lipid extracts are also available commercially. For example, *B. subtilis* extract contains PE, PG, CL, lysyl-PG in addition to neutral lipids (mostly diacylglycerol) [106-109]. One resource specify the percentages of these as 30%, 35.7%, 12.1%, 22.1% respectively [108].

These percentages of phospholipids contents, however, can change with bacterial growth phase and conditions. For example, it was reported that CL levels rise, at the expense of PG when cells enter the stationary phase [110].

Nevertheless, collective studies confirm that PE and PG are the two major phospholipids making up the membranes for both Gram-positive (*B. subtilis*) and Gram-negative (*E.coli*) bacteria [106-110] .

PC and PE headgroups are chemically very similar with choline instead of ethanolamine group (methyl groups instead of hydrogen in the amine group) as shown in figure 1.3. They both are the major phospholipids making up the membranes of the eukaryotic cells including human cells [111]. Because both PE and PC are neutral phospholipids, they are not the first target of the cationic AMPs. This would in principle allow researchers to use both of them to represent the neutral content of the bacterial phospholipids.

However, the function of the membrane is not only related to the chemistry of the phospholipids headgroup, but also to the length and type of the hydrocarbon chain making up the hydrophobic tail of the phospholipid. There are many types of phospholipids tails in nature. They are identified by the number of the carbon atoms and the unsaturation (double bonds) within the chain. For example, a PC headgroup with saturated hydrocarbon tail of 12 carbon atoms is 1,2-dilauroyl-sn-glycero-3-phosphocholine (DLPC) while 14 carbon atoms is 1,2-dimyristoyl-sn-glycero-3-phosphocholine (DMPC), 16 carbon atoms is 1,2-dipalmitoyl-sn-glycero-3-phosphocholine (DPPC) and 18 carbon atoms is 1,2-distearoyl-sn-glycero-3-phosphocholine (DSPC). In addition, unsaturated hydrocarbon chains are common in nature. For example, 18 carbon atoms with one (cis) double bond is 1,2-dioleoyl-sn-glycero-3-phosphocholine (DOPC).

Many researchers have used different lipid composition to mimic bacterial membranes. For instance, Balhara et al, compared the interaction of a 13 amino acids AMP (GL13K) with liposomes and supported lipid bilayers (SLBs) of DOPC and DOPG lipids as models for eukaryotic and bacterial membranes, respectively [112].

Lopes et al, on the other hand, characterised and compared two bacterial model membranes; POPE/POPG with the mass ratio of 0.6:0.4 and POPE:POPG:CL with the mass ratio of 0.67:0.23:0.1 respectively. They found that this later system is closer to the *E. coli* natural extracts in thermotropic terms which explain the phase transitions when changing the temperature. Cardiolipin (CL) has been shown to have a strong influence on membrane organization which in turn affects protein–lipid interactions [113]. AFM images of both systems revealed that the bilayer thickness was reduced by 0.8 nm due to the addition of CL lipid.

Finally, Ryan et al and Jascindra et al, among others have used a vesicles mixture of DLPC:DLPG 3:1 mass ratio to study the interactions with different types of AMPs [114, 115].

In this thesis, we have followed the latter work in using DLPC:DLPG 3:1 mass ratio as a bacterial model membrane. The PG gives the overall anionic charge expected in the bacterial membranes. PC was chosen for consistency with all other experiments performed on the same AMPs by our collaborators at NPL. Supported lipid bilayers of this composition were prepared as described in chapter 2.

In chapter 3 of this thesis, two synthetic helical AMPs were studied as they attack the bacterial model membranes. The results demonstrated that a small change in the amino acid sequence induced a change in the mechanism of membrane degradation, leading to better understanding of the structure-function relationship for AMPs. In chapter 4, a de novo triskelion with three arms of antimicrobial β-sheet peptide motifs is characterised. The design was meant to co-assemble to form hollow antimicrobial capsules that can be used as antimicrobials as well as for intracellular gene delivery. Time lapse AFM imaging was used to monitor the attack of these capsules on the bacterial model membrane. In chapter 5, another de novo antimicrobial capsid system was studied. The design was inspired from the viral capsids and modified to have antimicrobial properties. AFM images revealed the poration kinetics and characterisation. Finally, chapter 6 is an overview of a possible commercialisation plan for of such materials (in line with departmental guidelines for PhD theses) with a business plan for antimicrobial wound dressing as a possible application.

Chapter 2

Materials and Methods

This chapter is divided into three main parts. The first part is describing the methods used for preparing the antimicrobial peptides studied in this research. The second part is describing the preparation of supported lipid bilayers (SLBs) as well as other sample preparation techniques for AFM. Finally, the third part describes AFM itself.

2.1 Antimicrobial Peptides Preparation

All antimicrobial peptides studied in this research were synthesised chemically and prepared in laboratories at the sponsoring company of the project (NPL). The synthesis and preparation of one batch of peptide could take up to 2-3 weeks. This involves many steps as mentioned below which usually performed by a team in NPL. I have been shadowing my colleagues in NPL during these preparation steps and performed them myself entirely for one peptide which was not one of those mentioned in this thesis.

2.1.1 Solid Phase Peptide Synthesis

All peptides studied in this project were synthesised via solid phase peptide synthesis (SPPS). This technique was introduced by Merrifield in the early 1960s. In addition to synthesising peptides [116], it is also used to synthesise other organic molecules and oligonucleotides. This method uses a solid support (polymer-based resin), which is usually polystyrene, as a platform to facilitate and accelerate reactions between reactants. The resin is modified by attaching a cleavable linker (a chemical group) which provides an active centre to initiate the reactions of attaching the first amino acid to the resin. The amino acids used in the synthesis must have a protected N-α amino groups. This protection is temporary to allow only one possible reaction on the peptide chain. The protecting groups can then be selectively removed during the synthesis to allow the coupling of a next amino acid and thus the assembly of the peptide sequence happens in a step-wise fashion as illustrated in figure 2.1.

There are many advantages of SPPS over in-solution peptide synthesis [117]. Firstly, generally no post-coupling purification step is needed. In addition, it enables the use of excess reagents driving each coupling reaction to the completion. Moreover, the synthesis can be automated and optimised to shorten synthesis cycles.

The limitations of SPPS, however, are the difficulty of monitoring each synthesis step as it requires additional set-ups (e.g., UV monitoring or Kaiser test).

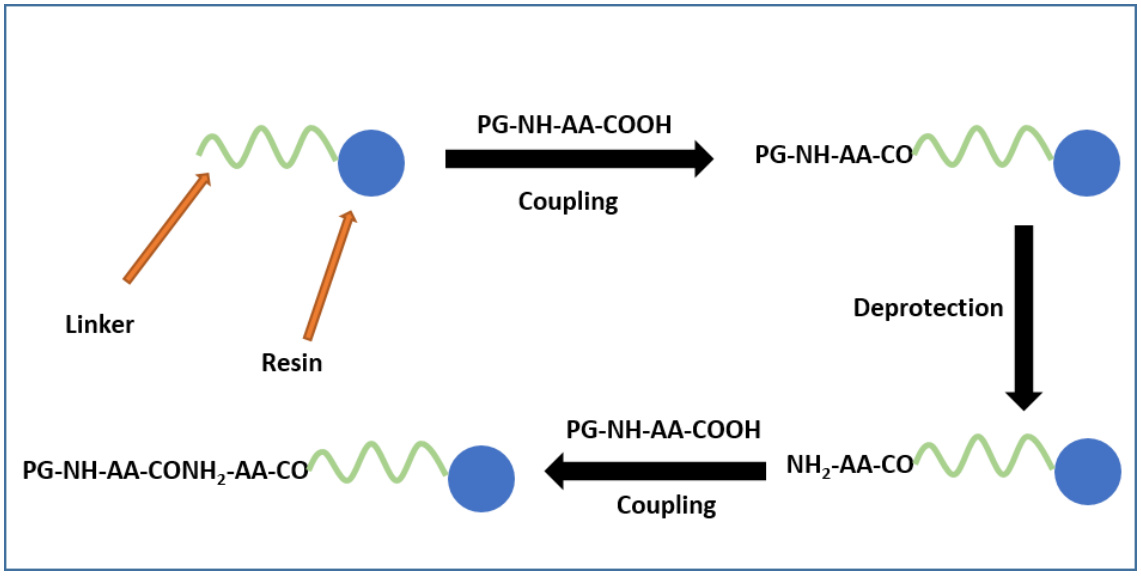

Figure 2.1: Solid phase peptide synthesis cycle. The synthesis of a peptide using N-protected (PG) amino acids.

In addition, it typically requires an excess amount of (potentially expensive) reagents and solvents used. However, these disadvantages can be offset by the high quality of the final product.

2.1.1.1 The Solid Support: Polystyrene Resin

Since SPPS was introduced by Merrifield using polystyrene-based polymer as a support, a great number of other materials have been introduced. Nevertheless, polystyrene resin is still the most commonly used support in solid phase chemistry [118] and is obtained by a co-polymerization reaction of styrene and divinylbenzene (figure 2.2).

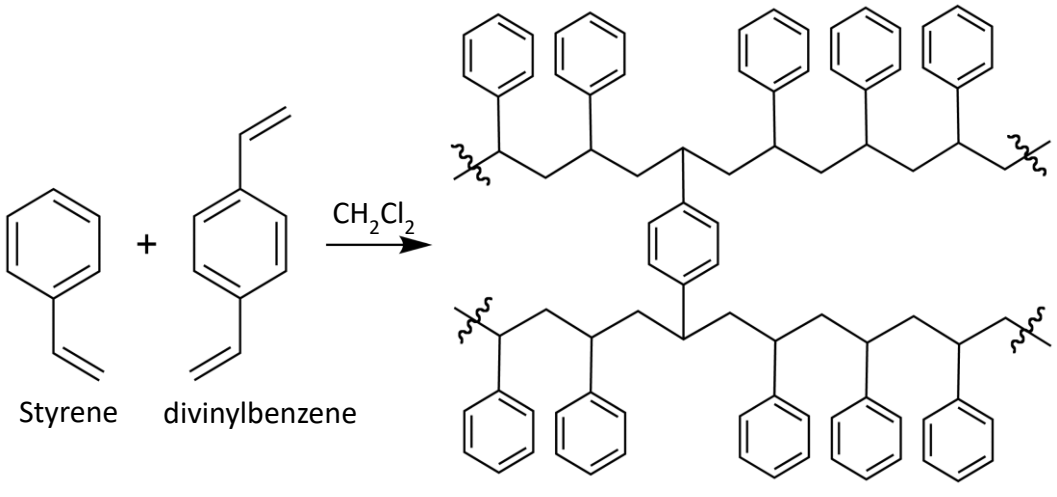

Figure 2.2: Synthesis of polystyrene resin with divinylbenzene cross-linking.

Divinylbenzene is used to a small concentration (1-2 %) in the reaction to cross-link polystyrene chains, figure 2.2. The degree of cross liking is directly related to the ability of resin to swallow when solvating, which has an effect on the reaction kinetics.

Polystyrene resins are insoluble in organic solvents, but when solvated in aprotic solvents such as toluene, DMF, and DCM they become swollen and mesh-like. The more the resin swallows, the larger the diffusion rate of the reactants toward the resin matrix [119]. Since the reaction kinetic is a diffusion controlled, higher diffusion will make the reaction time shorter.

2.1.1.2 Linkers

Achieving a covalent bond of organic molecules directly into the polystyrene support is difficult. A more efficient approach is to modify the polystyrene support with different linkers. A large number of linkers have been developed and are commercially available and each has an advantage for a particular synthesis. Figure 2.3 shows the chemical structure of MBHA linker used in synthesising all peptides studied in this project [9]. When cleaving the peptide at the end of the synthesis, this linker gives an amide group at the carboxylic end.

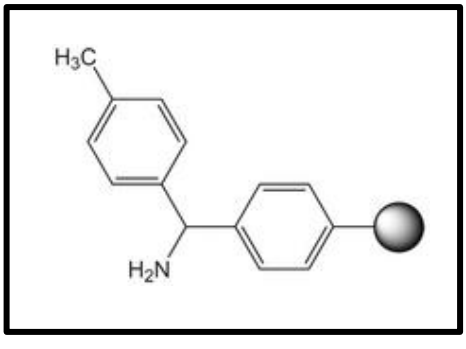

Figure 2.3: Chemical structure of MBHA linker attached to resins (grey balls) used for SPPS [9].

2.1.1.3 Boc and Fmoc Protected Amino Acids for Solid Phase Peptide Synthesis

Peptide synthesis happens through steps in which the amino acids forming the peptide sequence are added one by one. For this stepwise SPPS to happen, two types of protecting groups are necessary to avoid undesired reactions and side products. The first one is a protecting group on the α-amino group of each new amino acid added to the reaction which is also called orthogonal protecting group. This protecting group will prevent the same amino acid to form a chain with itself; instead, it only allows the carboxylic acid side to form a peptide bond with the α amino group at the end of the peptide chain. This protecting group is then removed after each coupling (linking an amino acid to the chain) to allow chain

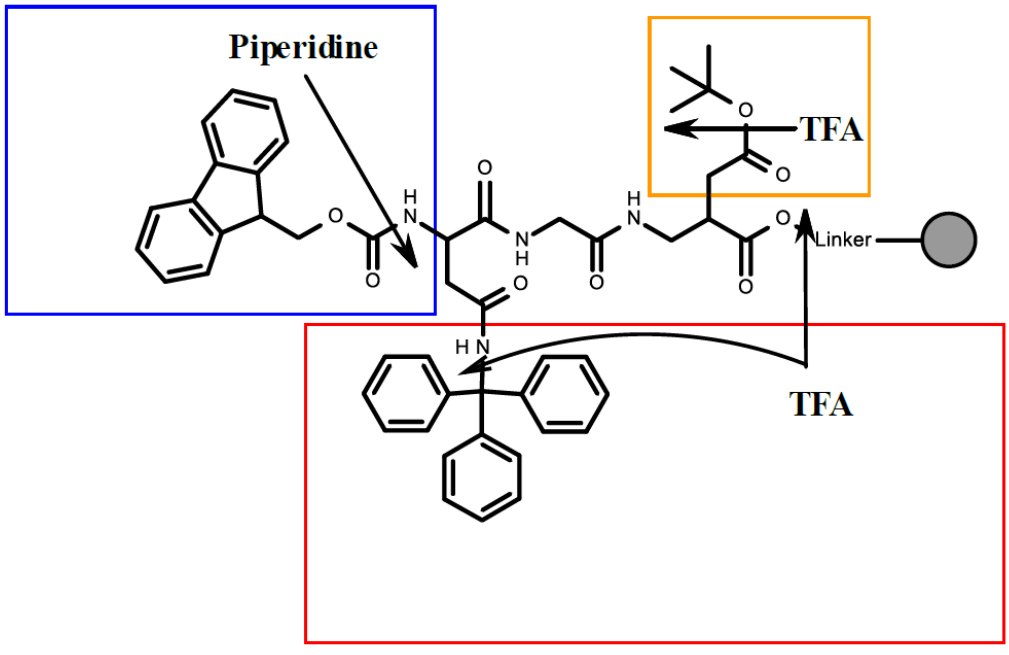

Figure 2.4: Orthogonal protection using Fmoc as Nα-protection group and acid labile side-chain protecting groups. Fmoc groups are removed only using basic conditions (blue box). Low TFA concentrations are sufficient to remove highly acid labile trityl groups (Red box), whereas high TFA concentrations remove all acid-labile groups including Boc and Trityl groups (red and orange rectangle). Figure reproduced from [5].

elongation. The second protecting group is a side chain protecting group which is necessary to prevent reactions that could happen on the side chains of the amino acids.

These protecting groups are usually removed at the end of the synthesis during the peptide cleavage (detaching from the resin). Hence, the removal of these two protecting groups should happen via two different mechanisms.

Amino acids that already have their groups protected are commercially available. There are two main types of protected amino acids according to the N-α protecting groups. Boc (tert-butyloxycarbonyl) and Fmoc (9H-fluoren-9-ylmethoxycarbonyl) protected amino acids, figure 2.4. The removal of the Fmoc protecting group is achieved by adding a very mild base, usually piperidine, leaving an exposed neutral amine group. Therefore, no neutralisation of the peptide-resin is require after each deprotection, figure 2.4 (blue box). The Boc protecting group on the other hand is removed by adding acid which is usually TFA, figure 2.4 (yellow box).

The choice of Boc or Fmoc as an orthogonal protecting group depends on the nature of the resin linker and the synthesised peptides. For example acid sensitive resins can be used

only with Fmoc orthogonal protecting group [120]. All the peptides in this study were synthesised using Fmoc as orthogonal protecting group and Boc as a side chains protecting group.

2.1.1.4 Coupling Principle

In order to form a peptide bond, the carboxyl group of the amino acids needs to be activated to couple with the amino group of another amino acid. This activation is necessary to speed up the reaction. Figure 2.5 shows the coupling reaction using a general activating group.

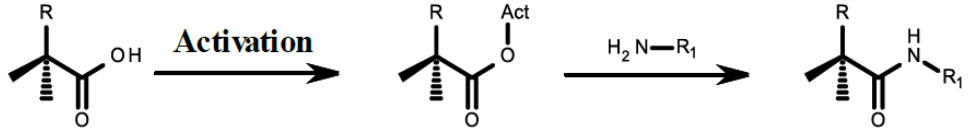

Figure 2.5: Formation of amide bonds via activating the carboxylic acid group of one amino acid.

There are many different activation agents available. There are activating groups such as phosphonium salts and uronium salts. The two activating groups used in this study are HBTU, TBTU. Both are uranium salts with a chemical structure illustrated in figure 2.6. For the coupling reaction to be activated, it usually needs specific conditions suitable for the type of activating group used. For these activating groups, a basic medium is necessary and usually achieved by using DIPEA (Diisopropylethylamine).

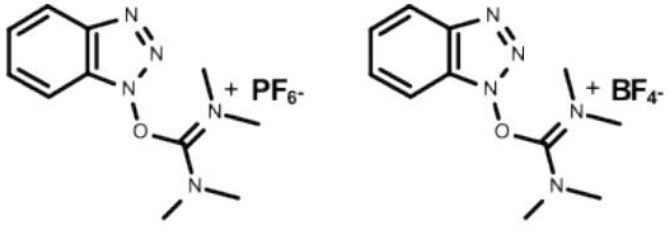

Figure 2.6: Chemical structures of the two activating groups HBTU and TBTU [7] .

2.1.1.5 Peptide Synthesis Protocol

All peptides studied in this project were synthesised by a Liberty-1 microwave peptide synthesizer (CEM Corp) as peptide amides using solid phase Fmoc/tBu protected amino acid. HBTU/DIPEA are used as coupling reagents and Rink amide 4-

methylbenzhydrylamine (MBHA) resin (Novabiochem, UK) was used throughout. For the synthesis of capzip monomers, Fmoc-Lys(Mtt)-OH was used to enable orthogonal conjugation via a tri-functional dendritic hub – βA-KK-am. While allyl-based orthogonal protocols were used for the synthesis of the C 3 (+) -triskelion on resin. Fmoc-Lys(Alloc)-OH was used to generate the C 3 -dendrimer hub. The C 1 (-) strand was acetylated using a solution containing acetic anhydride (5%, v/v) and pyridine (5%, v/v) in DMF.

2.1.2 Peptide Purifications

Once the peptide is synthesised, the resin is thoroughly washed with DMF and DCM and then cleaved and deprotected using an acidic mixture containing 95% TFA, 2.5% TIS, 2.5% water. The resin is then separated from the peptide solution by filtration followed by peptide precipitation using cold diethyl ether. The pellet (containing the peptides) is re-suspended in di-water to be purified by RP-HPLC.

2.1.2.1 RP-HPLC

All peptides were purified by semi-preparative gradient reversed-phase high performance liquid chromatography (RP-HPLC). RP-HPLC was performed on a JASCO HPLC system using Vydac C18 semi-preparative (5 µm 10 mm i.d x 250 mm) column.

The semi-preparative HPLC was run using a 10-60 % buffer B gradient over 50 min at 4.5 mL/min with detection at 280 nm, 230 nm and 220 nm. The mobile phases used are: buffer A – 5% aqueous CH3CN, 0.1% TFA and 95% Water, buffer B – 95% aqueous CH3CN, 0.1% TFA and 5% water.

2.1.3 Peptide Characterisation

The identity of the peptide was confirmed by analytical reversed-phase high performance liquid chromatography (RP-HPLC) and matrix-assisted laser desorption/ionization time-of-flight (MALDI-ToF) mass spectrometer. Similar to semi-preparative, analytical RP-HPLC was performed on a JASCO HPLC system but using Vydac C18 analytical (5 µm, 4.6 mm i.d x 250 mm) column. It was again run using same buffers but with a gradient of 10-60 % buffer B over 50 min at 1 mL/min. Analytical RP-HPLC was employed to determine the peptide purity. As the eluted peptides from the chromatography column are represented by peaks on the micrographs, the sharpness of these peaks indicates the purity. The integrated area of these peak is a measure of the purity. All the peptides produced for this study had a purity of at least 98%.

The final peptides constructs were also identified by MALDI-ToF mass spectrometry with α-cyano-4-hydroxycinnamic acid as the matrix to help ionisation of the sample. Mass spectra

show peaks of mass/charge ratio of the positive ions resulted from sample ionisation. As MALDI-MS is considered a soft ionisation technique, the full peptide structure is expected to be ionised without fragmentation. Hence the calculated mass/charge ratio of the peptide should appear experimentally in the spectrum as a sharp peak. The purity of the peptide could also be identified from MALDI-MS spectra. The peaks that are not related to the peptide must be attributed to the impurities. Ideally, the pure peptide sample should show only peaks that are attributed to the full structure of the synthesised peptide.

2.1.4 Peptides Drying and Storage

Once the peptides were purified, they were freeze dried and stored in their powder form at -80 C^{o} freezer.

2.1.5 Peptides Sample Preparation

In order to prepare the liquid sample used for experiments, the peptide powder was dissolved in DI water and the molar concentration was determined using the UV:VIS spectroscopy, employing the Beer-Lambert Law explained in the next section [121]. Once the concentration of the stock solution was determined, peptide solutions of lower concentrations were prepared by simple dilution with DI water. The entire amount of solution then was divided into small volumes (200 µL each) and kept separately in small Eppendorfs tubes in the freezer (– 4C). In this way, frosting-defrosting of the peptides was avoided to minimise the risk of peptide deformations.

2.1.5.1 Determining the Molar Concentration

The Beer-Lambert Law given in the equation 2.1 relates the total absorbance of the material to its concentration in the solution. Two constants are involved in this equation. First, the extinction coefficient (ϵ) which is directly related to the chemical bonds and chemical structure of the absorbents. Second, and the path length (l) which is the cell width through which the light passes.

$$A = \epsilon l c \qquad 2.1$$

A: The Absorbance

l: The length of the cell path (cm)

c: The concentration of the absorbent (mole L^{-1})

ϵ: The extinction coefficient (L $mole^{-1}$ cm^{-1})

The cell used in the studies has a width of 0.1 cm, a value which can be substituted in the equation. The extinction coefficients of the peptides were determined by summing up all the extinction coefficients of every amino acid and chemical bond that absorbs at the selected wavelength [121]. By measuring the absorbance of the peptide solution at the selected wavelength, and by substituting the extinction coefficients and the length of the cell used in the equation 2.1, the concentrations of the peptide solutions were determined.

2.1.5.2 Peptides Extinction Coefficient Calculations

Table 2.1 shows the amino acid sequences of each peptide studied in this project with their calculated extinction coefficients at the selected wavelengths. Appendix 1 includes a list of the amino acids with their abbreviation and chemical structure.

Peptide	Amino Acid Sequence	Wavelength λ	Calculated ϵ
Amhelin	KQKLAKLKAKLQKLKQKLAKL-am	214	19621
Tilamin	KARLAKLRARLYRLKARLARL-am	280	1280
Capzip monomer	(RRWTWE)-βA-K(RRWTWE)-K(RRWTWE)-am	280	34140
C3 (+)	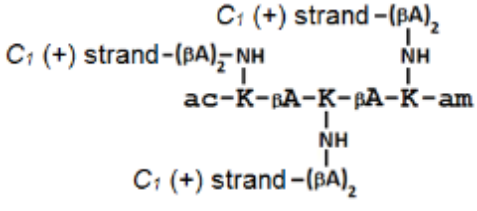	214	71241
C1 (-)	ac-CβAEISALEQEIASLEQEISALEQ	214	22848

Table 2.1: The studied peptides with their amino acid sequences, the calculated extinction coefficient at the specific absorbance wavelength

2.1.5.3 Peptides Sample Preparation for AFM

Starting from the peptides stock solutions of determined concertation, amhelin and tilamin peptides were considered ready for AFM experiment. The required concentration of the peptide for AFM experiments was achieved with simple dilution of the peptide stock in DIi-water or in the relevant buffers.

However, capzips (explained in chapter 4) and capsids (explained in chapter 5) require more preparations for the peptide monomers to co-assemble into antimicrobial spherical shells.

For capzip, the monomers stock solution was used to prepare a solution of 100 µM in MOPS buffer pH 7. The sample then was left overnight at room temperature prior AFM experiments.

Capsids on the other hand, was prepared by mixing two peptides C1 (-) and C3 (+) with the molar ratio of 3:1 respectively. The overall monomers concentration in the sample was 100 µM (75 micromoles C1 (-) and 25 micromoles C3 (+)). To achieve the required concentration of the monomers, the peptide stock solutions were diluted in MOPS buffer pH 7. To induce the assembly, the sample requires the addition of the reducing agent TCEP to a concentration of 0.147 M in the sample. Prior to mixing TCEP with the peptides monomers, TCEP was neutralised to pH 7.4 using 1 M NaOH. After mixing all the three components, C1 (-), C3 (+) and neutralised TCEP, the sample was tleft to self-assemble over night at room temperature.

2.2 AFM Sample Preparations

2.2.1 Substrates for AFM Imaging

Choosing the suitable substrate is essential to immobilise the biological sample during scanning. Muscovite mica has been demonstrated as a suitable substrate for biological samples. It consists of layers of silicate minerals sheets. The top sheets are easily cleavable by an adhesive tape leaving a clean and atomically flat layer [122]. For most experiments in this study, sample supports were made using ⌀ 15 mm steel SPM specimen discs (Agar Scientific), topped by a layer of self-adhesive, fluorinated ethylene propylene (FEP) coated Bytac laminate with a thickness of 0.254 mm (Saint-Gobain Performance Plastics). On the Bytac laminate, a ⌀ 9.9 mm muscovite mica disc (Agar Scientific) was glued using two component Araldite rapid epoxy adhesive (Huntsman Advanced Materials) with a 5 min working time. The sample supports were cured overnight before use.

The hydrophobic (FEP) layer clued in between the metal disc and the mica is to make a hydrophobic edge around the mica disc, to prevent the liquid from leaking off the mica.

Before using the substrate, mica discs were cleaved using Scotch Magic tape (3M). In this process, several layers of the mica crystal are removed from the surface, leaving a flat and clean substrate suitable for lipid bilayer deposition and AFM experiments.

To facilitate the immobilisation of the molecules of interest on mica, it is often beneficial to add covalent cross-linking agents or certain cations such as calcium or magnesium. These link the constituents of the sample to each other and/or to the mica.

In this study, and for immobilising the negatively charged lipid bilayers on mica, mica discs in all samples were treated with buffer including ~10 mM of both $CaCl_2$ and $MgCl_2$.

2.2.2 Buffer Solutions

Two buffer solutions were used to prepare all the samples in this study. It was either 20 mM HEPES with 150 mM NaCl or 10 mM MOPS with 150 mM NaCl. The required amounts of HEPES, MOPS and NaCl powders were weighed and dissolved in DI water to get the concentration needed. Then the pH was adjusted to 7.4 by adding 1 M NaOH.

2.2.3 Phospholipids

As discussed in chapter 1, supported lipids model membranes were employed in this work to study the peptides antimicrobial mechanisms.

This was achieved by using two types of lipids, namely DLPC (1,2-dilauroyl-sn-glycero-3-phosphocholine) and DLPG (1,2-dilauroyl-sn-gly-cero-3-phospho-(1-rac-glycerol)) with a mass ratio of 3:1 (W:W). The chemical structures of these two lipids are shown in figure 2.7. This composition was chosen as a good mimic of the bacterial membrane [123, 124] and it was the same lipid composition used in other complementary experiments that were carried out at NPL.

DLPC is considered as neutral lipid and DLPG is negatively charged under the experimental conditions at pH 7. In addition, both lipids have transition temperatures below zero Celsius, which means they stay in the fluid phase and not in the gel phase at room temperature.

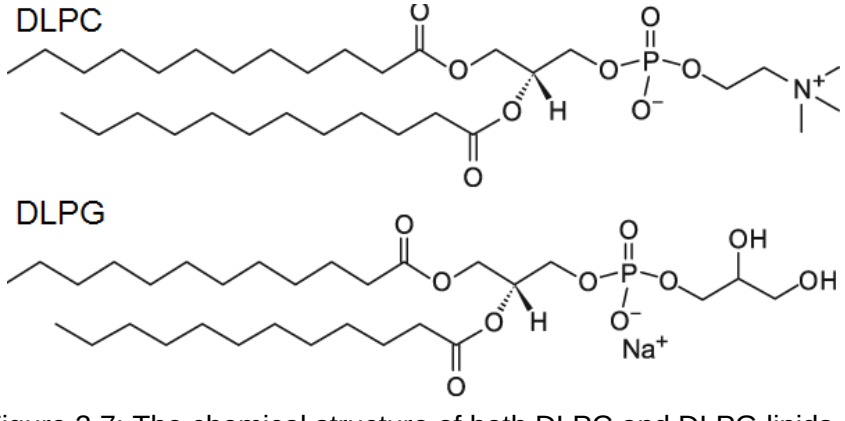

Figure 2.7: The chemical structure of both DLPC and DLPG lipids.

2.2.4 Formation of Bacterial Model Membranes

The bacterial model membranes were prepared fresh before every experiment following the same protocol which includes three main steps explained below.

2.2.4.1 Formation of Small Unilamellar Vesicles

The weighed amounts of the lipid powder (usually 3 mg DLPC and 1mg DLPG) are mixed and dissolved in 1 mL organic solvent to obtain a homogeneous mixture. This solvent was chosen to be Chloroform:Methanol 2:1 (V:V). The lipid powder and the solvent are mixed together in a glass vial until a clear solution is achieved. The organic solvent is then evaporated by a gentle steady nitrogen stream to form a dry lipid film deposited at the bottom of the glass vial. This film is then hydrated by 1 mL deionised water to achieve a lipid solution with a concentration of typically 4 mg/mL. The lipid suspension is vortexed for 2-4 minutes at room temperature to mix the lipids. At this stage, the lipids form large multilamellar vesicles (LMVs) in solution. These must be dispersed and reduced to single unilamellar vesicles (SUVs) via sonication and extrusion. The cloudy suspension of LMVs is sonicated at room temperature, well above the transition temperature of the lipids for sixty minutes in a bath sonicator. The use of the 80 kHz sonication frequency allows the large vesicles to be ruptured and broken down into SUVs. To ensure a uniform size distribution of vesicles in suspension, extrusion is performed [125]. Extrusion is the process by which the lipid suspension is forced through a polycarbonate membrane with pre-defined pore sizes. In this study, the lipid suspension is chosen to pass through a 50 nm pore membrane to form vesicles with 50 nm diameter. The process was performed a minimum of twenty times to ensure a uniform size distribution using an Avanti mini-extruder.

2.2.4.2 Absorption of Lipids Vesicle to form the SLB

The preparation of supported lipid bilayers is performed via the vesicle fusion method, described fully in reference [126]. The vesicle fusion method cannot be used to form asymmetric bilayers or closely regulate the packing density of the lipids in the bilayer as can be achieved via the Langmuir-Blodgett technique, but the vesicle fusion technique allows bilayers to be assembled relatively easily and quickly.

In the vesicle fusion method, SUVs in suspension are allowed to adsorb onto the sample substrate over a period of 30-60 minutes. If the transition temperature of the lipids is above room temperature, the process can be completed at room temperature [127].

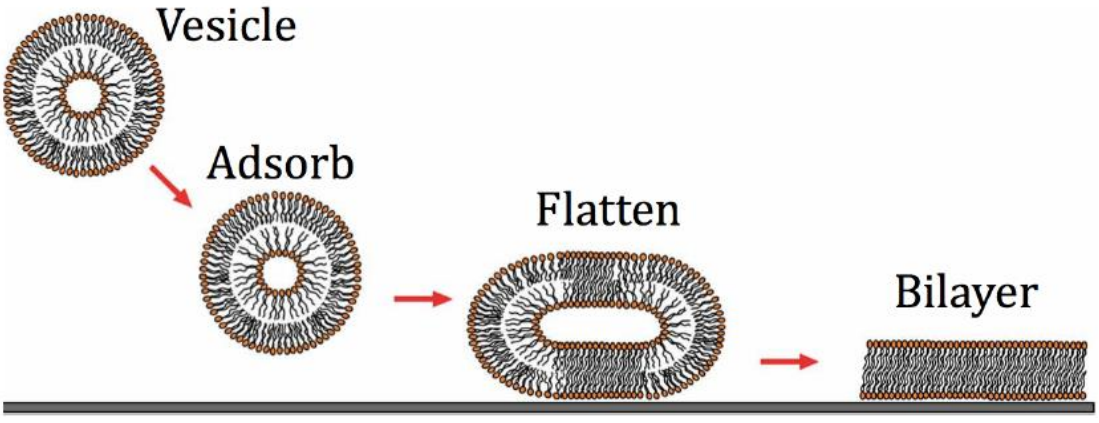

Figure 2.8: A schematic showing the deformation of a vesicle as it fuses onto the mica substrate forming the SLB. Illustration prepared by Dr Carl Leung

As the lipids reach the surface the spherical vesicles deform onto the surface as they adsorb, becoming ellipsoidal in form, before rupturing to form a bilayer fused to the mica surface [128]. A schematic of the vesicle fusion process is shown in figure 2.8.

The substrate used in this research is mainly muscovite mica, which has a negatively charged surface under the here applicable buffer conditions [129]. In addition, the vesicles prepared to form the bacterial model membranes are negatively charged because of the presence of the negatively charged lipid DLPG.

Therefore, it is essential to add bridging positive cations to attract the negatively charged vesicles and immobilise the formed bilayer on mica [130]. In this study, we employed two cations, calcium and magnesium each with a concentration of 10 mM in the buffer. This cations-contained buffer is used to hydrate the mica substrate before letting the (DLPC:DLPG) lipid vesicles to absorb onto the mica surface.

This technique has been successfully used to form a continuous bilayers with both full and partial coverage on the mica. There are a number of parameters that can influence this process, including temperature, time of incubation and the amount of added lipid vesicles on the mica [131].

Model membranes were typically prepared at room temperature by adding 2 µL lipids vesicles solution (4 mg/ml) onto clean and freshly cleaved mica, which was pre-hydrated by 50 µL buffer containing 10 mM cations. The samples then were incubated for about 30 minutes in room temperature, well above the transition temperature of the lipids. The mica was then washed about 10 times with the same buffer except for the calcium and

magnesium cations. This washing stage removes any lipids remaining in the fluid that were not adsorbed to the substrate, to prevent later aggregation on the model membrane.

2.3 AFM Imaging

As explained in chapter 1, AFM can be used to image the peptides in action, or at least their effects, as they attack bacterial membranes. Here I am explaining the principle of AFM technique, the main components of atomic force microscope and the common modes of operation. In addition, I explain the methods for optimising the imaging on SLB.

In this project, I employed three atomic force microscopes, namely Multimode 4, Multimode 8 and FastScan Bio systems (Bruker, CA, USA). As explained below, different AFM operation modes and cantilevers were employed.

2.3.1 AFM Principles of Operation

AFM generates images by feeling the sample surface. This happens via tracing a sharp tip attached to a flexible lever over the surface of interest, as illustrated in figure 2.9. The surface could be a hard sample or a soft biological specimen, which in this case requires more care in applying lower forces to avoid sample deformation. Three dimensional images are recorded by scanning the sample surface by the AFM tip in a two dimensional (*xy*) plane with the ability to move in the third dimension (*z* dimension) when the tip senses features on the surface. As the tip is raster scanned over the surface, the topography of the sample surface is reconstructed from these traces. The movement of the sample or the tip in the *z*-direction is in response to the tip-sample interactions. When the tip encounters a feature on the scanned surface, a tip-sample interaction will arise. This then will change the force applied between the tip and sample. Usually, AFM is operated by keeping these tip-sample interactions or force gradient constant, via adjustment of the *z* position of the tip.

AFM can be operated in several modes. Each mode has different way to monitor and control the tip-sample interaction. In addition, AFM experiments can be performed in a vacuum, air or fluid. AFM operations in fluid are arguably the most relevant for imaging biomolecules.

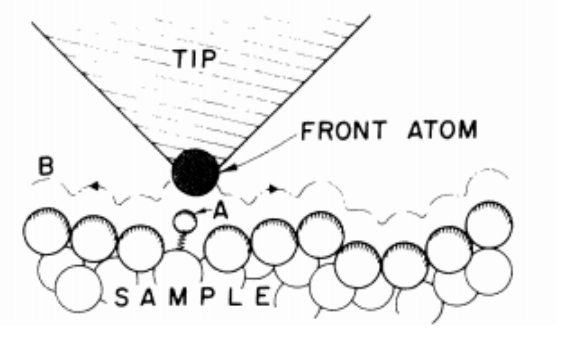

Figure 2.9: Description of the principle operation of an AFM. The tip follows contour B to maintaining a constant force between tip and sample. Figure reproduced from reference [11].

The change of tip-sample interactions induces bending of the cantilever or changes in a cantilever oscillation. In the majority of AFM setups, the cantilever bending or changing in the oscillation is monitored optically via the optical lever method pioneered by Alexander in 1989 [132]. This is achieved by focusing a laser on the back side of the cantilever and reflected on a position-sensitive detector (PSD), which is usually a quadrant photodiode. The quadrant photodiode measures the bending of the cantilever through the displacement of the laser signal.

The optical lever method reads the deflection of the cantilever on the quadrant photodiode by converting the incident light on each quadrant into a voltage as shown in figure 2.11. The vertical displacement or deflection of the cantilever can therefore be measured by the difference between the upper and lower quadrants of the photodiode. In the same manner, the voltage differences between the left and right quadrants can be used to determine the torsional motion of the cantilever, such as can be induced by frictional forces. The optical lever method amplifies the movement of the cantilever purely by path length, as the measured displacement on the photodiode (D) is proportional to the cantilever movement (z) multiplied by the path length from the cantilever to the photodiode (S) over the cantilever length (l) as shown in equation 2.2 [133].

$$D = \frac{3}{2}\frac{S}{l}z \qquad 2.2$$

The applied force in an experiment (F) can be calculated by Hooke's law shown in equation 2.3 from the deflection of the cantilever which gives the cantilever displacement (x) and the stiffness of the cantilever (k).

$$F = -kx \qquad 2.3$$

The applied force is therefore strongly dependent on the stiffness of the cantilever, as will also be discussed in section 2.3.5, and to the minimum detectable cantilever bendin. Alternatively or complementarily, force gradients and dissipation can be derived from changes in the oscillation of the cantilever when it is modulated vertically during the (lateral) scanning over the sample surface as described in section 2.3.4.2.

2.3.2 Tip-Sample Interaction Forces

Since the surface topography is determined from contours of constant tip-sample interaction (at least on average), it is worthwhile to understand the forces acting on the tip. Relevant forces in liquid and vacuum operations are long range attractive van der Waals, electrostatics and short-range repulsive interactions, figure 2.10. However, in air operation, capillary forces and the resultant adhesive forces should also be considered. The long range van der Waals forces and electrostatic forces can act over tens of nanometres and are caused by dipole interactions between atoms, and by Coulomb interaction between surface charges, respectively. At the Ångström range, the strong repulsive force originating from the overlap of atomic orbitals begins to dominate. At this point the tip is considered to be in contact with the sample. In air, the water meniscus formed between the tip and the sample causes an attractive capillary force between the tip and the sample. In aqueous salt solutions, van der Waals forces and electrostatic forces are usually screened for tip-sample distances larger than a few A, and there are no capillary forces.

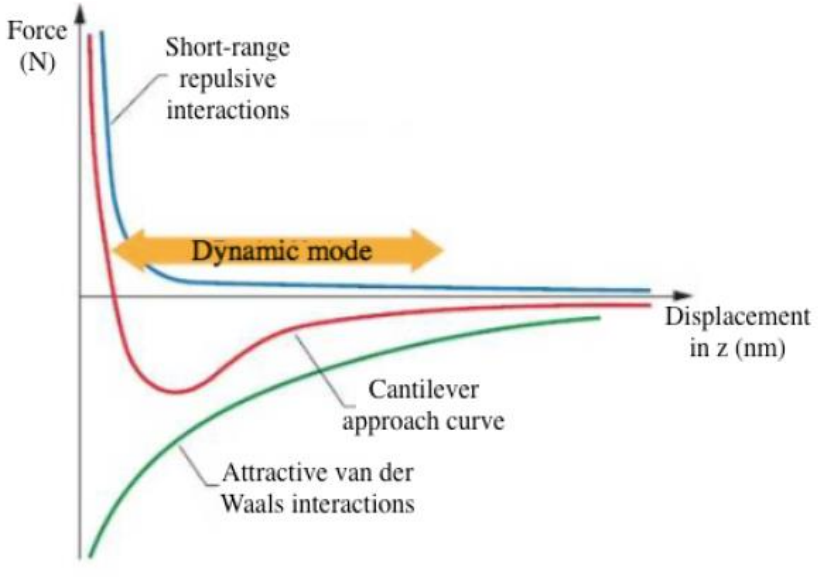

Figure 2.10: A representation of forces that can act on the AFM tip at various tip-sample separations with ignoring electrostatic interactions. At high separations the attractive van der Waals dominate, with the repulsive short-range repulsive forces dominating at lower separations. Figure was reproduced from [3].

2.3.3 AFM Imaging in Liquid

One of the main advantages of using the AFM for imaging biomolecules is the ability to work in fluid and thereby visualise and probe biomolecules in conditions similar to their natural

state. Additional advantages of AFM operation in liquid are the avoidance of the tip-sample capillary forces experienced in air, as explained above. These forces increase the contact area between the tip and the sample and tend to reduce the spatial resolution [134]. Another advantage of the operation in liquid is the use of buffer solutions. These buffer solutions permit tuning the long range electrostatic forces between the tip and the sample. This control of electrostatic forces can increase the spatial resolution [135].

The distance over which the long range electrostatic force decays is defined as the Debye screening length (K^{-1}) which is given by equation 2.4. This equation shows that (K^{-1}) is dependent on the permittivity of vacuum and the dielectric constant of the medium (ϵ_0 and ϵ_r, respectively). It also depends on the absolute temperature (T), the ionic strength of the solution (I), the electron charge (e) and Boltzmann's constant (k_b). Under typical conditions for AFM imaging of biomolecules, K^{-1} is a few Å.

$$K^{-1} = \sqrt{\frac{\epsilon_0 \epsilon_r k_b T}{2e^2 I}} \qquad 2.4$$

Figure 2.11 shows the standard setup of an AFM in liquid. The principle is the same as in air but without immersing the sample and cantilever in fluid. For imaging in fluid, a fluid cell (not shown) is used to hold the cantilever and contain the liquid.

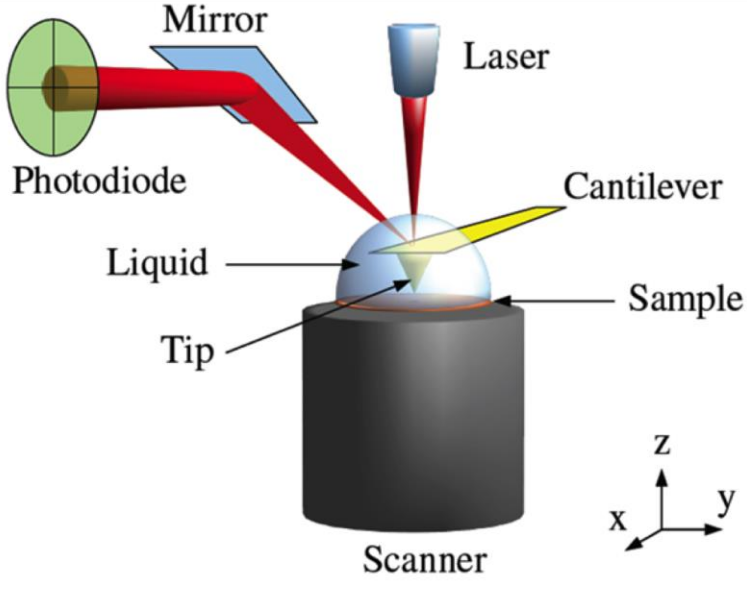

Figure 2.11: A schematic showing the operation of the AFM in fluid. Image courtesy of Prof Bart Hoogenboom.

There are some disadvantages to AFM imaging in fluid related to viscous damping. This is more pronounced for imaging in dynamic modes since the damping force exerted by the viscous liquid causes the resonant frequency f_0 and the quality factor, Q, of the cantilever to decrease. This issue will be discussed more in section 2.3.4.2. All AFM experiments in this project were carried out in fluid under buffer conditions with near-physiological pH and salt concentrations.

2.3.4 AFM Imaging Modes

As mentioned previously, AFM can function in a number of imaging modes, the most common of which are contact and tapping mode. Contact mode, elaborated in next section, is the simplest and fastest mode. However, its use for imaging biomolecules is limited because of the relatively high lateral forces exerted on the specimen. Tapping mode, elaborated in section 2.3.4.2, operates by oscillating the tip vertically above the sample. This makes the tip continuously coming into and out of contact with the sample in a `tapping' motion. This vertical modulation reduces the lateral forces that the tip exerts on the sample making it widely used for imaging biomolecules in liquid with lower risk of distortion or destruction of the specimens under study. Peak force tapping, elaborated in section 2.2.4.3, is a relatively recent mode for high resolution imaging of biomolecules and has been used extensively throughout this project along with tapping mode.

Other popular modes which have not been used in this project and not explained here are frequency-modulation AFM and multi-frequency AFM.

2.3.4.1 Contact Mode AFM in Liquid

In contact mode AFM, the tip is kept constantly in contact with the surface while moving across the sample. The cantilever deflection is directly proportional to the interactions arise between the tip and the molecules on the surface. In most commercially available AFMs, this deflection is simultaneously probed by the optical detector and translated by the feedback loop to the scanner. Typically, the feedback loop directs the scanner to adjust the *z* position (vertical position) of the cantilever or the sample to maintain a predefined constant force or cantilever deflection known as the setpoint. This assure a constant interaction force between the tip and the sample [133].

Contact mode AFM is the simplest in term of operation but it has its drawbacks of applying the large lateral force on the sample leading possibly to damage of soft biological specimen. In addition, the deflection of the cantilever drifts over time, even without contact with the sample, which results in a change in the applied imaging force as the setpoint is maintained. This can result in much larger forces than intended being applied to the sample. For this

reason, relatively soft cantilevers with less than 0.1 N/m spring constant are recommended to be used in this mode for scanning soft surfaces.

Dynamic imaging modes were subsequently developed and introduced to reduce the lateral force applied to a biomolecule [134],[136].

2.3.4.2 Tapping Mode AFM in Liquid

Tapping mode AFM, also known as amplitude modulation (AM-AFM) or intermittent contact mode, is one of the many dynamic modes evolved to minimise the drag force applied on the sample while scanning. This is achieved by oscillating the cantilever vertically while scanning the surface with maintaining constant frequency or amplitude. Hence, the time spent by the tip applying force on the surface while scanning is lessened. This technique is particularly useful for imaging biological molecules loosely bound to a substrate where the use of contact mode AFM would result in sample damage or sample movement. The movement of the sample/molecules during imaging could also irreversibly blunt the tip which results in reducing the resolution.

Hence, in this operational mode we can use stiffer cantilevers with up to 0.6-1 N/m spring constant without a significant damage of the sample. The cantilever is oscillated while scanning at its resonance frequency to get the maximum oscillation amplitude. The resonance frequency of the cantilever, f_0 , is (approximately) the frequency at which the driven cantilever amplitude response is largest. This can be calculated using the equation (2.5) knowing the cantilever's effective mass m and the stiffness k.

$$f_0 = \frac{1}{2\pi}\sqrt{\frac{k}{m}} \qquad (2.5)$$

This is usually achieved by driving the tip (the cantilever) to oscillate sinusoidally above the sample at a frequency f close to the natural resonance of the cantilever, f_0 , while the cantilever raster scans the surface.

The cantilever is usually driven mechanically by a piezoactuator in the fluid cell. The amplitude of oscillation is monitored as the root mean square (RMS) value of the deflection readout on the detector. When the tip approaches the sample surface while oscillating at frequency f, the attractive or repulsive tip-sample forces will change the resonance frequency of the tip that is driven and the energy is dissipated during the oscillation.

Figure 2.12 shows an example of a cantilever resonance curve when it is away from the sample and when interacting with the sample. The cantilever resonance decreased by Δf, when the repulsive tip-sample interaction increases.

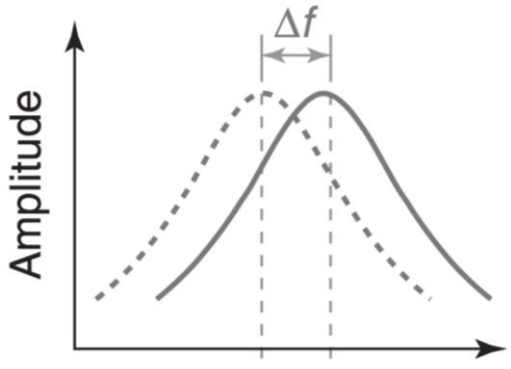

Figure 2.12: Amplitude versus frequency curves for a cantilever driven near resonance away from the sample (dotted line) and interacting with the sample (solid line) [3].

As shown in figure 2.10, changing the tip-sample distance affects the type and strength of forces raised between the tip and the sample. Hence, the topography changes of the surface when scanning will alter the strength of the interactions between the surface and the cantilever tip and this alteration will lead to changing the oscillation amplitude. The level of the amplitude change across the sample is probed by the optical detector. Usually the tip-sample interaction induces a reduction δA in the amplitude oscillation. The feedback loop is used to maintain the amplitude of oscillation A of the cantilever by adjusting the position of the cantilever with respect to the sample (or vice versa). This (approximately) will yield to traces of a constant tip-sample distance.

In tapping mode, additional information about the sample properties can be inferred from the change in the phase of the oscillation. Phase imaging monitors the phase lag between the signal that drives the cantilever to oscillate and the measured cantilever oscillation. Variations in a number of surface properties including elasticity, adhesion and friction can cause change in the phase of the oscillation and therefore affect the phase lag. Additional characteristics of a biomolecular surface can therefore be probed simultaneously to the topographic features. This can be used for example, to distinguish variations in the lipid composition of a bilayer which appears perfectly flat in topography but contains two phases of lipids.

On the other hand, the major drawbacks for tapping mode imaging in fluid are: (i) the reduction of the quality factor of the cantilever Q by the viscous damping of the fluid. This reduces the sensitivity of the method in changing the amplitude because a small shift in f_0 in liquid produces a much smaller δA comparing with in air. (ii) The cantilever is usually driven by a piezo actuator as explained in section 2.3.6.1. This actuator drives the entire fluid cell, or cantilever holder leading to the production of mechanical resonances in the fluid cell, in addition to the cantilever. This results in an excitation spectrum that is commonly denoted as a `forest of peaks' as shown in figure 2.13. This forest of peaks varies while imaging as the fluid changes within the fluid cell. This can result in large changes to the amplitude of the cantilever resonance peak as the forest of peaks moves [137]. Changes to the free amplitude of oscillation of the cantilever will result in changes in the load force and the resolution.

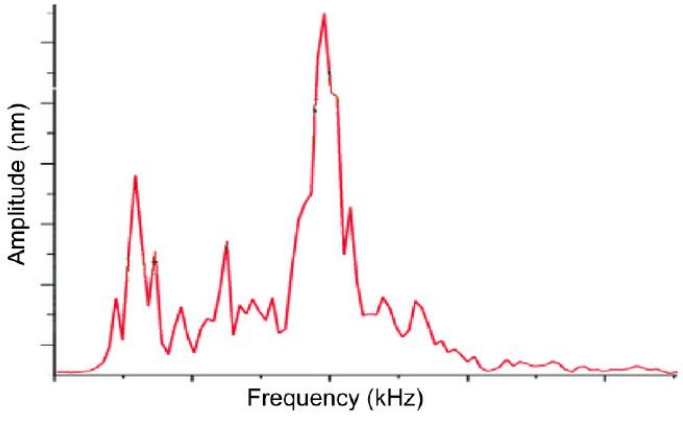

Figure 2.13: A plot of actuation amplitude versus frequency for a cantilever with f_0 ~ 550 kHz showing the forest of peaks introduced by the actuation of other mechanical resonances [3].

These are the major drawbacks for the imaging of biomolecules in fluid using tapping mode. Although the lateral forces in tapping mode are reduced, the applied force is in fact less-defined and can vary. The large changes in applied force can result in a loss of resolution, or damage to the sample or to the tip, which is another key for high resolution imaging using the AFM.

2.3.4.3 Peak Force AFM in Liquid

Peak force is a relatively new technique developed by Bruker (Bruker, Santa Barbara, USA) where the topographical image coupled with information about the mechanical properties of the surface are gathered simultaneously [138]. This is achieved by applying a series of force curves at a frequency significantly lower than the resonance frequency of the cantilever

[139]. For imaging in fluid, the tip is `tapped' on the surface in a sinusoidal motion at amplitudes that are typically less than 10 nm, at frequencies of 1-8 kHz. The tip-sample interaction is controlled by maintaining the maximum force, or `peak force', between the tip and the sample constant.

The force curves taken at each point on the surface allow precise control of the tip-sample interaction force, enabling imaging at peak forces of less than 200 pN, and as low as 30 pN in fluid environments. This helps protect both the AFM probe and the sample from potential damage and is a key factor in enabling high-resolution imaging.

Peak force tapping also allows to probe mechanical properties of the sample, including adhesion, dissipation, deformation and elastic modulus [140] [141]. The typical force curves are acquired by vertically approaching the tip from the sample, pressing on it with a set force causing a deflection of the cantilever and then retract from the sample. The force curve, shown in the figure 2.14.iv, is highlighting the way of calculating these mechanical properties of the surface. In the peak force tapping mode, the surface is scanned and represented in different ways. It could be represented in height so the topographical image is generated. The image could alternatively be generated to represent any of the mechanical properties mentioned above.

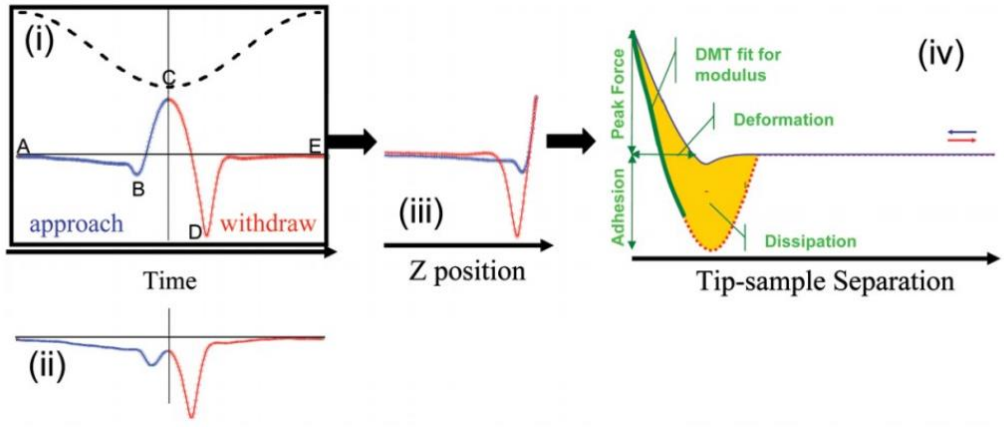

Figure 2.14: A schematic showing the data collected from an instantaneous Peak Force Tapping force curve, reproduced from reference [15]. Plot (i): Force (blue-approach and red-retract) and z-piezo (dotted) position as a function of time, where B is the jump to contact, C is the Peak Force, D is the Adhesion force. (ii) A force versus time plot with small peak force. (iii) A force versus z position plot. (iv) Force versus tip sample separation plot showing the different parameters calculated in Peak Force QNM.

2.3.5 Cantilevers

Cantilever properties as well as the tip shape have a vital role in increasing the imaging resolution. This is because force sensitivity is a key for increasing the imaging spatial resolution, which is directly related to the mechanical properties of the cantilever. In other words, the cantilever stiffness determines the sensitivity for force applied to the sample while imaging. The stiffer the cantilever, the less the force sensitivity, which could lead to sample deformation and/or less responsiveness to track the small topographical changes of the sample leading to poor resolution [1, 142].

2.3.5.1 Mechanical Properties of the Cantilever

For imaging of biomolecules in fluid in contact mode, tapping mode and peak force tapping mode, soft cantilevers are used to obtain high force sensitivity, minimising the load force on the sample.

In the contact mode for instance, usually soft cantilevers are used with ~ 0.01 N/m spring constant to be as soft as possible on the sample to avoid any damage. In tapping modes however, it is recommended to use stiffer cantilevers with 0.05-0.5 N/m spring constant.

There is on-going research to improve the cantilever properties. For example, smaller cantilevers allow for higher resonance frequencies while maintaining a low spring constant, facilitating faster or more sensitive measurements.

2.3.5.2 Small Levers

Small cantilevers have been predicted to yield improvement in image stability, imaging speed and reduction of the thermal noise. Compared to conventional cantilevers, small cantilevers show up to 5 times improvement in force sensitivity [143]. Much work on these cantilevers has been done in the context of high-speed AFM using tapping mode [144].

Traditionally, small cantilevers have been difficult to manufacture, however, they are now commercially available with high resonance frequencies [145-147]. Figure 2.15 shows the size difference between a conventional cantilever (100's of µm) and a small cantilever (~20 µm).

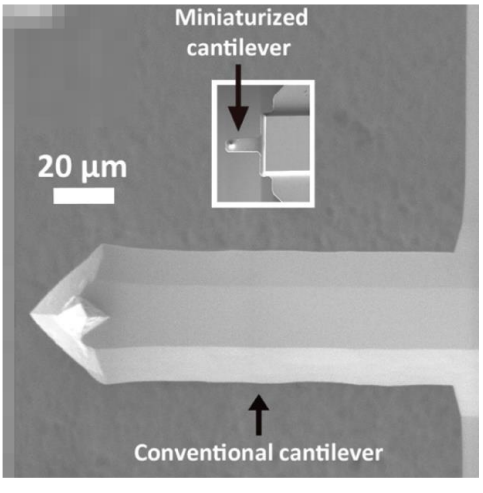

Figure 2.15: Scanning electron microscopy image of a small cantilever compared to a conventional NCH cantilever. Image reproduced from [1].

There are however a number of drawbacks for small cantilevers that might limit their use. Usually when the cantilever approaches the sample surface, the resonance frequency f_0 does not stay constant and this is more pronounced with small cantilevers. This is because of the interaction between the cantilever beam and the sample surface leading to hydrodynamic damping of the cantilever. This results in a less clearly defined force baseline above the sample [1].

In addition, it is difficult to fabricate a sharp tip at the end of a small cantilever. Larger tips however have masses that contribute more heavily with respect to the overall weight of the cantilevers which reduces the resonance frequency f_0 [133], but more importantly, it is harder to align the tip to the end of the cantilever in a batch fabrication process. Alternatively, carbon tips can be grown on the end of these cantilevers. This alteration largely increases the cost of manufacturing, and it has been shown that in some cases such tips reduce the resolution by affecting the interaction strength with the sample [148].

2.3.5.3 Tip

The cantilever tip also has a large effect on image resolution. By definition, each image is a convolution of the tip shape and the sample topography. For this reason, tip sharpness has been identified as a key component to increase the imaging resolution. The smaller the radius of the tip, the finer topographical details of the scanned surface can be resolved [149]. In addition, tip apex and aspect ratio are relevant to imaging resolution for larger biomolecules [1]. The convolution with the tip apex is responsible for the broadening effects that are observed in most AFM images, and that lead to an overestimation of the lateral dimensions of measured objects [150].

In addition, the higher the aspect ratio of the tip, the less the interactions are allowed between the tip's walls and the sample. This will minimise the extra forces arise that can alter the real topography of the scanned surface.

Ideally, the tip is preferred to be a sharp needle with a radius of less than a nanometre. Indeed a carbon nanotube with such narrow diameter mounted on a flexible cantilever was achieved. However, the manufacturing of carbon nanotube tips has considerable obstacles which results in high cost [151].

The most commonly used cantilevers are silicon with silicon tips or silicon nitride with silicon tips as shown in figure 2.16.

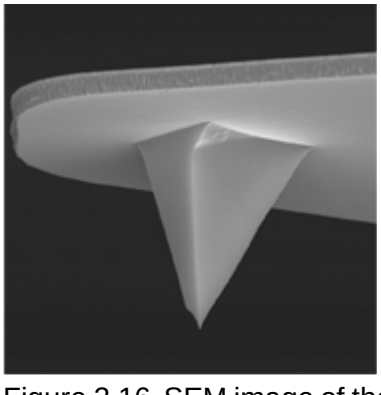

Figure 2.16 SEM image of the silicone nitride tip of a conventional the MSNL cantilever manufactured by Bruker (image taken from the company website)

Table 2.2 shows the specifications of the cantilevers mainly used in this project, and the operational mode they were used for.

Cantilever Type	k (N/m)	f_0 (kHz)	R (nm)	Mode Used
MSNL-C	0.01	1.5	2	Contact
MSNL-D	0.03	4	2	Contact
MSNL-E	0.1	6	2	Tapping/PFT
MSNL-F	0.6	40	2	Tapping/PFT
Fastscan DX	0.25	110	8	Tapping/PFT

Table 2.2: Nominal specifications for spring constant k, resonance frequency in fluid f_0, tip radius R and mode of imaging employed, for the cantilevers used in this project.

2.3.6 Cantilever Actuation

As mentioned in section 2.3.4.2, AFM imaging using tapping mode requires oscillating the cantilever at a particular frequency above the surface of the sample. This is also called cantilever actuation and is performed by an actuator. This actuator has to facilitate a stable and reproducible cantilever signal for measuring the tip sample interaction.

There are two cantilever actuation methods employed in this project: (piezo)mechanical actuation and photothermal or optical actuation.

2.3.6.1 Cantilever Mechanical Actuation

In the (piezo)mechanical method of actuating the cantilever, it is typically driven by a piezoactuator in the fluid cell. However, this has drawbacks in liquid where the cantilever resonance is convoluted with the other mechanical resonances of the fluid cell causing a `forest of peaks' as discussed previously. This affects imaging because the force exerted by the cantilever on the surface cannot be easily and precisely monitored during experiments, a problem the drifting of the `forest of peaks'.

2.3.6.2 Cantilever Optical Actuation

The optical method for actuating the cantilever was developed to solve the `forest of peaks' problem associated with the piezomechanical method, leading to more clearly defined cantilever resonance and more stable actuation. In the optical method, the cantilever is directly actuated without exciting the support chip or the fluid cell, thus avoiding the spurious resonances that are typical of piezomechanical actuation. This is achieved by focusing a modulated actuation laser on the cantilever surface. Due to the composite nature of most AFM cantilevers (silicon or silicon-nitride lever covered with a metallic coating) and their resulting propensity to bend [152], they can be actuated and brought to resonance by laser heating [153, 154].

The advantages of this optical actuation method over the other non-mechanical ones is that it does not require any electrical connections or any corrosive coatings for cantilevers and fluid cells, making it a convenient technique for use in fluid. In addition, the laser modulation allows the use of both small cantilevers with a range in ~MHz resonance frequencies, [148, 155], as well as the standard cantilevers.

The drawback however of optical actuation is that the achievable range of tapping amplitudes is usually small [153].

In this project, we have employed optical actuation for fast scan imaging using small Fastscan DX cantilevers with a spring constant of ~0.25 N/m. The cantilever actuation performed via a modified AFM head designed for the photothermal actuation of miniaturised cantilever [156, 157].

2.3.7 Optimising AFM Parameters for Imaging Model Membranes

As discussed in section 2.2.4, supported lipid bilayers were formed on a mica substrate to mimic bacterial membranes. These supported membranes are considered soft biological samples and imaging it by AFM requires careful operation. This is mainly due to the risk of damaging the membrane by the AFM tip while imaging.

As stated in equation 2.3, in order to calculate the precise force applied by the tip on the sample, the cantilever spring constant has to be measured. In addition, it is essential to calculate the precise spring constant of the cantilever, if one wishes to determine the mechanical properties of the sample surface. Usually, the theoretical spring constant of a cantilever is provided by the manufacturer of the cantilever. However, the precise spring constant could vary from one cantilever to another. There are different ways to measure the spring constant of the cantilever. The method usually employed in this research is the thermal fluctuations method [158].

Our imaging is usually aimed to be performed with forces lower than or approximately equal to 100 pN. The imaging starts by approaching the tip to the sample surface with an approach setpoint slightly higher than the imaging setpoint, to avoid an erroneous detection of a tip-sample contact ('false engage'). To assure an optimum minimum force is applied, after the tip is engaged with the sample surface, the force again was gradually reduced until a total dis-engage occurred. Finally, the force was increased again very slowly until the tip engaged again with a reasonable minimum force. This force was determined from the quality of the imaging, which can be monitored by the "trace" (left to right) and "retrace" (right to left) line profiles. Regardless the typical noise level of ~few Å, an optimum force should result in a stable and overlapped trace and retrace spectra. Once an optimum force is found, a larger scan area 1-3 µm can be set.

2.3.8 Characterisation of Bacterial Model Membranes

The prepared model membranes were subject to characterisation process before using them for testing and studying the mechanisms of antimicrobial peptides.

To achieve a clean flat membrane surface, it was essential to assure that all the materials and equipment used are clean and free of contaminations. This includes the lipid, the buffers, the mica discs, the fluid cell and the cantilevers.

Clean bilayers formed using (DLPC:DLPG) lipids are expected to be flat with no topographic features [2, 159]. This flatness is because both lipids have the same length and they have similar transition temperature, hence they mix well. The flatness of the membranes was often investigated by AFM at different areas across the sample.

To assure that the imaged flat surface is a lipid bilayer and not the (nearly equally flat) mica disc surface, force curves were recorded with minimum force load and then at gradually increasing force load until the tip penetrates the bilayer, showing a step down within the force curve. Figure 2.17 shows a verification of the presence of a lipid membrane on a mica surface. Figure 2.17.A displays a flat surface imaged by peak force tapping mode. A force curve was performed on the area highlighted by the white circle. Figure 2.17.B shows the approaching and retracting curves of the performed force curve. The approach curve shows the breakthrough event highlighted by the black circle. This breakthrough is a typical event when the cantilever tip penetrated the soft lipid bilayer to reach the solid surface of the mica substrate.

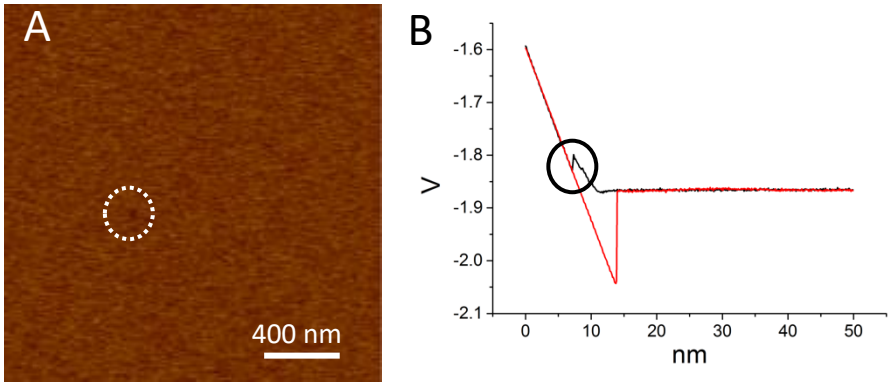

Figure 2.17: Force curve verification of the presence of a lipid bilayer on a mica surface. A) A peak force tapping AFM image of a supported lipid bilayer. B) A force curve taken on the DLPC:DLPG (3:1) lipid bilayer surface with a breakthrough event (marked by the black circle) confirming the presence of the lipid bilayer.

This verification process via applying force curve was avoided if not necessary as it can cause tip contamination and thus affects the spatial resolution. By following exactly the same protocol for membrane preparation, the same clean and flat membrane was achieved without the need to check it every time.

DLPC:DLPG membranes have a thickness of about ~ 3.2 nm [159, 160]. This thickness could slightly be influenced by the temperature [161], pH and the salts exist in the buffer [162].

In order to measure the depth of this bilayer, we need to know what we call the (sensitivity calibration of the cantilever) to convert the deflection of the cantilever from volt to distance. This sensitivity value varies from cantilever to another and the calibration must be performed every time we need this value. Once this calibration is done, We find, by measuring the little step in the middle of the deflection curve that the bilayer depth is about 3 nm, matching the value of the expected depth of DLPC:DLPG lipid bilayers.

A non-complete coverage of the mica by the SLB is also possible. This would result in step-wise changes of ~3 nm height. It usually happens when the amount of the lipid vesicles injected on the mica is not enough to cover entirely the mica surface, leaving the mica partly uncovered. Such phenomena were avoided by injecting enough lipid vesicles to completely cover the mica.

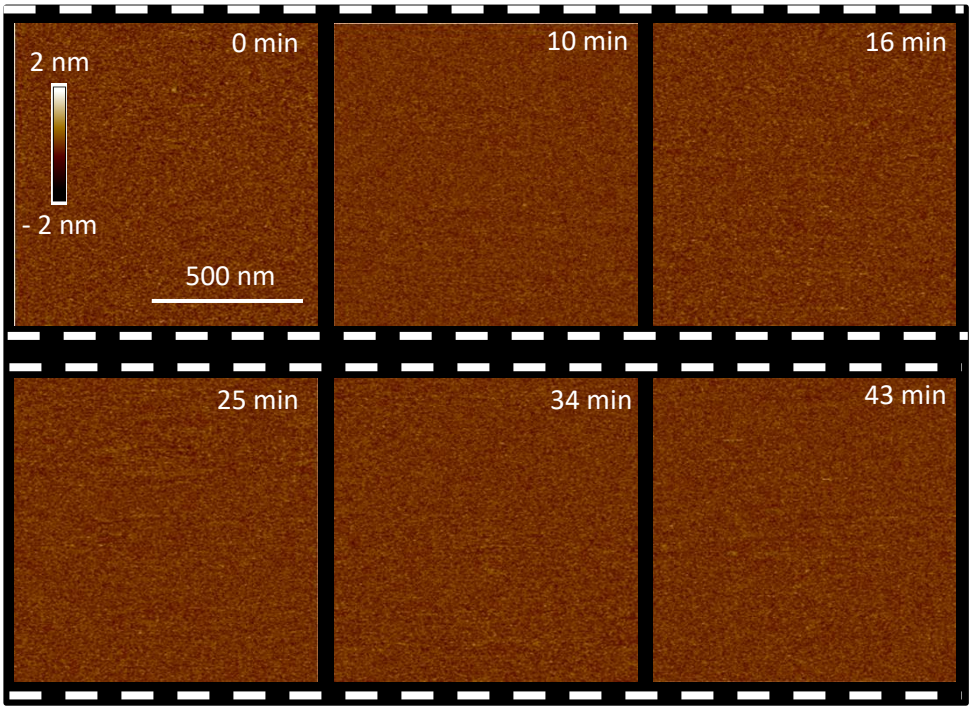

Figure 2.18: AFM images of a DLPC:DLPG (3:1) lipid bilayer surface imaged in buffer solution over the course of an hour.

To test the effect of antimicrobial peptides on the formed lipid membranes, we also need to verify that imaging itself does not alter or change the membrane topography.

To confirm that AFM imaging does not deform the lipid model membrane, continued imaging on the same area of the membrane surface was performed over a course of an hour as shown in figure 2.18. The images show no considerable change in the topography or flatness of the membrane surface. This confirms that the membrane is immobilised well on the substrate and that the imaging operation is soft enough to avoid any deformation.

This confirms that under the same conditions, and after injecting the studied peptides on the membrane, any topographical change or deformation of the membrane can be attributed to the peptides.

2.3.9 Image Processing

NanoScope Analysis (1.5), (1.7) and Gwyddion (2.34) are the software items used in this thesis to process the AFM images. Often, the first tool employed to process all AFM images is 1st or 2nd order plane subtraction, to remove background tilt of curvature.

In addition, we use line by line background subtraction, often called flattening, which aims to correct any remaining tilt or curving in the scan lines and to compensate for sudden line-to-line changes in the imaging process.

This plane subtraction and flattening tools can be applied on the whole image or on a selected area of the image that requires correction. As the images could include features like holes or aggregations, flatting was usually applied while a mask tool is performed to eliminate these features from the background fitting procedure.

Once the image is process, the analysis tools were used to study the features shapes and dimensions.

Chapter 3

Alpha Helical Antimicrobial Peptides

3.1 Introduction:

As discussed in chapter 1, many natural antimicrobial peptides adopt α-helical structure on bacterial membranes [163]. Natural helical AMPs include cathelicidins, cecropins, magainins, dermaseptins and buforins [164]. Helical AMPs interact with the bacterial membranes and many of them form pores causing cell lysis. The poration mechanisms, however, vary between the different peptides. While relatively few are studied in detail [165], it is still not obvious to understand the relation between the peptide sequence/structure and the mechanism by which the helical AMPs attack the bacteria. This chapter aims to provide an insight into this relation. Combined with the known structures and mechanisms of some natural AMPs, such an insight can facilitate the design of improved AMPs based on modified sequences of well understood peptides. Here, we will compare two synthesised peptides each with a sequence of 21 amino acids. They are both designed to form α-helices when interacting with the bacterial membranes. The only difference is that in the first one, called amhelin, all the positively charged amino acid used in the sequence are lysines (L), while in the second one, called tilamin, only three of them are lysines and the other six are arginines (R). Our collaborators in NPL have prepared both peptides and determined their structure using different techniques and investigated their biological activity against bacteria, as published in references [22, 159] and briefly reviewed below. The next sections then describe the AFM experiments carried out as part of this PhD research to determine their mechanism of action.

3.2 Amhelin Peptide

3.2.1 Amhelin Design and Structure

Amhelin is a *de novo* amino acid sequence designed according to the heptad model (PPPHPPH) [166] where (P) corresponds to a polar amino acid and (H) corresponds to a hydrophobic amino acid, with the sequence containing three PPPHPPH repeats. Figure 3.1.A shows the amhelin amino acid sequence highlighting the polar (P) and the hydrophobic (H) residues (top) and the cationic (C) and the neutral (N) residues (bottom) at neutral pH. As a unique feature of helical AMPs, the positively charged peptide is expected to preferentially interact with the negatively charged bacterial membranes and to fold into an amphipathic helical structure.

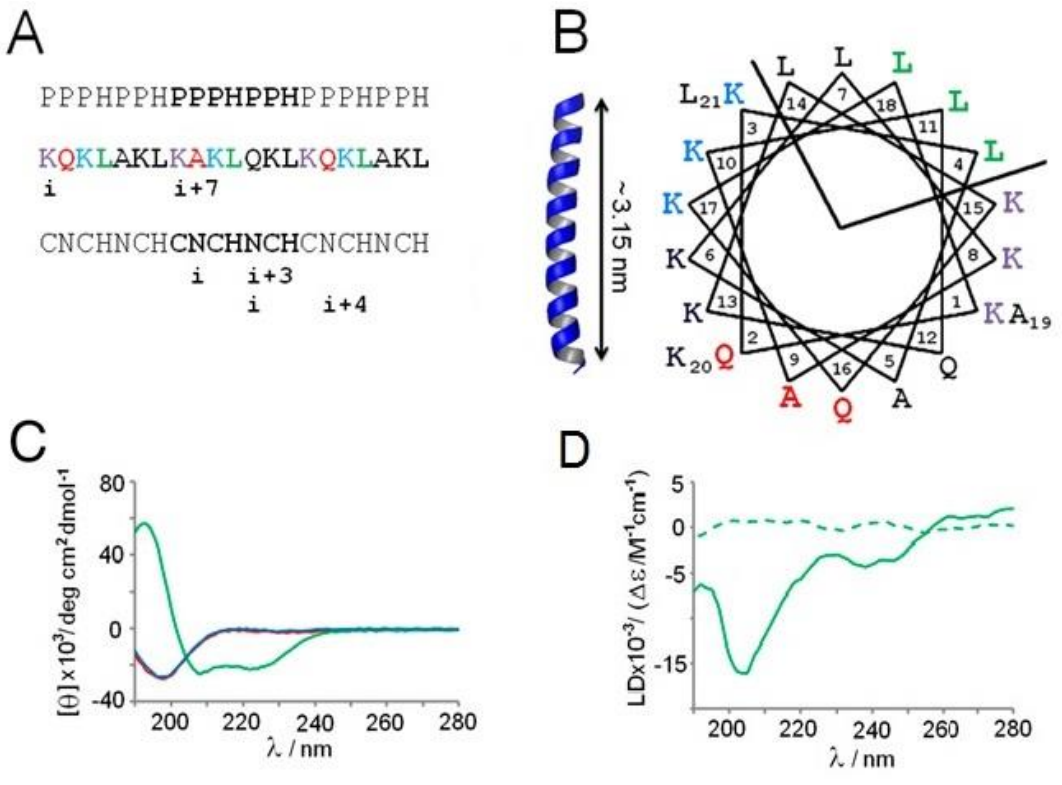

Figure 3.1: Amhelin peptide sequence and secondary structure characterisation. (A) Amhelin amino acid linear sequence (middle) with the tokens of polar (P) and hydrophobic (H) amino acids (top), and the tokens of cationic (C) and neutral (N) amino acids (bottom). (B) Amhelin peptide as a helical wheel showing an amphipathic helix spanning ~3.15 nm (in blue, 2ZTA PDB entry [21], rendered with PyMoL). (C) CD spectra of amhelin (20 μM) in 10 mM phosphate buffer, in the absence (red line) and presence of ZUVs (blue line), both red and blue spectra are overlapped, and in the presence of AUVs (green line). (D) LD spectra of amhelin (solid line) and the non-AMP (dashed line) (both at 20 μM) in AUVs.

Thus targeting bacterial membranes, the peptide is antimicrobial against a wide range of bacteria. The expected secondary structure of the peptide is represented in figure 3.1.B, showing a top-down schematic view. It is presented like a wheel with the amino acids side-chains protruding out of the peptide cylinder. This representation is highlighting the hydrophobic side along the peptide (located within the acute angle), attributed to leucines (L). All the other amino acids are aligned on the other side of the peptide cylinder (located around the reflex angle) and are hydrophilic. The length of the folded helix is about 3.15 nm attributed to 0.54 nm per turn.

To confirm the helicity of the peptide, circular dichroism (CD) spectroscopy [167] was carried out on three different samples. The first sample is a control consisting of amhelin peptide in

buffer solution. The second sample is amhelin peptide with the presence of zwitterionic unilamellar vesicles (ZUVs) formed by the neutral lipid (DLPC). This lipid composition mimics eukaryotic cell membranes [111]. The third sample is amhelin peptide in the presence of anionic unilamellar vesicles (AUV) formed by a mixture of two lipids; (DLPC:DLPG) with the mass ratio of (3:1) respectively. As mentioned in chapter 1, this lipid composition mimics prokaryotic (bacterial) cell membranes. The CD spectra of the control sample (amhelin in buffer) and the second sample (amhelin in buffer with neutral vesicles) are hardly distinguishable and show a negative signal near 195 nm confirming the disordered peptide structure [168], figure 3.1.C. On the other hand, the spectrum of the third sample (amhelin in buffer with negatively charged vesicles) shows a positive signal at 193 nm and negative signals at 208 and 222 nm. These features are signatures for peptides with helical structure [168]. The CD data therefore confirms that amhelin folds into the amphipathic helical structure only when interacting with the negatively charged bacterial membrane.

To understand the mechanism by which antimicrobial peptides interact with the bacterial lipid membrane and eventually disrupt it, it is important to know the orientation of peptide helices with respect to the membrane. To probe this, linear dichroism (LD) [167] spectroscopy was used for two different samples. The first sample is the amhelin peptide and the second sample is a control that includes a peptide that is not antimicrobial (non-AMP), both measured in the presence of anionic unilamellar vesicles (AUV). The LD data shows that the spectrum of amhelin presents peaks at 190-195 nm and 220-230 nm, and a minimum at 205-210 nm. These bands are indicative that the peptide is inserted in the lipid vesicles figure 3.1.D solid line; the spectrum of the non-AMP peptide shows no signals meaning that it cannot bind and orient itself in any specific direction with respect to the membrane, figure 3.1.D dashed line [169].

3.2.2 Biological Activity of Amhelin

As mentioned above, amhelin was designed as an antimicrobial peptide. To determine its activity against bacterial cells, a live/dead-stain (propidium iodide, PI) assay [170] was performed on two samples. The first sample was a control consisting of *E.coli* bacteria incubated with a non-AMP. The second sample was *E. coli* incubated with amhelin. The fluorescence data figure 3.2.B, show that for the control experiment and over 50 minutes of incubation, the number of the dead cells (red spots) has not considerably increased.

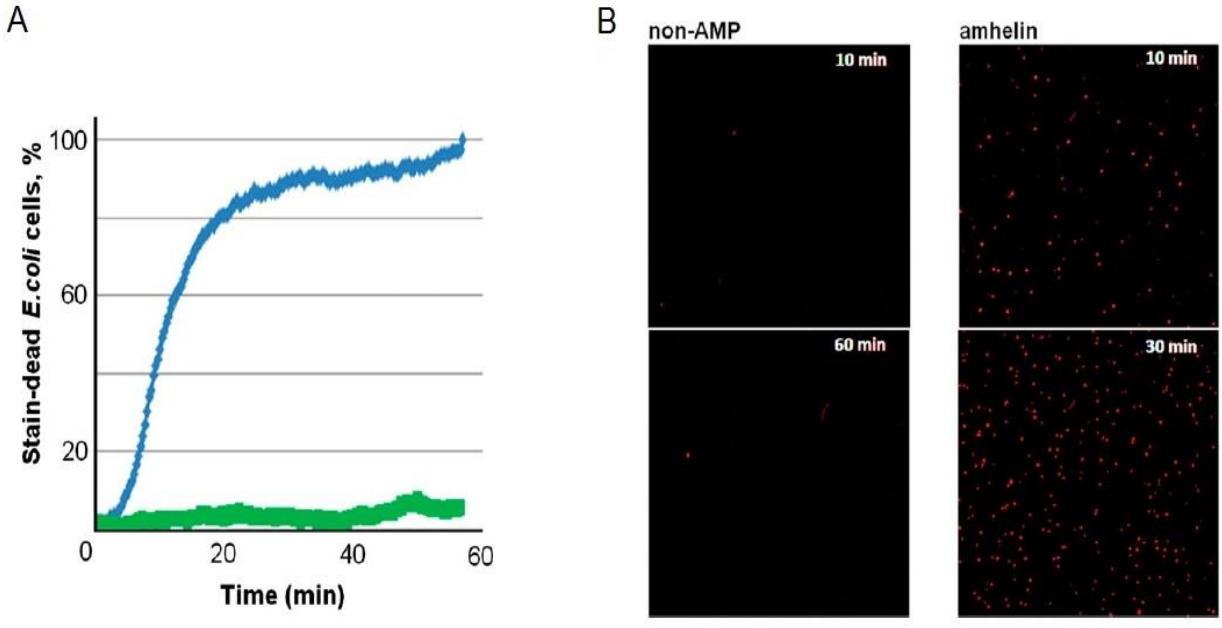

Figure 3.2: Amhelin biological activity. (A) Average number of stain-dead cells incubated with amhelin (blue) and the non-AMP, QIAALEQEIAALEQEIAALQ (green), as a function of time. (B) Fluorescence microscopy images of PI-stained E. coli cells. Incubation conditions: 10 µM peptide, 30 min, at OD600nm = 0.008.

On the other hand, many dead cells appeared after 20 minutes of incubating *E. coli* with amhelin. A quantitative analysis of these results shows that amhelin can reach up to a 100 % efficiency in killing *E. coli* within 60 minutes incubation, compared with the non-AMP peptide, which showed no significant effect, figure 3.2.A.

To verify that amhelin shows similar antimicrobial activity against different bacteria, the standard minimum inhibitory concentration (MIC) assay [171] was performed on different types of bacteria, shown in table 3.1. *E. coli* and *P. aeruginosa* are Gram-negative bacteria, while the other three, *B. subtilis, S. aureus* and *M. luteus*, are Gram-positive.

The data shows that amhelin exhibited antimicrobial activity against gram-negative and gram-positive bacteria with MICs that are typical of AMPs [172]. On the other hand, the data shows negligible lytic activity against human red blood cells, see table 3.1. This confirms that amhelin is not toxic to human cells at the studied level of antimicrobial concentrations.

Bacterial Strains	Minimum Inhibitory Concentration (MIC), µM
E. coli (K12)	3
P. aeruginosa (ATCC 27853)	12
B. subtilis (ATCC 6633)	6
S. aureus (ATCC 6538)	>50
M. luteus (NCIMB 13267)	<12
Eukaryotic Cells	LC_{50} [a]
Human erythrocytes	>>600

Table 3.1: Biological Activity of amhelin. Minimum inhibitory concentration assay for amhelin applied on different bacterial strains including Gram-negative bacteria (in red) and Gram-positive bacteria (In blue) as well as on human cells. [a] Median lethal concentration

3.2.3 Effect of Amhelin on Bacterial Membranes

To determine the mechanism by which amhelin attacks the bacterial membrane, atomic force microscopy (AFM) was used. AFM was first applied on dried samples – by our collaborators at NPL – to image amhelin-treated bacterial cells (Escherichia coli) [159]. The images revealed some surface corrugation, but the interpretation of pore-like structures was complicated because of the intrinsic roughness of the damaged bacterial surface.

To circumvent this problem and to facilitate real time AFM imaging, bacterial model membranes were used instead of whole bacteria, and the effect of amhelin was imaged on these membranes in liquid. Specifically, a supported lipid bilayer was chosen to mimic the negatively charged bacterial membrane. As mentioned in chapter 1, the flatness and less stickiness of the supported lipid bilayer allow more stable AFM scanning and yield clearer images.

The lipid used is a mixture of DLPC:DLPG, with a mass ratio of (3:1), and the bilayer was prepared as explained in chapter 2.

Once the flat lipid surface was prepared and characterised by AFM, the concentration of amhelin peptide to cause a discernible effect on the lipid bilayer was determined by trial and

error. The challenge was to find the concentration of the peptide at which the kinetics of membrane disruption was accessible within the time resolution of AFM imaging. Unsurprisingly, the rate at which the peptide attacks the membrane strongly depends on concentration and temperature.

A high peptide concentration will lead to a rapid destruction of the lipid bilayer, and the AFM will not be able to track it. A very low concentration of the peptide, on the other hand, will lead to a very slow process and the subsequent AFM images will show no significant changes. The desired concentration for our mechanism-understanding purpose will lead to a relatively gradual and continued disruption of the membrane over the time scale of the AFM experiments.

Figure 3.3 shows an example of an experiment where a high concentration of amhelin was applied to the lipid bilayer. It first shows a flat (DLPC:DLPG) negatively charged lipid bilayer imaged in buffer before adding any amhelin. The flatness of the bilayer is confirmed by the height profile bellow the image, showing only noise of at most a few Å on the vertical (*z*) scale. At time zero, amhelin was added at a concentration of 0.75 µM. Figure 3.3.B is an image of the lipid bilayer after 18 minutes. The image shows a complete disruption of the membrane, as also evidenced in the height profile.

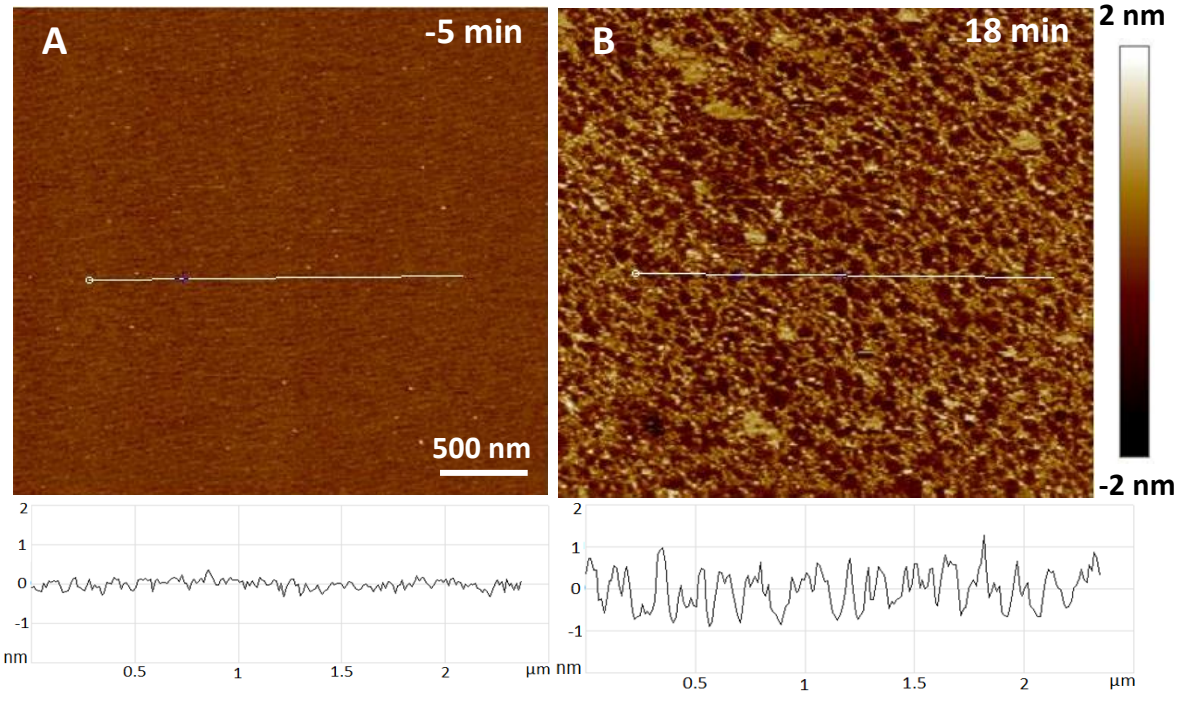

Figure 3.3: The effect of high amhelin concentration on bacterial model membrane. (A) In liquid AFM Image of flat DLPC:DLPG (3:1 W:W) lipid bilayer. (B) Same sample but after incubating with 0.75 µM amhelin. Amhelin was injected on the sample at time 0 min. Buffer: 20 mM HEPSE + 150 mM NaCl pH≈7.4.

The more appropriate concentration of amhelin for AFM imaging was then determined to be 0.5 µM.

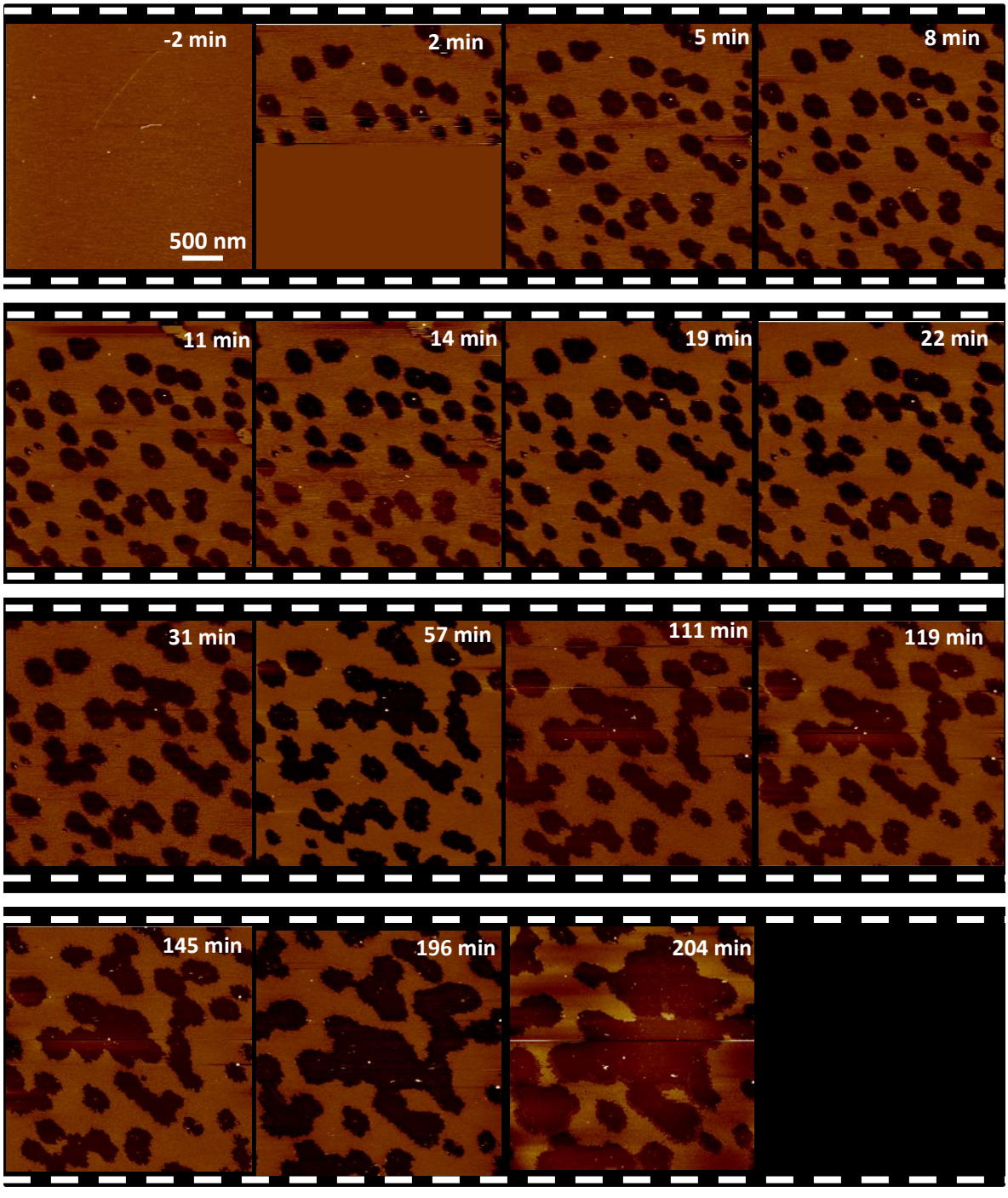

Figure 3.4: Time-lapse AFM images of DLPC:DLPG (3:1 W:W) supported lipid bilayer incubated with 0.5 µM amhelin. Amhelin was injected on the sample at time 0 min. The first image was acquired before the treatment with amhelin and shows a flat bilayer. The sample was prepared in a buffer of 20 mM HEPES and 150 mM NaCl, PH≈7.4. The experiment was carried out at room temperature

To monitor the effect of amhelin, multiple sequential topographical images were recorded on the same area of the bacterial model membrane. Figure 3.4 shows time-lapse images of the DLPC:DLPG (3:1 mass ratio) lipid bilayer and the degradation process following the addition of 0.5 µM amhelin. The first image was taken before the treatment, showing a flat lipid bilayer.

The effects of amhelin appeared instantly after injecting into the sample at time 0 min. The images show roughly circular pores that expand to gradually lead to a nearly complete removal of the membrane after about 3 hours. The pore expansion occurred in two ways, with single pores expansion in size and with different pores merging. The depth of the pores is consistent across the images, at about 3 nm as shown by the height profiles of three different pores figure 3.5.B. This pore depth was further confirmed by a heights analysis over a complete image of the same sample. Figure 3.5.C. The height histogram shows to main peaks corresponding to the two major heights recorded over the sample surface: the membrane surface at 0 nm and the substrate surface (pores) at ~ -3 nm.

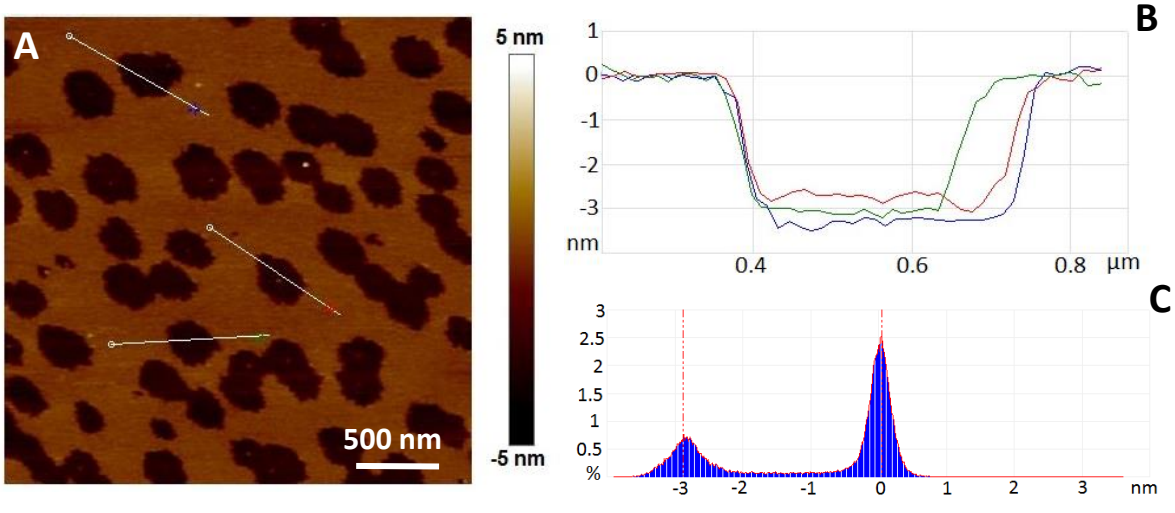

Figure 3.5: Pores characterisation from by amhelin in bacterial model membrane. (A) AFM topography image of DLPC:DLPG (3:1) supported lipid bilayer incubated with 0.5 µM amhelin over 5 minutes (taken from figure 3.4). (B) The corresponding cross section profiles drown on the image over three different pores showing consistent pores depth of ~ 3 nm. (C) Histogram profile of the image heights. Height (0 nm) represents the membrane surface while (-3 nm) represents the substrate..

To interpret these results in terms of a poration mechanism, we have to elaborate on two key intrinsic features of amhelin peptide.

The first feature is the overall positive charge of the peptide, which is attributed to the nine lysine residues in its sequence. The isoelectronic point (pI) of lysine is 9.94 meaning that at the physiological, neutral pH (~7), lysine residues will be protonated giving the peptide a net positive charge of (+9). The second feature is the ability for the peptide to form an amphipathic structure caused by the segregation of the hydrophobic and hydrophilic faces. To avoid toxicity to human cells, the hydrophobic face, which is attributed to leucine residues, was designed narrow comparing with the positive face attributed to lysine with a ratio of (1:1.5) (Leucine:lysine) respectively. The haemolytic activities assay confirmed the apparent non-toxicity which is common for venom peptides to human cells. These toxic peptides normally have broader hydrophobic clusters [79, 173]. To maintain the ratio of 1:1.5 mentioned above within the amhelin sequence, small alanines and neutral glutamines, which do not contribute to membrane binding, were alternately arranged in the polar face as a neutral cluster opposite to the hydrophobic face. The resulted secondary structure of the peptide helices is then stabilised by inter- and intramolecular forces upon binding to the bacterial membrane.

The positively charged peptides first interact electrostatically with the negatively charged bacterial membrane and fold into amphipathic helices. At this state, which we call S-state, figure 3.6, amhelin helices remained stable for a time (< few seconds) that is too short to be resolved in these AFM experiments. To support this interpretation, molecular dynamics simulations were carried out to show that amhelin helices remained stable with slightly tilted orientations over timescales of 100 ns [159]. In this S state, the hydrophilic and positively charged side of the peptide face the membrane, while the hydrophobic (leucine) side is exposed out to the water, implying an energetically unstable state. This is forcing the peptide to induce tension on the membrane surface seeking stabilisation.

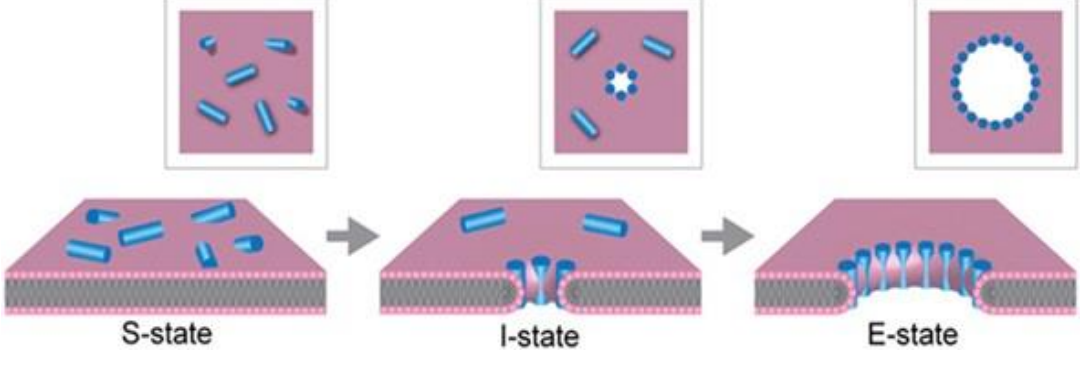

Figure 3.6: Proposed pore expansion mechanism for amhelin as an amphipathic antimicrobial peptide. Amhelin peptides (blue cylinders) first bind to the surface of the membrane (S-state), then insert into the lipid bilayer forming pores (I-state), which can then expand (E-state).

When the tension is large enough, it leads to membrane poration. The first recorded AFM image after adding amhelin to the sample was after two minutes, figure 3.4. The image shows pores that have already developed to a diameter of around 300 nm. These AFM images therefore do not track the pore formation in the very early stage (the first two minutes) of the attack. The molecular dynamics simulations, however, showed that the poration primarily starts with hexameric and octameric pores constructed in the bilayer, which we call (I-state), figure 3.6. The root-mean-square displacement (rmsd), which is a measure of differences between values predicted by a model and the values actually observed, demonstrates that the expansion of pores double in diameter over timescales of order 100 ns [159]. In this state, the peptide helices align together in a bundle and stabilise by the intramolecular forces forming almost circular pores which is the lowest energetic state possible. The hydrophilic sides are aligned toward the core of the pores, exposed to the aqueous medium, while the hydrophobic side is hidden inside toward the hydrophobic fatty acid chains of the lipids. The length of the peptide helices is matching the thickness of the lipid bilayer (~3nm), making it difficult to identify the peptides themselves in the AFM height profiles. However, the edges of larger pores were shown to be lined with helical peptides by high-resolution secondary-ion mass spectrometry (SIMS) [159]. In that experiment, amhelin which was ^{15}N-labeled at alanine and leucine residues, and attacked the membrane under otherwise similar conditions. SIMS images showed a higher signal intensity from regions of the surface rich in peptide, which were found at the edges of the pores.

Finally, our AFM images indicated that these peptide bundles that triggered the pores in I-state allowed more and more peptides to join making wider pores in a state that we call E-state figure 3.6. This evolving state is attributed to the fact that the intramolecular forces (peptide-peptide and peptide-lipid) are not rigid enough to arrest the initiating pores in I-state. As the diffusion of peptides across the membrane available, the complete rupture of the membrane eventually occurred by either a continued expansion of individual pores or by pores merging.

3.3 Tilamin Peptide

3.3.1 Tilamin Design and Structure

Tilamin was also designed to be a three repeats of the heptad model (PPPHPPH) where (P) and (H) are polar and hydrophobic amino acid residues respectively. Tilamin however differs from amhelin in the positively charged amino acid used in the sequence. In tilamin, six of the positively charged amino acids in the sequence are arginines (R) and only three of them are lysines as shown in figure 3.7.A. The aim of this change is to understand whether such a small tweak in the amino acid residues will change the structure of the peptide assembly under the same conditions as well as its antimicrobial activity and the mechanism of action. Similar to amhelin, the amino acid arrangement in tilamin allows the peptide to fold into a ~3 nm helix when interacting with the bacterial membranes. The folded structure makes a segregation of the hydrophobic and the hydrophilic residues along the peptide cylinder leading purposely to an amphipathic assembly. The proposed folded secondary structure of tilamin is presented schematically in figure 3.7.B. Leucine (L) residues are aligned on one side of the peptide cylinder highlighted by the arc while the hydrophilic residues are on the other side of the peptide cylinder.

The helical structure of tilamin was confirmed by CD spectroscopy. In these experiments, four different samples were examined to produce a CD spectrum for each shown in figure 3.7.C. These four samples were; tilamin in phosphate buffer, tilamin mixed with anionic unilamellar vesicles (AUVs), tilamin mixed with zwitterionic unilamellar vesicles (ZUVs) and a non-AMP peptide mixed with AUVs. Only the spectrum belong to sample 2 (tilamin mixed with AUVs) shows a positive peak at 193 nm and negative ones at 208 and 222 nm which are indicative of the alpha helix structure [174]. The other three spectra are nearly overlapping and show no such signals indicating disordered peptides structures [174].

This confirms that tilamin adopts helical structure only when it interacts with the negatively charged lipid membrane. Linear dichroism spectroscopy (LD) was also used to investigate the orientation of tilamin helices with respect to the lipid membranes [75]

Four samples were studied, namely; tilamin with AUVs and ZUVs, and a non-AMP control peptide with AUVs and ZUVs. Figure 3.7.D shows the spectrum of each sample. The one that belong to tilamin in AUVs is clearly distinguished with positive peaks at 190-195 and 220-230 nm and a vague minimum at 205-210nm.

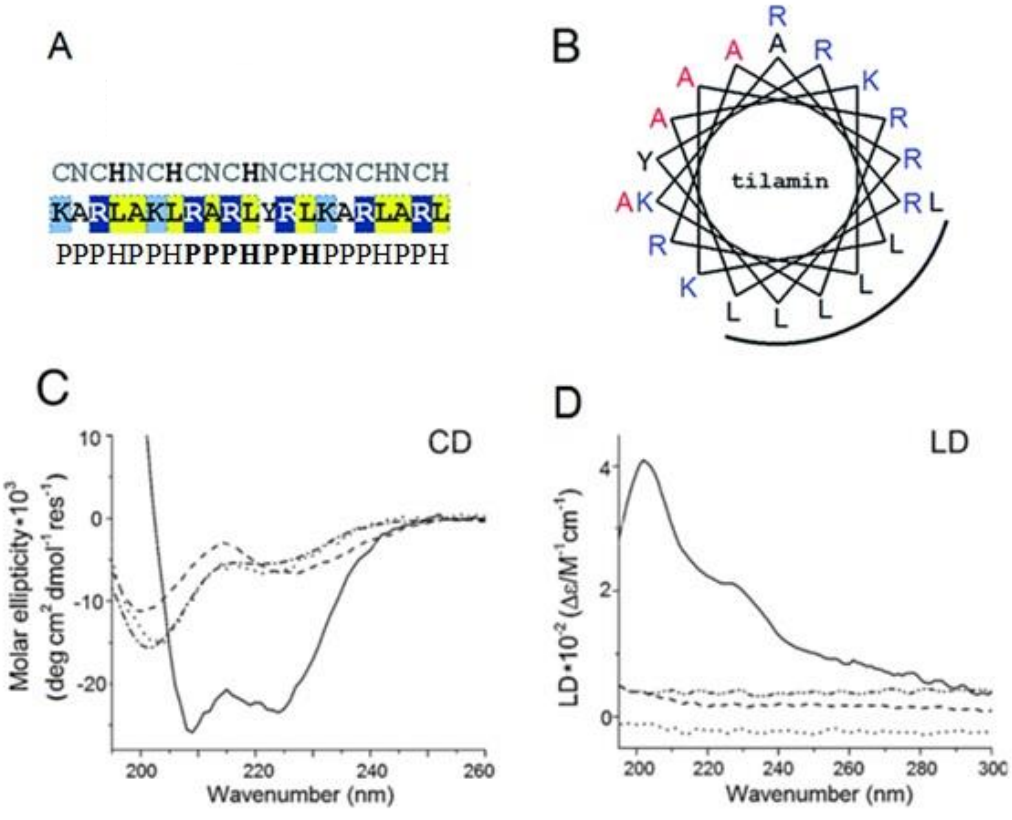

Figure 3.7: Tilamin peptide sequence and secondary structure characterisation. (A) Tilamin amino-acid linear sequence (Middle) highlighting the polar (P) and hydrophobic (H) amino acids residues (lower), and the cationic (C) and neutral (N) amino-acids residues (upper). (B) Tilamin peptide as a helical wheel showing an amphipathic helix (C) (CD) spectra for tilamin in the DLPC/DLPG (3:1) AUVs (solid line), DLPC (dotted line) and phosphate buffer (dash-dotted line) and for non-AMP in the DLPC/DLPG (3:1) AUVs (dashed line). Peptides were at 30 µM, at lipid/peptide 100 molar ratios. (D) (LD) spectra for tilamin in DLPC/DLPG) (3:1) AUVs (solid line) and DLPC (dotted line), and for non-AMP in DLPC/DLPG (3:1) AUVs (dashed line) and in DLPC (dash-dotted line). Peptides were at 30 µM, at lipid/peptide 100 molar ratios.

These peaks are indicative of oriented peptides [175]. Comparing with amhelin LD spectrum shown in figure 3.1.D, the peaks for tilamin with AUVs are broader. More importantly, the peaks here have positive values indicating that tilamin has a more parallel orientation to the membrane normal and the direction of the excitation light [169, 175].

3.3.2 Biological Activity of Tilamin

Tilamin shows an antimicrobial activity against different types of bacteria and with no considerable toxicity to human cells under the same conditions.

Table 3.2 compares the minimum inhibitory concentration (MIC) of tilamin with amhelin and three other well-known antimicrobials, namely; cecropin B, daptomycin and polymyxin. Seven types of gram-positive and gram-negative bacteria were examined in the assay as well as the human red blood cells.

The results show that tilamin is effective in the same concentration ranges when compared with the other antimicrobials against all the studied types of bacteria. Tilamin also shows less toxicity to human red cells comparing with the other antimicrobials.

Cell	**Peptide[a]**				
	tilamin	**amhelin**	**cecropin B**	**daptomycin**	**polymyxin B**
	Minimum inhibitory concentrations, μM				
P. aeruginosa (ATCC27853)	4.0	12.3	1.6	>100	<1
S. aureus (ATCC6538)	8.8	>50	>100	7.7	<50
E. coli (K12)	10.2	3.0	<1	>100	<1
B. subtilis (ATCC6633)	<1	6.2	>50	7.7	1.5
S. enterica (ATCC700720)	3.1	6.2	3.1	>50	<1
E. faecalis (OG1X)	3.1	6.2	25	>100	>100
M. luteus (ATCC 7468)	<1	7.1	<1	15.4	<1
	(LC_{50})[b], μM				
Human erythrocytes	10^4	12 x 10^3	8.3 x 10^3	10^3	N/D

Table 3.2: Minimum inhibitory concentration (MIC) assay indicating the biological activities of peptides used in the study. Red, blue and green denote gram-negative, gram-positive and gram-variable bacteria respectively. [a]non-AMP was inactive (>>250 μM). [b]median (50%) lethal concentration calculated from the actual percentage of lysed bacteria populations at 500 μM. N/D – non-detectable. All tests were done in triplicate.

Although the results of MIC assay indicate the amount of the antimicrobials needed to inhibit the bacterial growth overnight, it does not give kinetic information about how quick the response is against bacteria. To probe this, a live/dead-stain (propidium iodide, PI) assay [170] was performed on *E coli* as a good model for gram-negative bacteria. The fluorescence data shows that, at MIC, tilamin is three times quicker in killing bacteria comparing with cecropin B and amhelin, figure 3.8. The fluorescence data were compared to a non-antimicrobial peptide as a reference which shows no impact on bacteria.

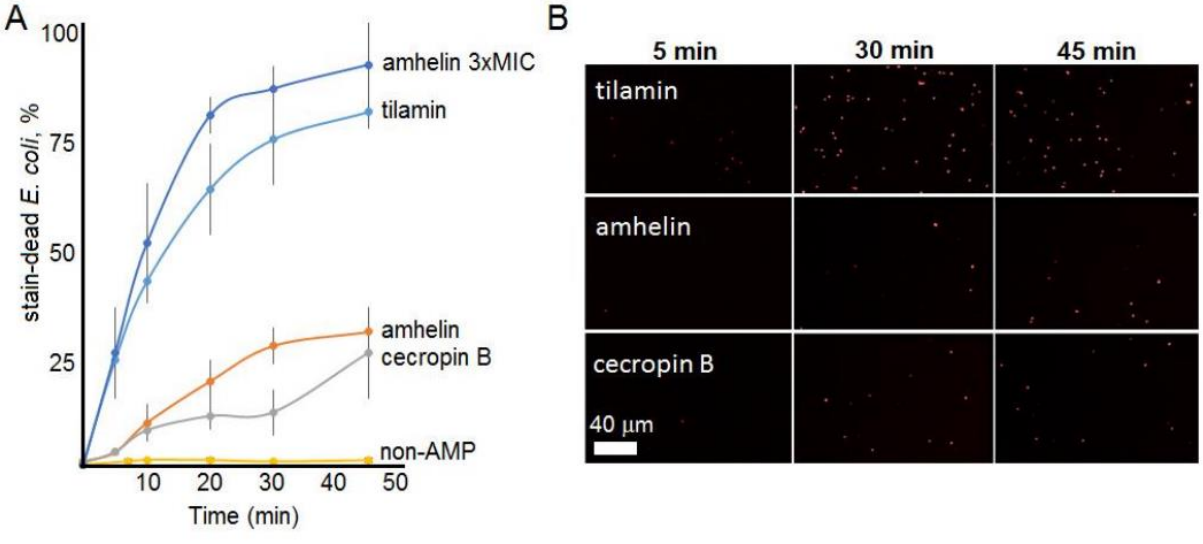

Figure 3.8: Comparison of antimicrobial kinetics of tilamin and other studied peptides. (A) Average numbers of stain-dead E. coli cells incubated with tilamin (blue), amhelin (orange), cecropin B (grey) at MICs, amhelin at 3xMIC (dark blue) and the non-AMP at 10 µM (yellow) as a function of time. The data represent mean values ± s. d. (B) Fluorescence microscopy images of PI-stained E. coli cells.

3.3.3 Tilamin Mechanism on Bacterial Membrane

AFM imaging was used to determine the mechanism by which tilamin attacks the bacterial membranes and to probe whether it differs from amhelin mechanism. For comparison, AFM experiments were performed under similar conditions of those applied for amhelin. Exactly the same supported lipid bilayers were prepared as bacterial model membrane using the lipid composition of DLPC:DLPG (3:1) mass ratio. A flat lipid bilayer was reconstituted and imaged before adding any tilamin as shown in figure 3.9.

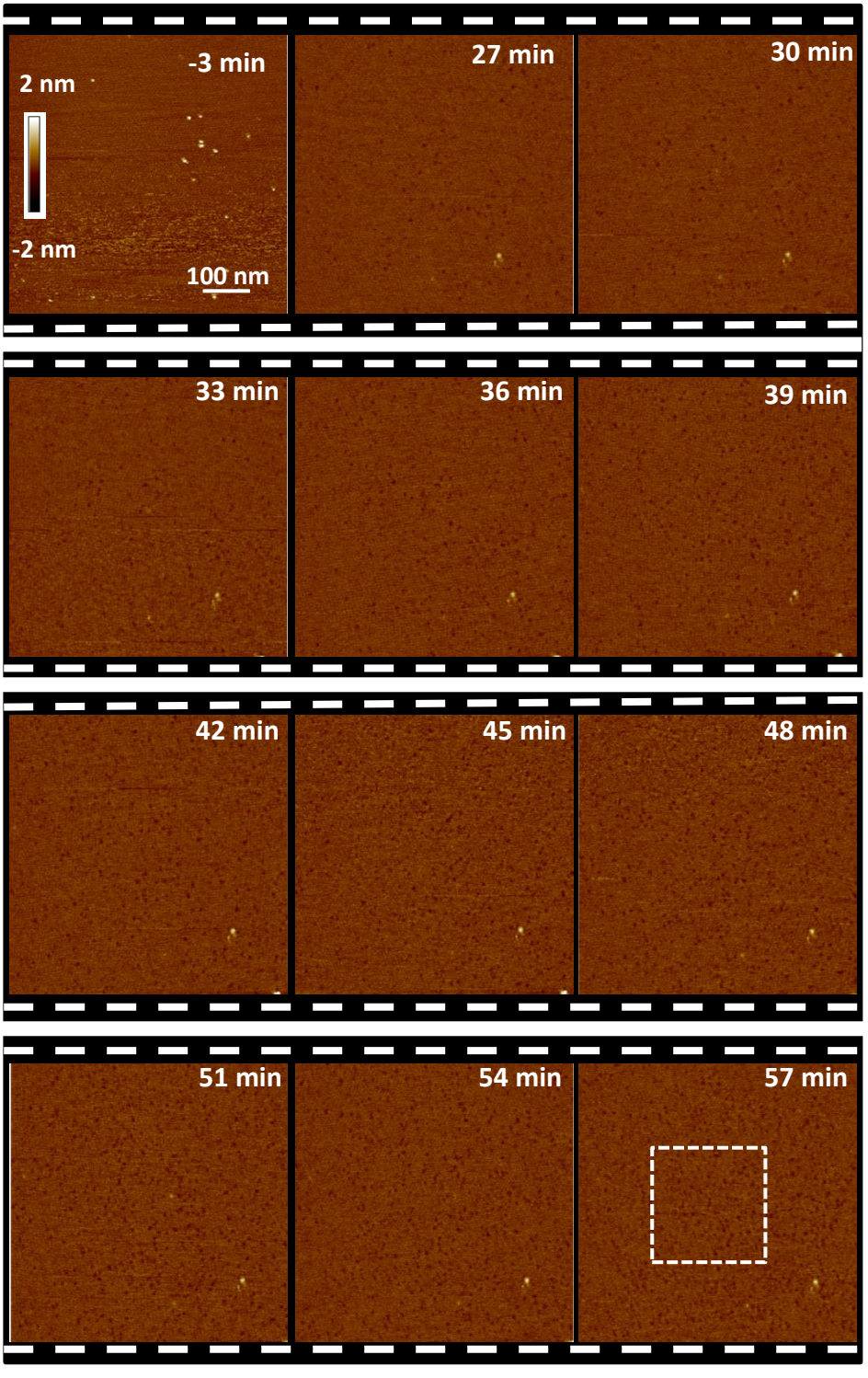

Figure 3.9: Time-lapse in-liquid AFM images of DLPC:DLPG (3:1 W:W) supported lipid bilayer incubated with 1.5µM tilamin. Tilamin was injected on the sample at time (0) minutes. The first image was taken before the treatment with tilamin and shows a flat bilayer. The sample was prepared in buffer of 20 mM HEPES and 150 mM NaCl, PH≈7.4 and AFM performed in room temperature

Tilamin peptide was then added at time 0 min to a total concentration of 1.5 µM in the sample. AFM time-lapse imaging was carried out over the same surface for an hour. The subsequent images after adding the peptide show that tilamin forms small pores which are distributed over the membrane surface. Unlike amhelin, the pores formed by tilamin did not develop in size over time. On the other hand, the number of pores has increased.

The diameter of each pore is constant at about ~15 nm. Zoomed-in images were taken shown in figure 3.10. Unlike amhelin, the height profile in figure 3.10 right shows that the pores formed by tilamin have depths of about ~1.5 nm.

In addition, pores could gather in clusters to form bigger compressed membrane areas with ~1 - 1.5 nm depth. Figure 3.11 shows a bacterial model membrane incubated with 1.8 µM tilamin. Figure 3.11.a shows a membrane image captured before injecting tilamin peptide which confirms the flatness of the membrane. Once peptides were added, they appeared to form clustered pores distributed all over the sample as shown in image 11b. The magnified area on image in figure 3.11.b highlighted by the dashed square is shown in figure 3.11.c. It shows that the lesions created by tilamin peptides take the form of depressed membranes patches with ~ 1.5 nm depth as illustrated in the corresponding height profile on figure 3.11.d.

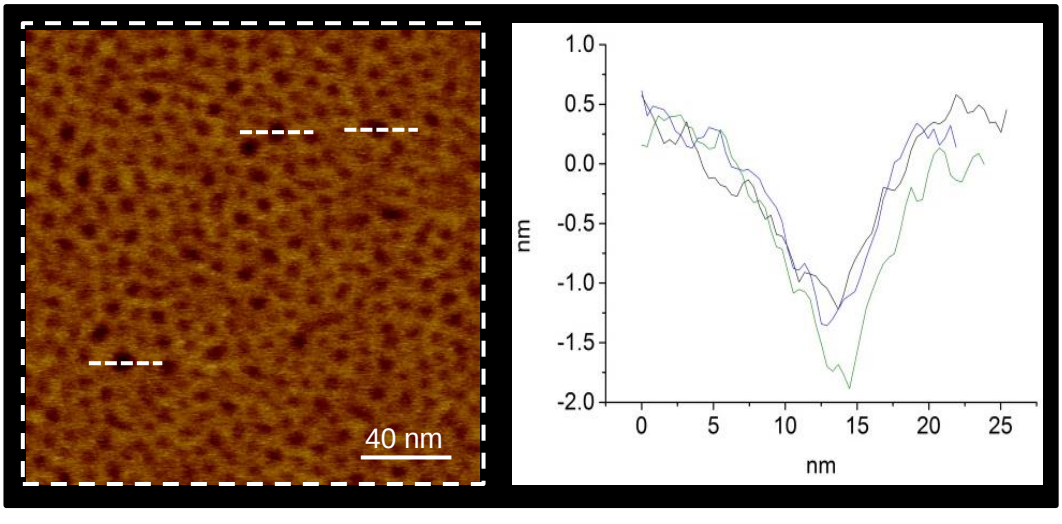

Figure 3.10: Pores characterisation formed by 1.5 µM tilamin on bacterial model membrane. (Left) Zoomed in-liquid AFM topography image taken from the area highlighted by the white dashed frame shown on the last image in figure 3.9. (Right) the corresponding height profiles of three selected pores highlighted by the white dashed lines on the image. The profiles show consistent pores depth of ~ 1.5 nm and diameter or ~ 15 nm.

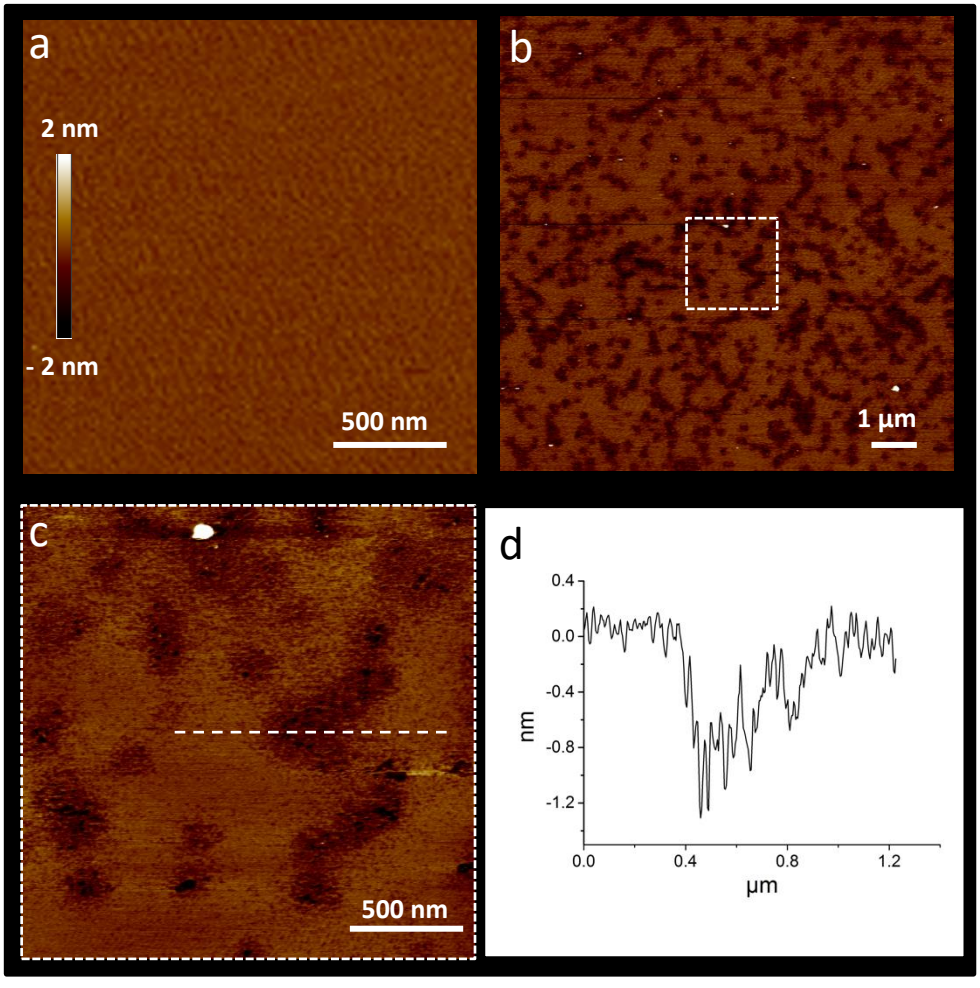

Figure 3.11: In-liquid AFM images of DLPC:DLPG (3:1) lipid bilayer incubated with 1.8 µm tilamin. (a) Image of a flat membrane before treating with tilamin peptide. (b) Image of the membrane treated with 1.8 µM tilamin showing clustered pores. (c) A magnified image of the area highlighted by the dashed square on b. (d) The corresponding cross section profile (dashed line on c) showing compered membrane with ~1.5 nm depth. The sample was prepared in buffer of 20 mM HEPES and 150 mM NaCl, pH≈7.4 and performed under room temperature

The amphipathic assembly and the positive overall charge of tilamin as key antimicrobial features are similar to those discussed for amhelin. Changing six of the positively charged amino acid, lysine to arginine, however, has influenced the mechanism and results in shallower and non-expanding pores

To understand how helices spanning 3nm (tilamin) drill and stabilise holes of only 1.5 nm depth in the membrane, we proposed a mechanism shown in the schematic representation in figure 3.12.

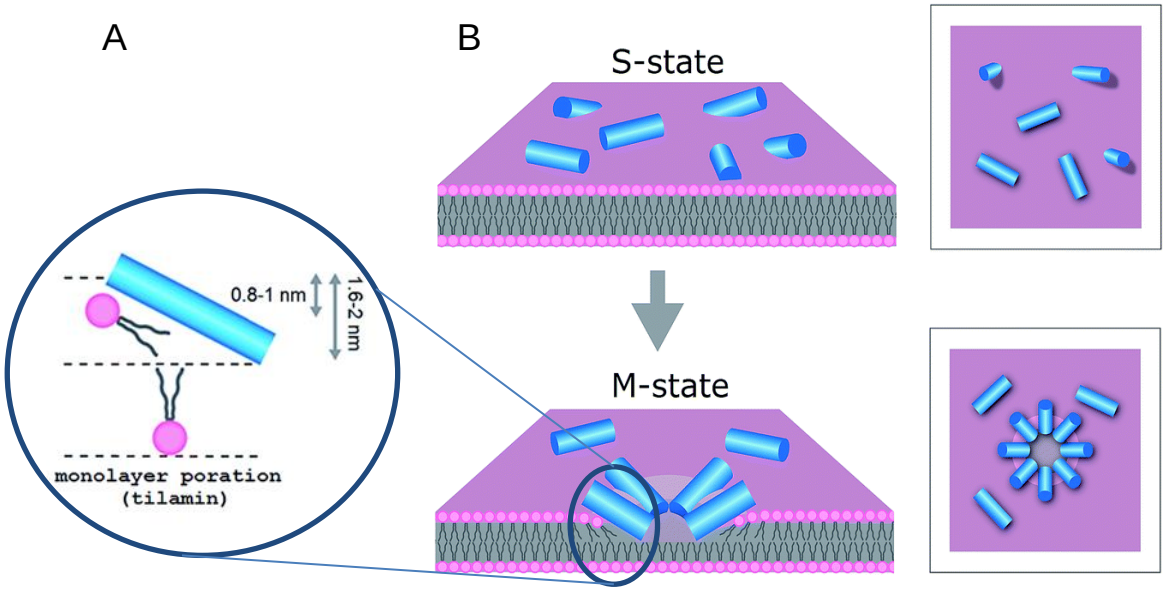

Fig 3.12: Proposed interactions and insertion mechanism of tilamin in the bacterial membrane. (A) Schematics of pore edges showing depths of insertion for proposed monolayer and transmembrane poration mechanisms. For clarity, only one peptide (blue cylinder) and one phospholipid per layer are shown (aliphatic chains in grey, headgroups in pink). (B) Proposed mechanism for antimicrobial monolayer poration. Peptides (blue cylinders) bind to the membrane surface – “S”-state (upper), and insert with forming pores in the outer leaflet of the bilayer – “M” state (lower).

It shows that tilamin peptides orient with a tilted state to stabilise with a monolayer removal of the lipid membrane, compared with the 3 nm deep, bilayer removal for those formed by amhelin.

Tilamin peptides here undergo two stages when interacting with the bacterial membrane. The first stage which we call S-state is initiated by the electrostatic interactions between positively charged amino-acid residues (arginines and lysines) and the negatively charged membrane. This leads tilamin to fold into amphipathic helical structure similar to amhelin.

The hydrophobic amino-acid residues (Leucines) are then exposed to water which is not energetically stable. Hence, tilamin will seek stabilisation by drilling into the membrane to hide the leucine residues within the lipid membrane and to interact with the hydrophobic lipid tails.

Arginine however allows extensive H-bonding with its five hydrogen bonds donors to stabilise Arginin–lipid headgroups clusters unlike lysine which allows only one hydrogen bond [176], figure 3.13. These bonds contribute in holding tilamin back from diffusing freely over the lipid surface. In addition, arginine has a pKa of 12.48 comparing with 10.79 for

lysine, figure 3.13. This makes arginine a stronger base with a more stable translocated positive charge on the two amine groups under the same condition [176, 177]. This supports stronger electrostatic interactions between tilamin peptides and lipid headgroups, compared with amhelin.

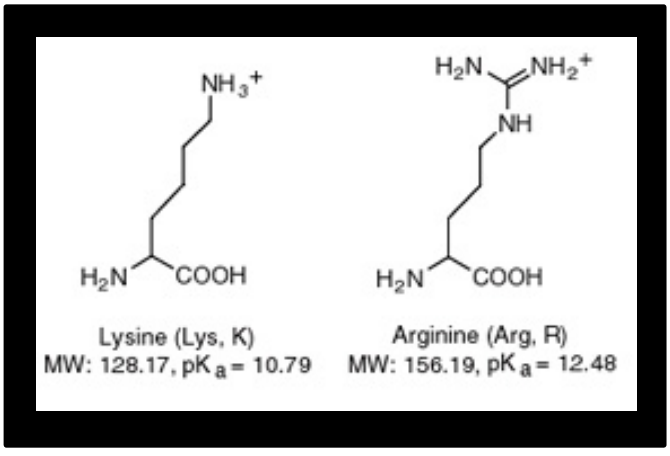

Figure 3.13: The chemical structure of Lysine and Arginine amino acids with the pKa values.

While the hydrophobic interactions promote a deeper penetration, the electrostatic interactions arrest the peptide in the lipid headgroup region [178]. These conflicting forces are compensated in a tilted peptide orientation spanning only halfway through the membrane removing only the upper leaflet of the lipid bilayer. Such an orientation hides leucine residues from the hydrophilic medium and allows electrostatic interactions to lock the peptide from diffusion.

For such shallow pores to form, however, one would expect that the hydrophobic tails of the lower membrane leaflet are exposed to the aqueous medium, which is again not a favourable, stable state. This may be true for a real bacterial membrane [22], however, in the model membrane conditions, this state could stabilise as the lipids of the lower leaflet are bound to the substrate via relatively strong electrostatic interactions.

3.4 Conclusion

In conclusion, we have demonstrated that the two peptides amhelin and tilamin show effective antimicrobial properties and negligible cytotoxicity. The experimental data indicated that both peptides fold into helical amphipathic structure of 3 nm length.

Atomic force microscopy has revealed a difference in the mechanism by which the two peptides attack and disrupt the bacterial model membrane. Amhelin, which has lysines as the positive charged amino acid, attacks the bacterial membrane and orients along the membrane thickness forming expanding pores until the membrane removal. Tilamin on the other hand has six arginine residues. Upon membrane attack, it assumes a tilted configuration with respect to the membrane surface, to form shallower static pores, removing only parts of the upper leaflet of the membrane bilayer.

Chapter 4

Antimicrobial Capsules for Gene Delivery

4.1 Introduction

Gene therapy is a promising solution against many genetic diseases. In principle, genetic disorders can be cured by replacing or disrupting defective genes using synthetic nucleic acids or analogues [179]. In practice, a main challenge remains in finding delivery vectors that can safely deliver therapeutic nucleic acids to the targeted human cells [180]. Viruses can be developed as transfection vectors and are the most efficient for gene delivery but there are safety concerns associated with their use including immune reactions and insertional mutagenesis [181]. Synthetic non-viral vectors, on the other hand, still greatly lack the required structural integrity. The ideal delivery vector therefore is considered as a compromise between viral and synthetic vehicles. This would be a nanoscale device which structurally mimics native viruses to efficiently deliver genes, but is directed to do so at the designer's whim.

In addition to the challenge of designing effective and safe delivery vectors, gene delivery can be compromised by bacterial infections. This prompts the need for vehicles that are able to not only deliver nucleic acids to human cells but also kill pathogens [182]. With the rise of antimicrobial resistance, supramolecular chemistry may provide creative solutions to the challenge by designing synthetic systems with a dual functionality, i.e., gene delivery and antimicrobial activity.

In this chapter, the design of a synthetic antimicrobial capsule (termed capzip) is discussed, as developed by our collaborators at NPL. The results show that the capsules successfully and safely deliver siRNA to human cells in addition to being toxic to bacterial cells. As part of this PhD research, the antimicrobial attack on the bacterial membranes was monitored by atomic force microscopy in real time to elucidate the mechanism of action.

4.1.1 Antimicrobial Virus Design

The building block of the devised capsule was inspired by a breast-milk protein lactoferrin shown in figure 4.1 [183]. The antimicrobial motif within the protein consists of 6 amino acids (RRWQWR) which folds into an amphipathic β-strand which tends to interact with another strand (blue and green) via hydrogen bonds, figure 4.2.a [184]. This motif, if isolated from the rest of the protein, exhibits negligible antibacterial properties, but does not co-assemble into capsules [2].

Capsules in nature like in virus capsids employ noncovalent interactions between subunits to direct the assembly into icosahedral cage architectures [185].

With such inspiration in mind, we modified the amino acid sequence of this natural building block to allow particular supramolecular interactions between the engineered subunits to co-assemble into capsules.

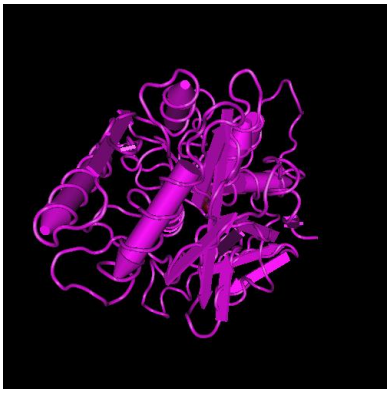

Figure 4.1: Structure of the recombinant N-terminal lobe of human lactoferrin determined by X-ray crystallography at 2.0 Å resolution [19]

First, we have substituted the amino acid glutamine (Q) by threonine (T). This change is to copy the well-known tryptophan zipper sequence with a characteristic core motif WTW. This motif adopts β-sheet conformations

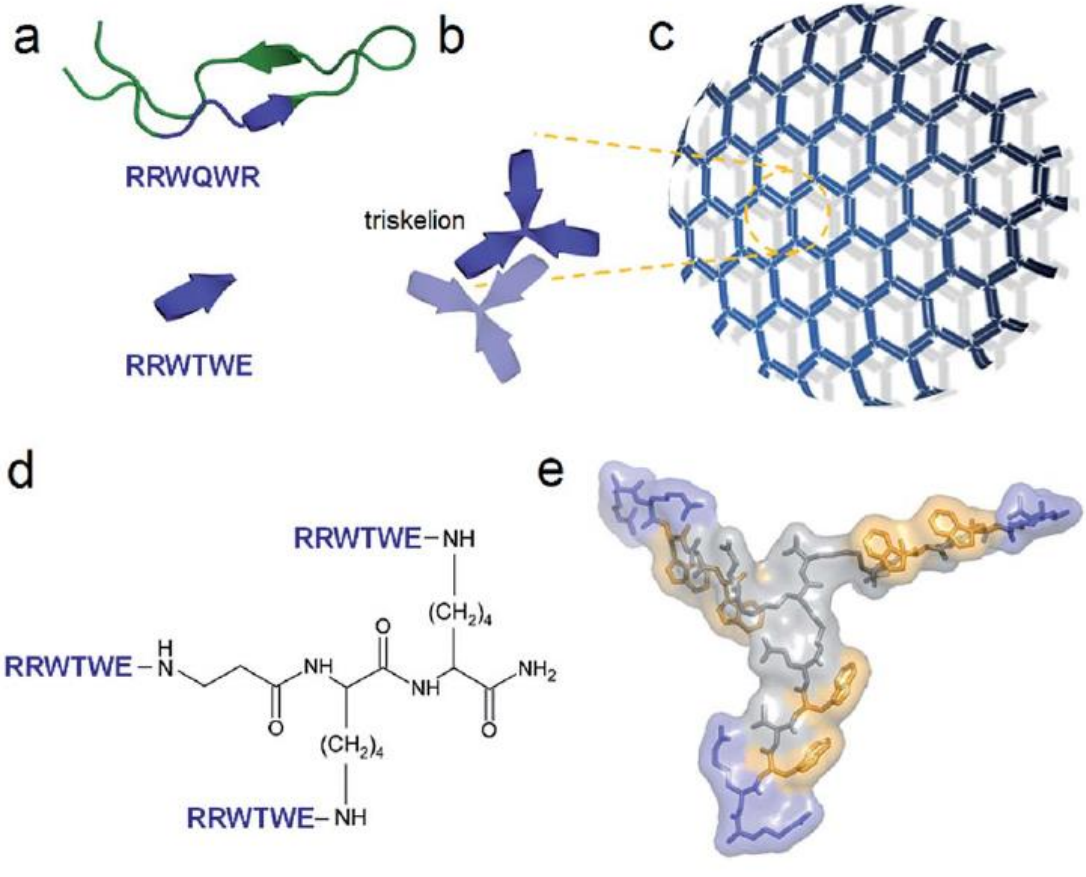

Figure 4.2: Capzip design. (a) Antimicrobial lactoferrin peptide (PDB entry 1LFC rendered by PyMol [20]) with the RRWQWR motif highlighted in blue (top). The motif is converted to a self-complementary RRWTWE β-strand (bottom). (b) Three copies of RRWTWE are conjugated into a β-strand triskelion. For clarity only two triskelions forming a β-sheet are shown and highlighted in different colours. (c) Triskelions self-assemble via a β-sheet-formation following a trilateral honeycomb-like symmetry. (d) The chemical structure of the triskelion. (e) A β-strand triskelion model with arginine and tryptophan residues highlighted by blue and yellow, respectively. The figure was reproduced from reference [2].

with cross-strand tryptophan rings packed tightly against one another [186], figure 4.2.a. Secondly, we have substituted the positively charged amino acid arginine (R) at the C-terminal by the negatively charged amino acid glutamic acid (E). This change will increase the self-complementary of the β-strands and direct to arrange antiparallel. The self-complementarity is enhanced from the positive-negative electrostatic interactions arising between the amino-acid side chains of opposite termini (R and E), figure 4.2.a. Finally, we can learn from natural virus architecture, which adopts an n-fold rotational symmetry, where n is usually 3 or 5 or both [180].Thus, to induce the three dimensional symmetrical self-assembly, we have linked three of the resulted β-sheet motifs into triskelion figure 4.2.d, [185]. The resulted triskel conjugate of RRWTWE is reminiscent of native cage-like subunits figure 4.2.b–e. In the triskel conjugate, RRWTWE is prone to fold as a β-turn and pair into a β-sheet with another arm of another conjugate [184]. Triskelions are then expected to propagate into two-dimensional sheets whose increasing curvature would facilitate the formation of a three dimensional capsule.

4.1.2 Capzip Characterisation

The capzip assembly conditions were kept constant for reproducibility. As explained in detail in chapter 2, the monomers (capsule subunits) were dissolved to a concentration of 100 μM in a buffer solution of pH 7. The sample was then incubated over night at room temperature to allow time for complete assembly. Various experiments showed that capzip readily assembles into morphologically uniform and polydisperse hollow capsules with dominating size ranges of 20–200 nm. The assembled structures were confirmed by atomic force microscopy (AFM), transmission electron microscopy (TEM) and cryo-scanning electron microscopy (SEM) [2]. Figure 4.3.a shows an in-liquid AFM image with capzips in different sizes, with diameters typically in the range of 20-100 nm. The cross section profiles in figure 4.3.b show sizes of the three selected capzips highlighted by the white dashed lines. The three measured capzips have almost overlapped cross section profiles with about 60 nm width (diameter) and 30 nm height. Figure 4.3.c shows AFM images of dried samples. Circular dichroism (CD) microscopy has confirmed the β-sheet secondary structure of the peptides making up the capsules with and without an siRNA cargo. Figure 4.3.d is CD spectra of capzip with siRNA (dashed line) and without siRNA (solid line). The CD spectra show minima at $\lambda = 200$ and $\lambda = 214$ nm, which are characteristic to β-turns confirming β-sheet secondary structure of the subunits within the assembled capsules.

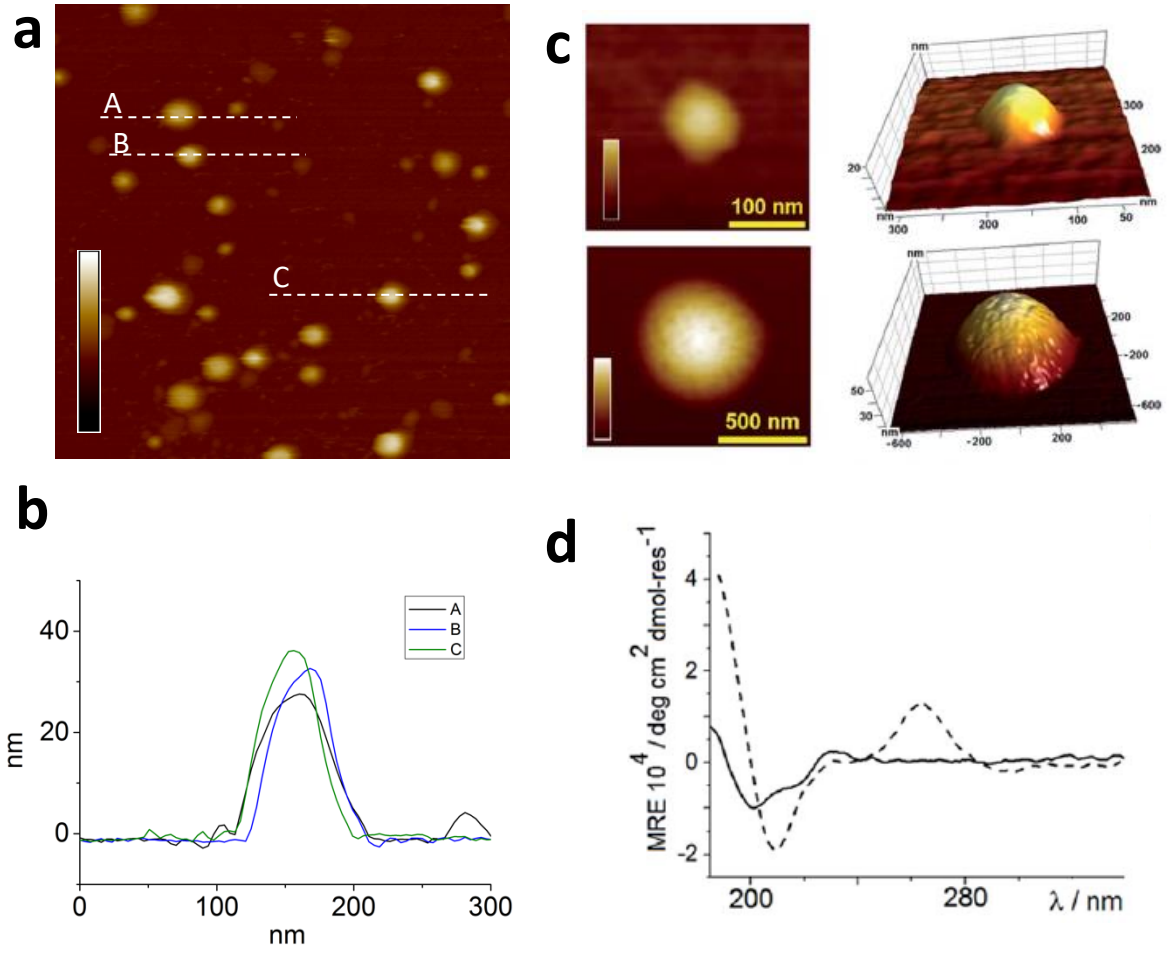

Figure 4.3: Capzip characterisation. (a) In liquid (buffer) AFM topography images of capsules on mica. (b) The cross section profiles for the three selected capsules by the dashed white lines A, B and C in a. The colour scale is 80nm. (c) In-air AFM topography images of capsules (dry samples) on silicon wafer with their 3D representations. Colour scales are 20 nm (upper) and 60 nm (lower). (d) CD spectra for capzip (solid line) and capzip with siRNA (30 mM, dashed line)

4.1.3 Gene Delivery and Antimicrobial Property

To assess the dual functions that are aimed for with this design, capzips were tested for their ability to deliver gene to human cells and the antimicrobial responses on bacterial cells.

For gene delivery, capzip successfully co-assembled with model siRNAs (21 base-pairing duplexes) to form structures similar to those assembled in the absence of the cargo materials. CD and SAXS data confirmed a successful encapsulation of the cargo [2]. The two techniques along with AFM and TEM, all confirmed a consistent structure of capzip with and without cargo [2]. The successful gene delivery to human cells and silencing gene expression were investigated by florescence microscopy.

a

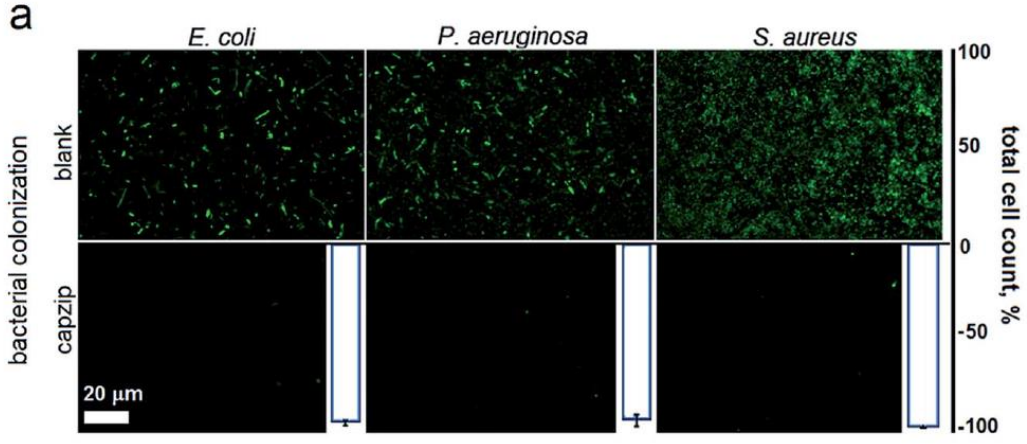

b

Biological cell	MIC, µM		
	capzip	ampicillin	gramicidin S
E. coli (K12)	20	9	22
P. aeruginosa (ATCC27853)	18	>200	43
S. aureus (ATCC6538)	30	5	22
	LC_{50}		
Bovine erythrocytes	>>100	UD*	≥25

*undetectable (>>10^3)

Figure 4.4: Capzip antimicrobial activity. (a) Confocal micrographs of bacterial cells after 16 hour incubations with and without capzip, stained with membrane-permeant SYTO®9. White histogram bars denote total cell counts (%) for bacterial colonization with capzip after subtracting background adhesion taken as 100%. (b) Biological activity of capzip in comparison with two other known antimicrobial agents. The panels were reproduced from Ref. [2].

The data shows that capzip delivered fluorescent siRNA to HeLa cells within the first hour of incubation [2]. The effect of this transferred gene into HeLa cells was measured by monitoring the knockdown of two genes meant to be expressed within the cells. The experiments compared knockdown levels of HeLa cells treated in three different ways. Firstly, with siRNA alone (without delivery vehicle) as a negative control, secondly; using N-TER® and Lipofectamine® which are commercially available vectors as positive controls for successful siRNA delivery, and finally using capzip. All samples were treated using the same siRNA materials under same conditions. The data were normalised to the first sample (negative control) and show that capzips successfully silence mRNA expression in the same range of efficiency as for the commercial vector N-TER®. Lipofectamine® however showed about 25% more positive result but that was on the expense of substantially reduced cell numbers indicating apparent cytotoxicity [2].

The antimicrobial property of the capzip was also tested against a range of planktonic cells types using fluorescence microscopy and via the minimum inhibitory concentration assay. Figure 4.4.a shows dead-stain assays [170] applied on three types of bacterial cells, namely; *E. coli*, *P. aeruginosa* and *S. aureus*. The total cell-count was measured using confocal laser scanning microscope differentiating between live cells which stain green and dead ones which stain red [2]. Capzip shows a 100% efficiency in killing the three tested types of bacteria within 16 hours. Figure 4.4.b shows a table comparing the minimum inhibitory concentrations [171] of capzip with ampicillin and gramicidin as two well-known antimicrobials. The numbers in the table indicate that capzip has values of MIC in same range of those for the other agents. The table also shows that capzip, similar to the other antimicrobial, does not show toxicity towards Bovine erythrocytes, as verified with a haemolysis assay (LC50) [2].

4.2 Mechanism of Antimicrobial Attack

Atomic force microscopy was utilised to image capzip in liquid while attacking the bacterial model membranes, showing large membrane disruption. Similar to what was described in chapter 3, a supported lipid bilayer was chosen to mimic the negatively charged bacterial membrane, facilitating high resolution imaging. The lipid used is a mixture of DLPC:DLPG with a mass ratio of (3:1), and the bilayer again was prepared by the same protocol explained in chapter 2.

As usual with these experiments, supported lipid bilayer were used as model membranes, and their integrity and flatness were verified before exposing them to capzip as shown in figure 4.5.a. The flatness of the surface is confirmed by the cross section profile (right) corresponding to the white dashed line in the AFM image. High capzip concentrations (5 µM) led to a major disruption of the membrane, as illustrated in figure 4.5.b, which shows an AFM image of the same area as in figure 4.5.a but after incubation with 5 µM capzip. The depth and heights of some features are shown by the cross section profile figure 4.5.b right. The profile shows pores with ~3nm depths, which is consistent with the expected lipid bilayer thickness. The aggregations however could be lipid vesicles formed from the peeled-off lipids or lipid-peptides aggregations.

After several experiments to optimize measurement protocols, the optimum concentration of capzip was found to be ~2 µM (at room temperature). This concentration appeared enough for capzip to diffuse across the sample while disrupting the membrane at a time scale that was accessible for AFM experiments.

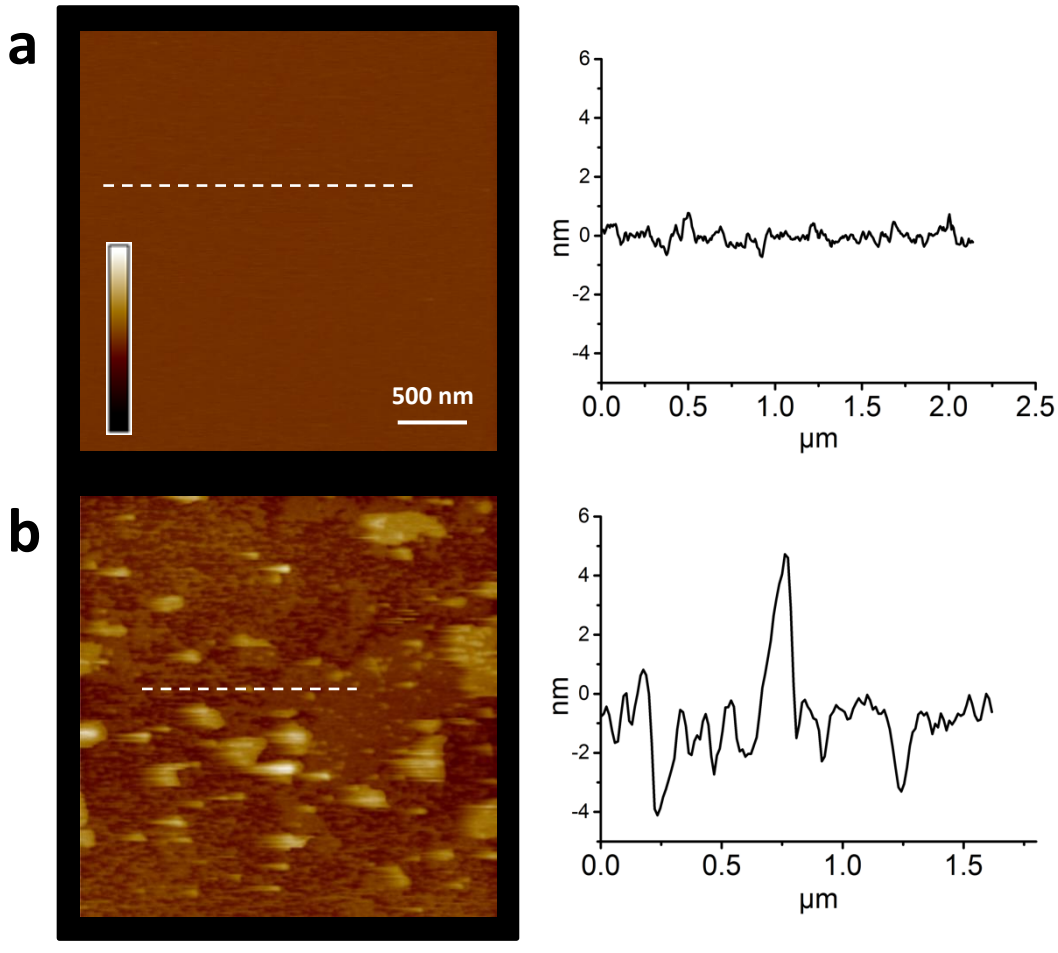

Figure 4.5: AFM images in liquid showing the effect of high capzip concentration on bacterial reconstituted membranes. (a) Image of the membrane before adding capzip (left). The flatness of the membrane surface confirmed with the cross section profile (right) of the area highlighted by the white dashed line. (b) Image of the same area after adding 5 µM of capsules (left). destruction of the membrane is confirmed by the height profile (right) of the area highlighted by the white dashed line. Colour scale is 40 nm. Experiment was done under the room temperature.

Figure 4.6 is a time-lapse sequence of AFM images over 17 minutes showing capzips attacking the bacterial membrane. The first image shows a flat and clean membrane surface acquired two minutes prior to capzip injection. Capzip dosage was injected at time 0 min at a concentration of ~ 2 µM.

The second image was acquired 5 minutes after capzip injection, showing membrane pores as well as capsules that are still intact (yellow particles), highlighted by white boxes and arrows. Capzip interacted with the bacterial membrane and over time some of them have descended in the membrane making pores at their precise landing positions. The pores sizes stay constant during the operation time of the experiment (120 minute).

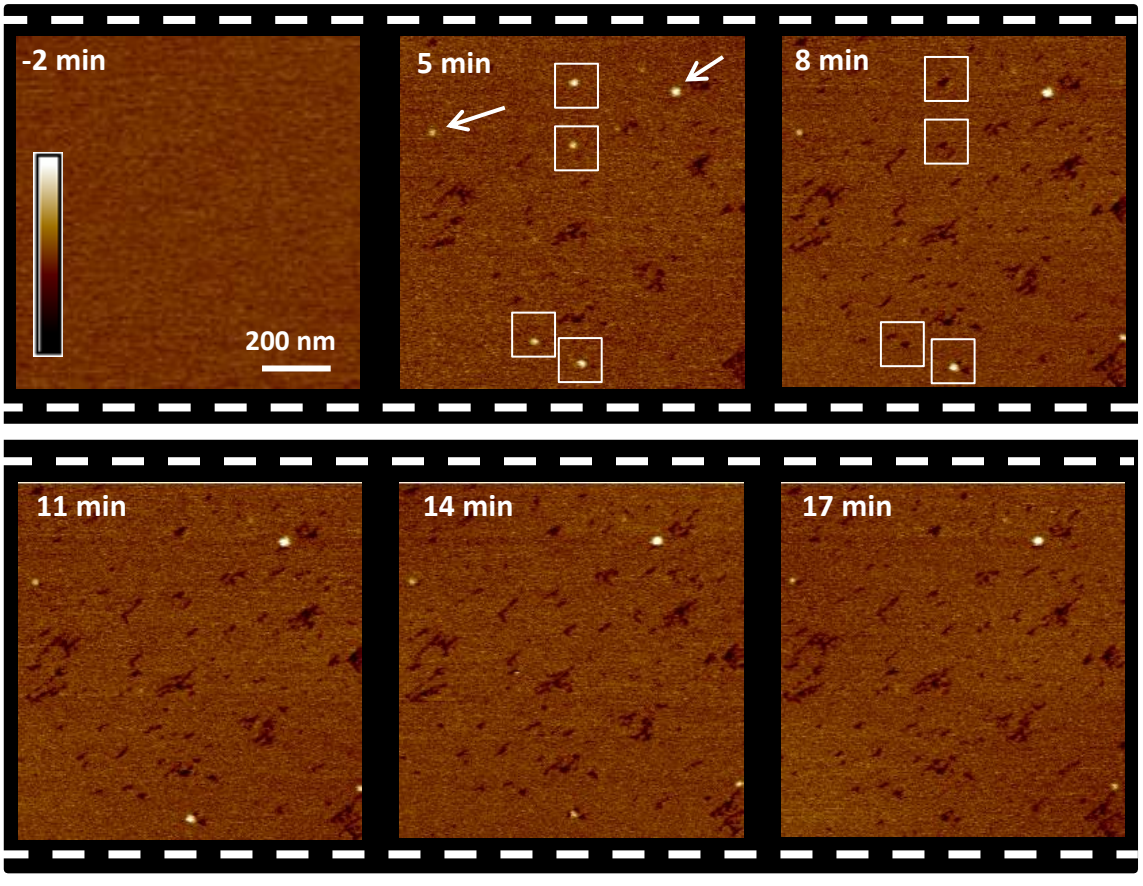

Figure 4.6: AFM time lapse images of a bacterial model membrane incubated with capzip at room temperature. The time stamp refers to the moment of capzip injection on the sample happened at time (0) minutes. White boxes and arrows are to highlight capzips. The total concentration of capzip in the sample is ~ 2µM. Colour scale is 6 nm. The full movie is available online with the supportive information of the published paper [2].

We next analysed the sizes of capsules and membrane pores in the second image of figure 4.6 (5 minutes after injection). Figure 4.7.a shows the image highlighting the features (turquoise colour) that have heights of at least 0.3 nm with respect to the membrane surface. The table in figure 4.7.a right shows six features in total (capsules) that have diameters of 30 ± 3 nm. The pores appearing in the same image were caused by capsules that had interacted with the lipid membrane and disassembled in less than 5 minutes.

Figure 4.7.b shows the depth analysis of the highlighted pores, which have depth of at least 0.2 nm below the membrane surface. The table in figure 4.7.b right shows that there are 37 pores counted with a mean depth of 1.2 ± 0.6 nm below the membrane surface. Given the small pore size at the scale of this images, the thus observed pore depth values may well depend on AFM tip size and the precise surface tracking in the AFM experiment.

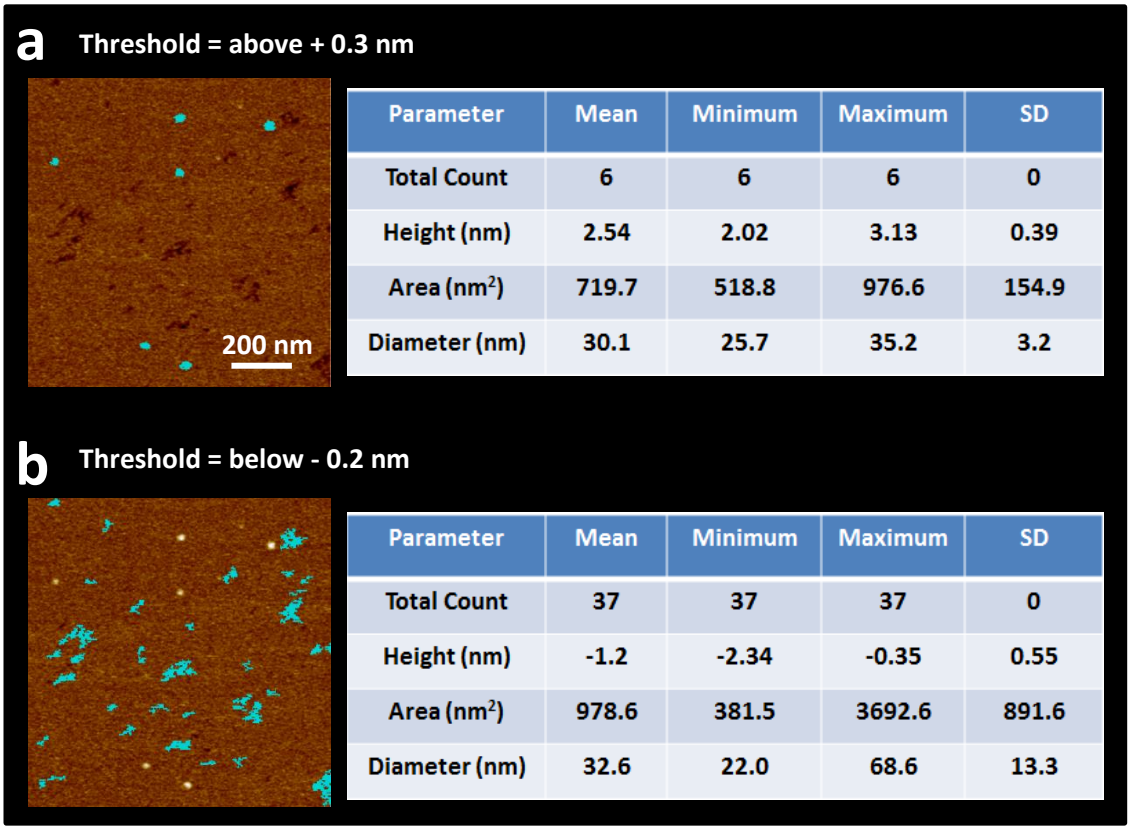

Parameter	Mean	Minimum	Maximum	SD
Total Count	6	6	6	0
Height (nm)	2.54	2.02	3.13	0.39
Area (nm^2)	719.7	518.8	976.6	154.9
Diameter (nm)	30.1	25.7	35.2	3.2

Parameter	Mean	Minimum	Maximum	SD
Total Count	37	37	37	0
Height (nm)	-1.2	-2.34	-0.35	0.55
Area (nm^2)	978.6	381.5	3692.6	891.6
Diameter (nm)	32.6	22.0	68.6	13.3

Figure 4.7: Size analysis of capsules and pores. (a) AFM image of a bacterial model membrane incubated with 2 uM capzip for 5 minutes. A mask is set to define features that are at least +0.3 nm above the membrane surface. Features/capsules with height above 0.3 nm are thus highlighted in blue. The table on the right shows size estimates for the highlighted features (capzips on the membrane). (b) The same AFM image but with the mask set to define features that are at least 0.2 nm below the membrane surface, to highlight membrane poration. Table on the right shows sizes of the highlighted features (pores).

To analyse the conversion of an individual capzip into a pore, figure 4.8 shows a sequence of magnified AFM images with a capsule that took 14-17 minutes to convert into a membrane pore at it precise landing position. From the cross section profiles (dashed white lines) on the images, the capsule initially appears with a height of 2 - 2.5 nm. The measured height then decreased over time until the capsule completely disappeared and transformed into a pore of ~ 2 nm depth.

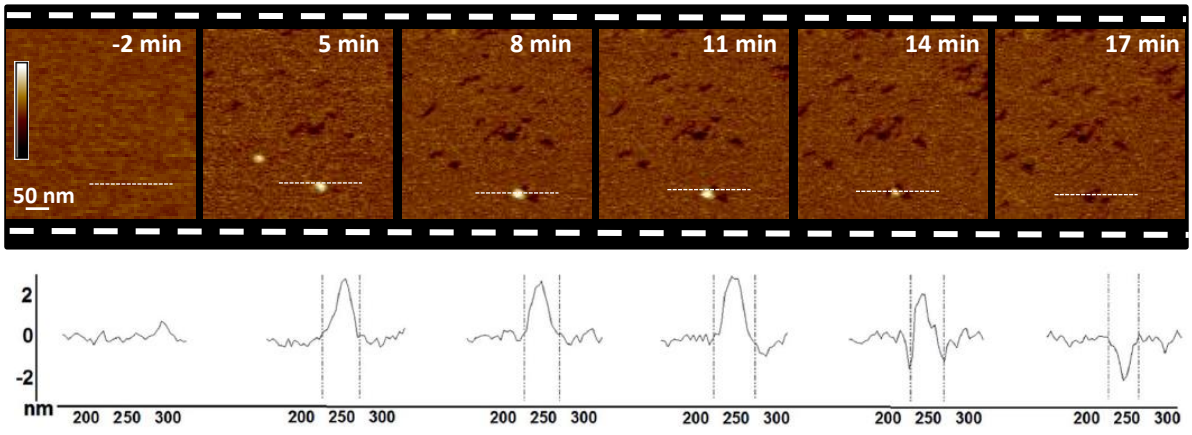

Figure 4.8: Time-lapse sequence of AFM images at higher magnification, showing a landing capzip on the bacterial model membrane. The time stamp refers to the moment of capzip injection into the sample at 0 min. The colour scale is 6 nm. Dashed lines highlight the lines for which height profiles are shown in the lower panel. The total concentration of the capzip in the sample is 2 µM. The experiment was done at room temperature.

4.3 Discussion

As explained above in the design section, capzip subunits are devised to interact with each other to complete the formation of hollow capsules. The stability of capzip structure is attributed to the inter-molecular interactions between the subunits' arms. These interactions were probed (by our collaborators) and confirmed by circular dichroism microscopy, FTIR and small angle X-ray scattering (SAXS) [2]. However, the pH of the solution is essential to maintain these interactions. For example, arginine (R) and glutamic acid (E) are positive and negative amino acids, respectively, and the electrostatic interactions between them are part of the capzip stability mechanism as explained in the design section of this chapter. The pKa and pI values for these two amino acids are, respectively, 13.2 and 10.76 for arginine, and 4.25 and 3.08 for glutamic acid. In a solution with pH 7 (i.e., neutral and physiological), arginine will be protonated and have an overall positive charge, while glutamic acid will be deprotonated and have a negative overall charge. Although this has yet to be experimentally verified by AFM or laser scattering techniques, having a medium with more acidic or more basic pH will affect the balance of the opposite interacting charges which might destabilise the capsule structure.

The AFM data shows that capzip binds to and next collapses on/into the negatively charged bacterial model membranes. This is triggered by the electrostatic interactions initiated after the first contact between the positively charged arginine within the capzip subunits and the negatively charged lipid headgroups.

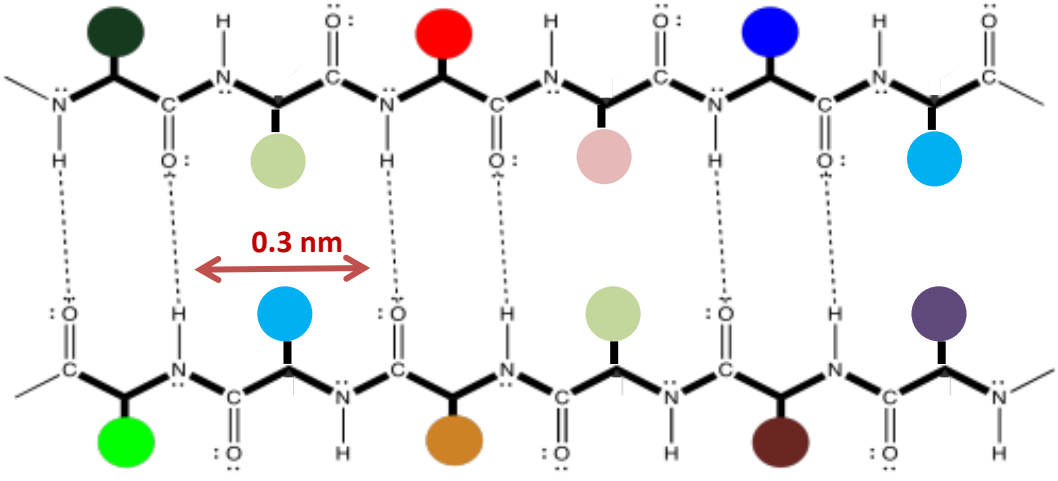

Figure 4.9: Schematic representation of two β-strands arranged antiparallel with hydrogen bonds between the backbones. Coloured circles denote amino acid side chains. Each amino acid spans ~ 0.3 nm along the contour of the peptide.

These interactions cause disruption in the membrane and the capzip structure. After some time, capzip will disintegrate into either completely discrete and separate subunits or they may keep a form of association between their arms. Our data do not allow us to distinguish between these two scenarios. That said, as explained above, the subunits arms are β-strands, which tend to arrange antiparallel with the hydrogen bonds, bridging the backbones together as shown in the schematic in figure 4.9.

In addition to hydrogen bonding, the two strands are further stabilised by interactions between side chains of some amino acids, in particular tryptophan- tryptophan (W-W) and arginine-glutamic acid (R-E) interactions. This suggests that capzip collapse could happen while keeping subunits arms arranged together with some reorientation due to the transition from a hollow sphere into an energetically stable pore-forming state within the membrane. AFM data confirms that the pores have a depth of ~ 2 nm. This matches the length of the subunit arm formed by 6 amino acids as each residue within a β-sheet secondary structure spans ~ 0.3 nm [187], figures 4.9 & 4.10.a. It also matches the thickness of one leaflet of the lipid membrane, figure 4.10.b. A hypothetical stable pore-state for capzip subunits within the bacterial membrane, consistent with our experimental data, is illustrated in figure 4.10.c & d. The suggested pore depth of ~ 2 nm is determined by the triskelions arms spanning only halfway through the membrane. Each arm is associated with another arm from another triskelion. The two associated arms have a hydrophobic side formed by the hydrophobic side chains and a hydrophilic side formed by the hydrophilic side chains. The hydrophobic side faces and interacts with the hydrophobic tails of the lipids and the hydrophilic side is pointing toward the core of the pore to interact with the aqueous medium.

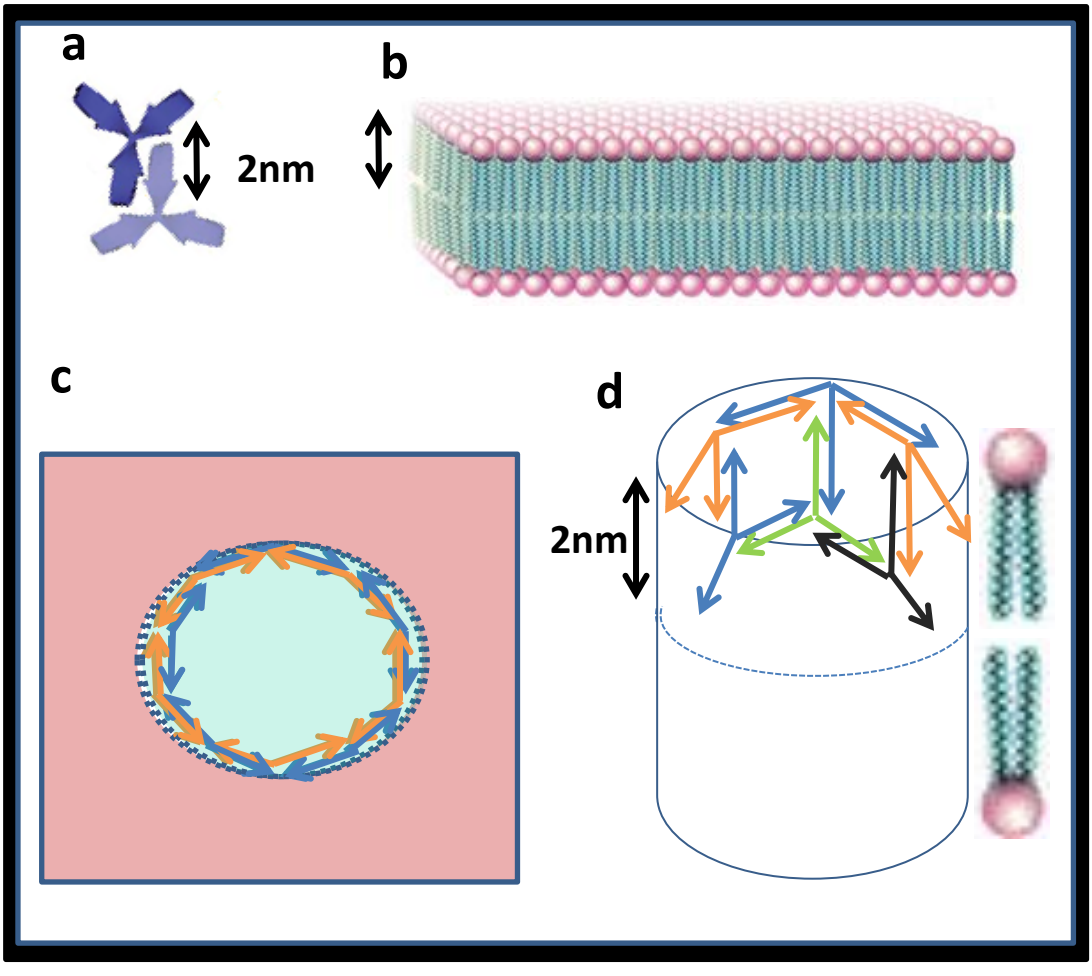

Figure 4.10: Schematic representation of the proposed stable (meta-)pore-state for capzip subunits within the bacterial membrane. (a) Two associated triskelions interacting via their arms which span 2nm. (b) Cartoon of a lipid bilayer, highlighting the depth of one leaflet. (c) Schematic of a top-down view for the pore formed by capzip subunits, highlighting the horizontal arms around the pore edges. (d) Schematic showing triskelions forming the walls of the pores within the membrane.

The bottom of this pore consists of the hydrophobic tails of the lower leaflet of the lipid bilayer. This can only be stable as the head groups are bound to mica substrate, which is not the case in the real, free-standing bacteria membrane. In general, it is not energetically stable for the hydrophobic tails of the lower leaflets to remain exposed to the aqueous medium. This non-stable state could then induce a quick lipid rearrangements leading to membrane disruption and cell lysis.

4.4 Conclusion

In summary, this chapter describes a conceptual design for virus-like capsules with dual biological activity. Similar to viruses, the capsules self-assemble from individual subunits

and promote gene delivery. AFM has confirmed a consistency in the capsule structure with a variety in size. This plasticity is an advantageous for ensuring that capsules are not limited to hosting only specific sizes of cargo like viruses. Along with other techniques, AFM has also confirmed the antimicrobial function of the capsules. The images show capsules attacking bacterial model membranes to form pores on their precise landing positions. A possible attacking and pore-forming mechanism has been explained.

To farther elucidate and confirm this mechanism, computational work is needed to quantify the interactions arise in between molecules and identify possible transient states. The concept holds promise as a structural platform for engineering biologically differential nanomaterials and adds to the growing tool kit of nano-defined materials demonstrating the versatility of applied chemistry and design.

Chapter 5

Antimicrobial Capsids

5.1 Introduction

As discussed in chapter 1, the spread of bacterial resistance to antibiotics stimulates antimicrobial discovery. Traditional antimicrobial mechanisms and methods seem insufficient to address the challenge of antimicrobial resistance. An alternative and effective strategy is to programme membrane-disrupting mechanisms using autonomously functional devised biomolecules having subcellular sizes. Here we describe a *de novo* antimicrobial peptide arrangement that – by emulating the virus architecture – assembles into antimicrobial capsids. These synthetic capsids destroy bacteria on contact by instantaneously porating their membranes.

Similar to capzip system described in chapter 4, the antimicrobial system explained in this chapter is inspired from nature, but in a different way. In capzip, we have started from a β-strand motif as an initial building block that exists in the natural protein (Lactoferrin) and we modified it to assemble into capsules. Here, we next draw inspiration from nature on the assembly of virus capsids and we combined this knowledge with our knowledge about antimicrobial host-defence peptides to build antimicrobial virus capsids from scratch.

In programming and building antimicrobial capsids from the very initial building blocks (amino-acids), we will first increase our understanding and control over synthetic capsid design. Next, this will allow us to further optimise designs for specific applications. The long term aim is to programme more sophisticated nano-devised biomolecular assemblies with specific functions for targeting specific cells.

This new capsid system also holds promise for addressing antimicrobial resistance. As illustrated in chapter 1, typical antimicrobial peptides disrupt bacterial membranes by forming pores, channels or carpets [86]. Every membrane lesion needs multiple peptide molecules to act collectively [188]. For this collective effect to happen, peptides have to reach a local concentration above a certain threshold, and this threshold is dependent on the nature of the peptide and its mechanism of assembly [17]. In contrast, the antimicrobial capsids presented in this chapter act like pre-concentrated bactericidal bullets to cause membrane poration and disruption instantly on the first contact. Hence these capsids present a strategy to apply antimicrobial peptides to bacterial membrane at a high enough local concentration to instantly disrupt the membrane.

In this chapter, the design of a synthetic viral capsid is discussed, as developed by our collaborators at NPL. The results show a good antimicrobial activity of the capsids with no apparent toxicity to human cells. As part of this PhD research, capsids have been characterised by AFM. In addition, the antimicrobial attack on the bacterial membranes was monitored by atomic force microscopy in real time to elucidate the mechanism of action.

5.2 Virus Capsid Design Principles

Native virus capsids are self-assembled from natural proteins. The majority of viruses can be classified into rodlike or spherical. The capsids of most spherical viruses arranged with icosahedral symmetry. The proteins forming such spherical virus architecture follow three universal principles for their self-assembly. First, they are packed together forming a symmetrical icosahedron. Second, the subunit proteins are positioned in identical chemical environments (quasi-equivalent) with respect to each other [189]. And third, they are clustered into closed supramolecular networks [190]. The arrangement of these subunits tiling a sphere, connected via weak non-specific interactions, suggests that quasi-equivalent lattices are the lowest energy possible for these subunits to form icosahedral arrangement [19].

There is large variation in the size and the number of subunits needed to build such a stable symmetrical icosahedron. The number of subunits necessary to form the capsid is dependent on their n-fold rotational symmetry. This rotational symmetry imposes geometric constraints on the allowed folds and interactions of the subunits (proteins). Often a lower n-fold rotational symmetry implies that more protein subunits are used or needed in a capsid. These overall differences are classified on the basis of the quasi-equivalence principle proposed by Donald Caspar and Aaron Klug [191].

For example, figure 5.1.A shows an icosahedron that consists of 20 flat faces of equilateral triangles arranged around a sphere. This resulted icosahedron has a 5, 3, and 2 symmetries. Such symmetries can be explained by assigning a rotational axis for the icosahedron to see how many identical projections can be achieved by rotating the icosahedron around the axis. In this particular situation, we could assign three different axes denoted by the black pentagon, triangle and the rectangle in figure 5.1.A. Rotating the designed icosahedron around the pentagon axis, five identical projections can be achieved, while only three can be achieved around the triangle and tow around the rectangle. The number of faces in any icosahedron is usually represented by the triangulation number (T-number). This number can be calculated graphically from an equilateral triangular net and using a simple equation:

$T = k^2 + k \times h + h^2$, with k and h are the distances (steps) between the successive pentagons on the virus surface for each axis, figure 5.1.B.

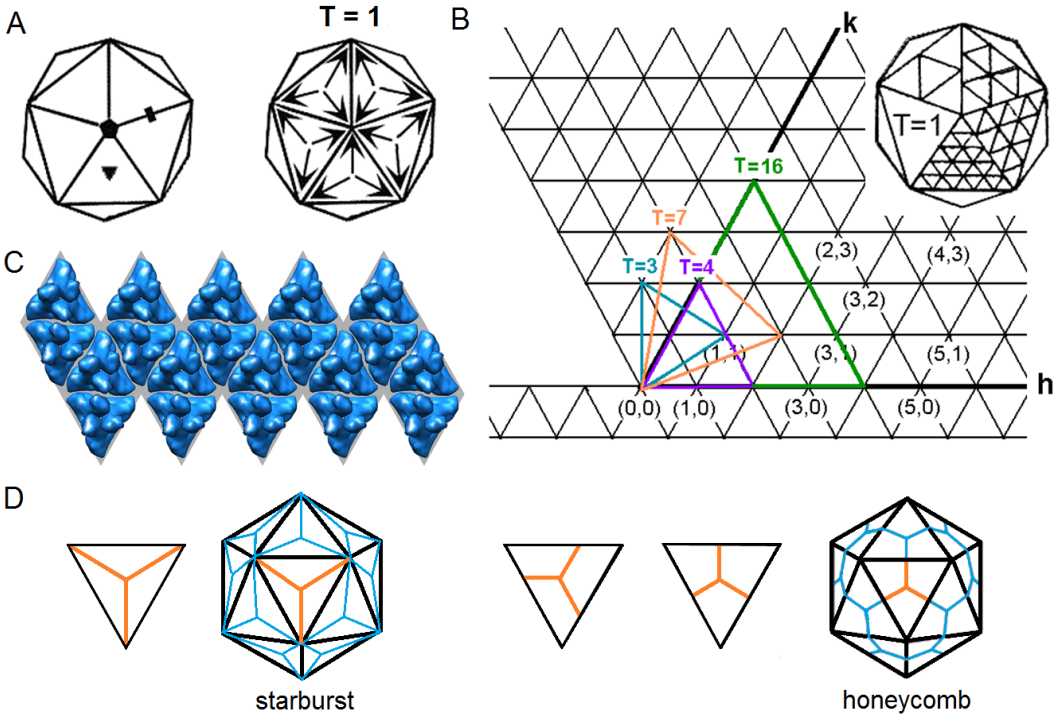

Figure 5.1: The geometry of viral capsids. (A) A schematic representation of an equilateral icosahedron. 20 flat triangular faces and 12 vertices are arranged around a sphere and related by 5-, 3- and 2-fold axes of rotational symmetry (diamond-, triangle- and rectangle, respectively). With each triangular face hosting three protein subunits (arrows at the vertices), 60 equivalent subunits in total, the icosahedron becomes a T = 1 capsid. (B) An equilateral triangular net relating icosahedral and quasi-equivalent symmetries. Each triangulation (T) number is calculated from (h, k) and denotes the number of smaller triangles arranged around local quasi-6-folds in one triangular icosahedron face. (Right inset) The net folded into an icosahedron showing different T numbers in individual triangles: (clockwise) 1, 4, 9, 16 and 25 (left). (C) A native virus (T=1) capsid unfolded into a triangular net with three identical subunits in each triangular face (Vdb 898, PDB 2GSY, reproduced from VIPER (http://viperdb.scripps.edu) (9). (D) Two arrangements of a C3-triskelion within a triangular unit leading to “starburst” and “honeycomb” propagation modes. In the starburst mode, the three equivalent legs of the triskelion serve as the altitudes of the triangle (left). Two variations of the honeycomb triskelion arrangement, symmetrical and asymmetrical, are given (right). For clarity central triskelions are shown in orange.

Each triangle (face) can be subdivided into three smaller triangles, facets. In reality, the number of these facets represents the number of subunits (proteins) needed to build up the capsid. For instance, a capsid with T=1 has 20 triangular faces and each triangle can be subdivided into three equal portions each hosting one protein. Figure 5.1.A (right) shows that each triangle is subdivided into three identical parts (black arrows).

This means that a total of 60 identical proteins would make up a T=1 capsid as shown in figure 5.1.C, where each blue triangle is made up of three identical proteins (blue protrusions). However, a capsid with T=2 needs (2x 20 x 3) = 120 subunits (proteins) to be built, or if T=3 then it needs (3x20x3) = 180 subunits and so on. The higher the number of subunits forming a capsid, the more precise collective interactions is needed between these building blocks to co-assemble together [192]. This level of precision is still challenging to achieve with *de novo* approaches.

However, to facilitate orthogonal assembly *de novo*, the same protein or peptide can be placed at each vertex of the triangle maintaining the three-fold symmetry around the symmetry axis denoted by the black triangle in figure 5.1.A. We have done that by covalently connecting three identical peptides together to form a rigid C3-triskelion as shown in figure 5.1.D (orange triskelions). Each C3-triskelion occupies one triangle which could propagate spherically in two different ways; “starburst” and “honeycomb” illustrated in figure 5.1.D. These two propagation modes follow the classical 5, 3, 2 symmetries explained above. However, as explained in section 5.4, our programmed C3-triskelion design will promote a “starburst” arrangement to direct a capsid-like assembly [17]. This is because the propagation of the C3-triskelions is induced by engineered hydrophobic interactions between cysteine amino acids at their termini. By looking at “starburst” arrangement in figure 5.1.D, each of these cysteine terminal is in a close distance to other four from adjacent triskelions facilitating the hydrophobic interactions among them which lead to a better stabilisation. “Honeycomb” propagations, on the other hand, allow only two adjacent triskelions termini to interact with each other. In order to stabilise this propagation, these interactions have to be strong oblique or orthogonal “sticky” interactions, which often need disulfide bridging as an additional stabilisation [193]. These later interactions are not facilitated within this presented design.

Based on these principles, we engineered an antimicrobial protein motif arranged into a C3-triskelion that assembles into capsid-like shells by clustering with other triskelion copies at its leg termini.

5.3 Elementary C1-Subunit Design.

To design the C3-triskelion as a capsid subunit, each leg which we call C1-subunit must be rigid and has a rod-like structure. These properties can be achieved by using α-helical coiled-coil protein motifs [194]. A coiled coil is a structure of protein bundles in which 2–7 α-helical motifs are coiled together like the strands of a rope. Figure 5.2 shows an example of dimeric and trimeric α-helical coiled-coils. The number of these interdigitated α-helices can be tuned and in viruses they are predominantly heterodimeric. The coiled-coils are usually stabilised via precise hydrophobic, hydrophilic or electrostatic interactions in between the helices. These α-helices making up the coiled coils are characterised by heptad repeats of their hydrophobic and polar amino acid residues designated as (abcdefg). The residues at positions a and d usually form the hydrophobic interfaces between the bundled α-helices as shown in figure 5.3.A, [195]. The average distance between each two hydrophobic residues along the α-helix sequence is 3.5 residues, which is less than one complete turn (3.6 residues) of a monomeric α-helix [194]. As a result, when two α-helices interact to form a coiled-coil, these little shifts of the hydrophobic residues along the helices induce a slight left-handed twist. This yields left-handed helix-crossing angles in the coiled-coil bundle. In addition to the hydrophobic interactions, complementary electrostatic interactions between residues at positions e and g help to stabilize the coiled coil. As illustrated in figure 5.3.A, this occurs between the successive heptads of partner strands (i.e. g-e' interactions: g of one heptad and e' of the following heptad on the other helix) [196].

To make the coiled coil antimicrobial, it is necessary to consider the hydrophobic a/d pairs in conjunction with the charged g/e' pairs [197]. As antimicrobial peptides or proteins are intrinsically positively charged [198], the coiled-coil could be engineered to be a heterodimer having an antimicrobial cationic strand and a complementary anionic strand. The antimicrobial cationic strands will be each arm of the C3-triskelion, while the complementary anionic strand will not be antimicrobial. However, this anionic strand is necessary for the subunits to propagate and form a capsid, as will be explained next section.

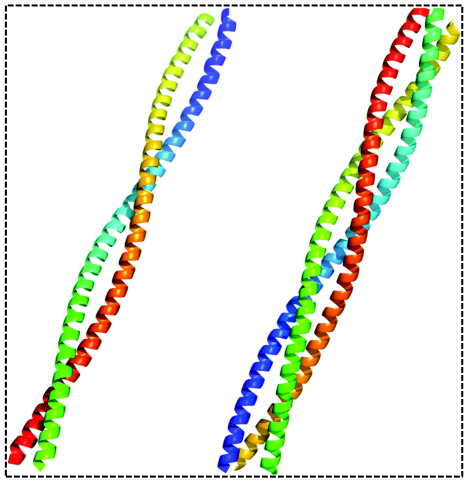

Figure 5.2: Structures of coiled coils. A cartoon presentation of a dimeric coiled coil (left) and a trimeric coiled coil (right) [8]

To enable an antimicrobial coiled-coil dimer, we designed the two positions (a and d) of the repetitive heptads in both the cationic and anionic strands to be isoleucine and leucine. This is to emulate the native leucine-zipper structures. It means that the two

helices stick to each other via hydrophobic interactions at these two positions. Further stabilisation of the dimer is achieved by the electrostatic interactions that arise between the complementary g/e' pairs. At these positions, the cationic amino acids (lysines) are used in the positive antimicrobial strands, while the anionic amino acids (glutamates) are used in the antagonistic strands as illustrated in figure 5.3.A&C.

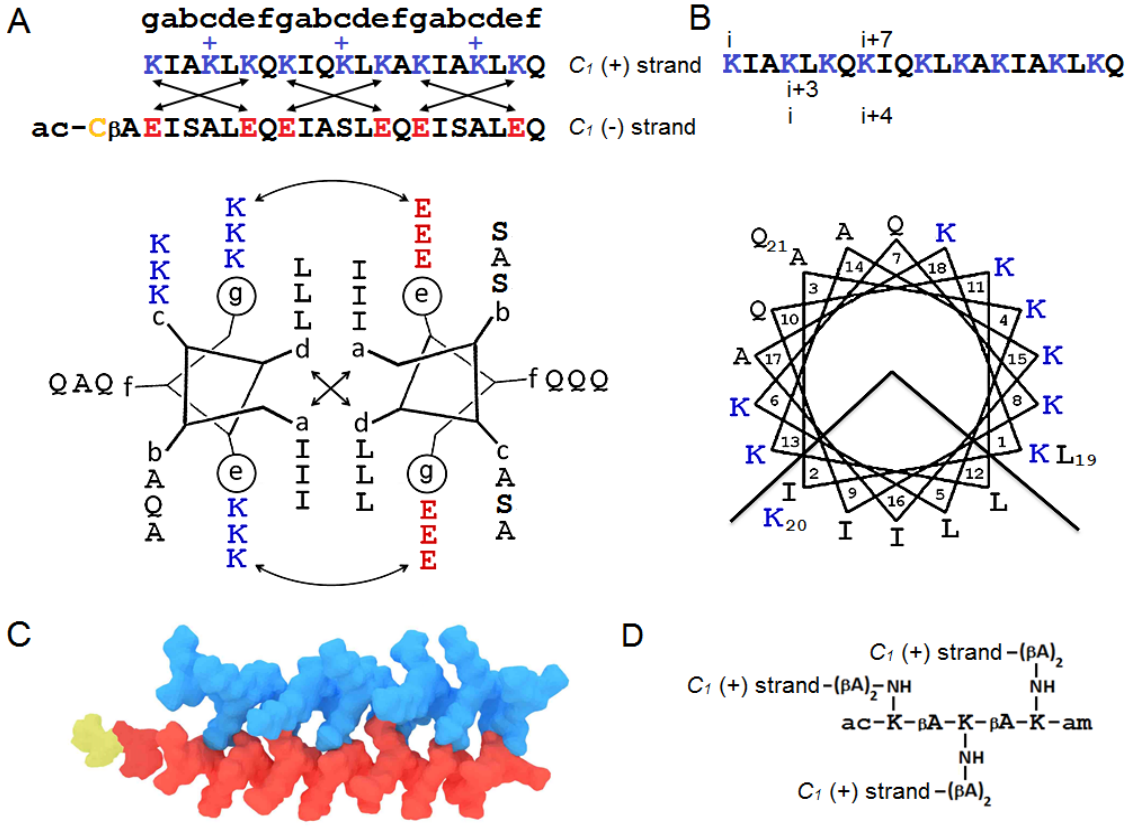

Figure 5.3: An elementary capsid C1-subunit. (A) The linear sequences of the subunit (upper) and configured onto a coiled-coil helical wheel with 3.5 residues per turn (lower). Antimicrobial (C1 (+) strand) and antagonist (C1 (-) strand) sequences are shown in blue and red, respectively, and are aligned under the coiled-coil heptad repeat pattern, gabcdef. The cysteine residue is shown in yellow. Curved double-headed arrows indicate electrostatic interactions between g and e' (circled) residues. Crossed arrows show the hydrophobic interface of the dimeric subunit formed by isoleucines and leucines in a and d, respectively. Unengaged positively charged lysines are highlighted with "+". These confer the dimer with an overall positive charge facilitating the binding of the subunit to anionic microbial membranes. (B) The linear sequence of the C1 (+) strand (upper) and configured onto a monomeric helical wheel with 3.6 residues per turn (lower), showing the clustering of amino-acid residues into two distinctive polar and hydrophobic faces. Monomeric (i, i+7) and coiled-coil (i, i+3 and i, i+4) helical spacings are shown, one of each for clarity. (C) A molecular model of the coiled coil C1-subunit (PDB entry 4DMD [18] rendered by Macromodel Shrödinger). (D) The chemical structure of a dendrimer C3-hub used to make the C3-triskelion, C3 (+) strand. βA denotes beta-alanine. Figure was reproduced from [17].

In addition, this arrangement makes the folded C1 (+) strand to follow the typical amphipathic structure of antimicrobial peptides explained in chapter 3. The folded helix will have two faces, hydrophobic and hydrophilic. Figure 5.3.B is the top-down view of the folded C1 (+) strand presented on a wheel-like schematic. The hydrophobic side of the helix is highlighted within the acute angle to include the two hydrophobic amino acids (leucine and isoleucine). On the other hand, all the hydrophilic amino acids including the positively charged ones are on the other side of the helix.

The hydrophobic positions a and d and the cationic/anionic positions e and g in each helical strand have amino acids that are engaged by interactions to stabilise the coiled-coil. Additional lysine residues were introduced into the antimicrobial strand at positions c that are not engaged and exposed to solvent as shown in figure 5.3.A. These residues interact with the anionic bacterial membrane and facilitate coiled-coil disassembly to boost the antimicrobial activity via freeing the other engaged lysine. The other solvent exposed positions, b and f, were occupied by alternating neutral polar glutamines and small alanines. In the anionic antagonistic strands, however, alternating serine with alanines residues were used in b and c positions to promote peptide solubility, with f sites taken up by glutamines.

The minimum requirement to form stable coiled coils is three contiguous heptads [199]. Similarly, antimicrobial peptides that have sequences of same lengths are reported to be significantly strong [200]. For these reasons, the full sequences of the both the negative and positive peptides are designed to consist 21 amino-acid residues as shown in figure 5.3.A-C. This resulted C1-subunit is an antimicrobial dimeric coiled coil (C1 +/C1-) offered an elementary rod-shaped anisotropic building block with size of ~ 3.2 nm (length) x 2 nm (width).

Circular dichroism (CD) spectroscopy revealed that when the positive and negative peptide monomers are not mixed together, they remain unfolded in solution. However, 90% of peptide monomers adopt a helical structure when the cationic and anionic peptides are mixed together in (1:1) molar ratio to form a coiled-coil dimer as illustrated in the schematic in figure 5.3.C [17].

The resulting coiled-coil C1-subunits, however, are not expected to propagate or assemble into capsids which was confirmed by TEM [17]. To enable each these subunits to be placed at the triangular vertices and to endow it with a capsid-like symmetry as discussed in section 5.2, further modifications were necessary to create what we call C3-subunit.

5.4 Capsid C3-Subunit Design

First of all, three copies of the C1 (+) strand were linked together into a triskelial hub shown in figure 5.3.D to form C3 (+). Each leg of the resulting structure folds with the C1 (-) strand giving rise to a rigid C3-triskelion as shown in figure 5.4. The three folded legs of the C3-triskelion are identical carrying a large positive net charge. This positive charge provides electrostatic repulsions keeping them away from each other. In addition, the three legs have polar faces which are designed to be solvent-exposed with no complementary interactions and none of them can facilitate undesired anti-parallel coiled-coil formation [201]. This rigid C3-subunit firmly fits into a triangular face with each leg span ~ 4nm as shown in figure 5.4. Yet, these C3-subunits cannot propagate into a spherical capsid as verified by TEM [17].

To promote the interactions of triskelions termini to propagate and form capsids, we have extended the N-terminus of the C1 (-) strand with a cysteine cap highlighted in yellow shown in figures 5.3.A&C and 5.4. Cysteine, in both reduced and oxidized forms, has the highest hydrophobicity among the proteinogenic amino acids [202]. Therefore it intrinsically tends to form secondary structure in aqueous media with the ability to do localised cross-linking [203]. For example, unpaired (uncross-linked) cysteines are known to induce particle formation in antibodies. This happens through clustered hydrophobic interfaces accompanied with the formation of non-native cysteine (more than two interacted cysteines) [204].

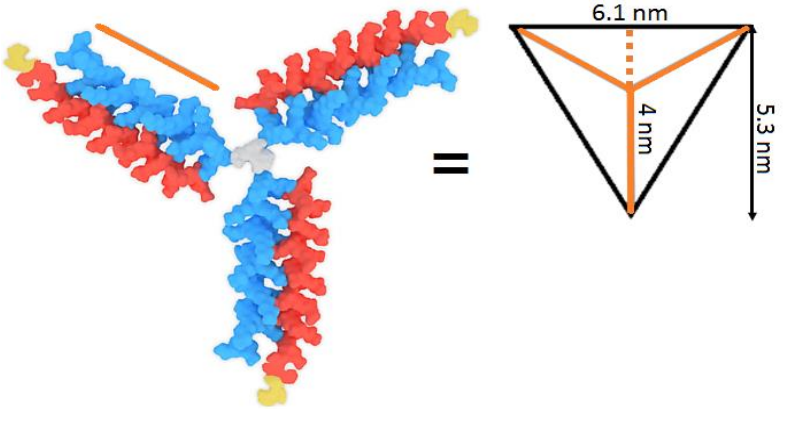

Figure 5.4: molecular model of the C3-triskelion (PDB entry 4DMD [18], rendered by Macromodel Schrödinger). Each subunit of the triskelion corresponds to the altitude of an equilateral triangle. A folded subunit spans ~ 4 nm (three coiled-coil heptads extended with the arm of the dendrimer hub and the cysteine cap), which makes the side of the hosting triangle ~6.1 nm. Figure was reproduced from [17].

Collectively, these factors suggest that C3-triskelions with its three arms capped at the N-terminal with cysteines should promote hydrophobic clustering at the vertices of triangular facets resulting in a capsid-like assembly.

5.5 Capsid Formation and Characterisation

As explained in chapter 2, capsids are prepared by mixing C3 (+) and C1 (-) with the molar ratio of (1:3) respectively. However, to promote the cysteine clustering explained in the previous section, we had to make sure that cysteines in C1 (-) strands exist in their free thiol form (not crossed linked/ disulfide). Therefore, (tris(2-carboxyethyl)phosphine) (TCEP) was added as a reducing agent to protect thiol groups from oxidation. The assembly takes place in a buffer solution of pH 7 to be close to the natural conditions and to maintain the balance of charged amino acids within the two strands.

AFM images and high resolution TEM revealed broadly uniform paracrystalline assemblies with an average diameter of 18 nm. Figure 5.5.A shows AFM images of capsids in solution. The height mask is set to be 2 nm (image on the left) and thus all assemblies having 2 nm height or more are highlighted by the pink colour. Another larger scale image is in figure 5.5.A (right) showing capsids (white dots) spread all over the substrate.

The colour scale for both images is 4 nm. The size analysis of the assemblies demonstrates that the majority of them have a diameter in the range of 15-20 nm, figure 5.5.A (lower right). Consistent with this, high resolution TEM micrographs show capsids deposited across the substrate.

The four highlighted capsids with the white squares are magnified to reveal some structural details. The average diameter of capsids is 18 nm as shown by the size distribution histogram, figure 5.5.C (right).

In our design, each leg of the folded triskelion (from the centre of the dendrimer hub to the acetylated N-terminus of C1 (-) strand) spans approximately 4 nm, figure 5.4. This makes the side of an equilateral triangle ~6.1 nm. The capsid assembly with T = 1 is believed to be unstable option as geometrically dis-favoured. This is because the triskelions are not able to orient around six-fold axes in this capsid, figure 5.1.D. Therefore, smaller assemblies are more likely to be observed.

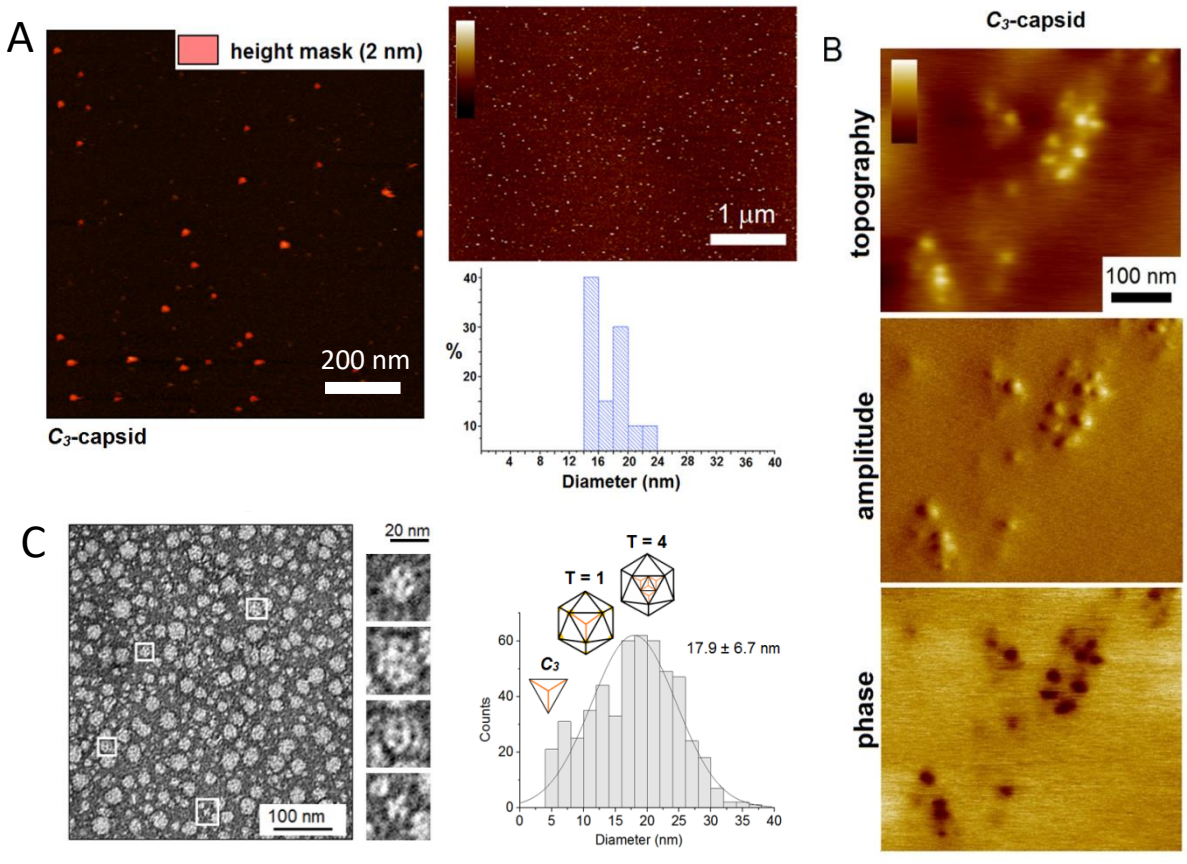

Figure 5.5: Capsid-like assembly characterisations of the C3-subunit. (A) in-water (buffer) AFM images of assembled capsids on mica. Colour scale bar (height) is 4 nm. The histogram is the capsids size analysis with height mask is set to be 2 nm. (B) In-air AFM images of assembled capsids on silicon recorded by a colleague in NPL. Colour scale bar (height) is 15 nm. (C) High resolution electron micrographs for C3 (+) strand (100 µM) assembled with C1 (-) strand at 1:3 molar ratio, with individual structures highlighted by white squares. (Right) diameter distributions of the assembled capsids with corresponding sizes calculated for the triskelion fitted into a triangular facet (C3) and T capsids.) EM data was acquired by a colleague in NPL. Figure reproduced from [17].

Since the triskelions can only pack into equilateral triangular facets, the next possible assembly, in which triskelia termini cluster into clearly defined six- and five-fold symmetries, is a T = 4 capsid of ~20 nm in diameter shown in figure 5.6.A. Triskelions readily fit into this capsid, figure 5.6.B, which is amply complemented by the most abundant diameters observed by AFM and TEM.

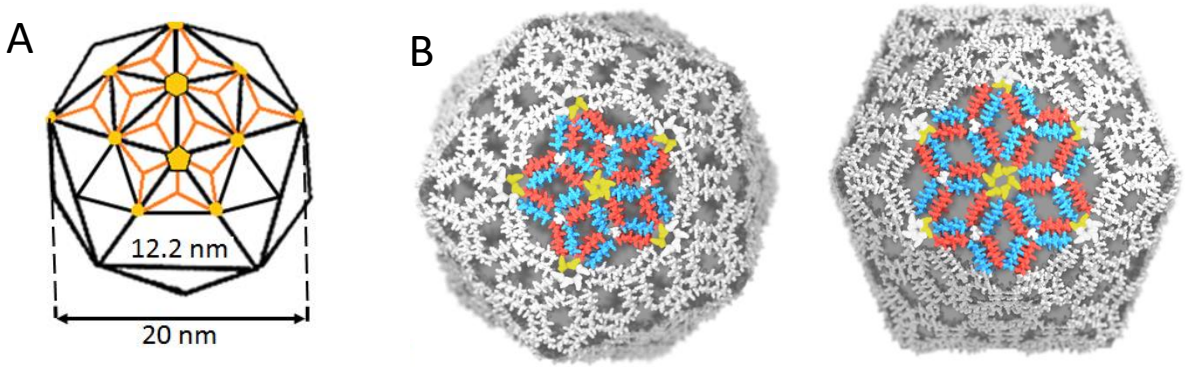

Figure 5.6: Capsid Icosahedron model with T=4. (A) A T = 4 icosahedron with four facets in each triangular face with each accommodating one triskelion. For clarity, only a partial network of triskelions in the icosahedron is shown. Five- and six-fold axes are highlighted by yellow diamonds. The diameter of the icosahedron and the side of its triangular face are calculated based on the triskelion dimensions shown in (Fig 4). (B) A model of a T = 4 capsid assembled from the C3-subunit with matching those from (A) and (Fig 4). For clarity, only one of five- and six-fold axes each is shown in colour. Figure was reproduced from the published paper.

5.6 Antimicrobial Activity and Mechanism of C3-Capsids

The antimicrobial activity of capsids as discussed is expected for the positively charged C3 (+) triskelions. In contrast, C1 (-) is not expected to show any toxicity against bacterial cells. In addition, both peptide strands should not show any toxicity against eukaryotic cells.

To probe this, CD spectroscopy was used to monitor the patterns of structural folding for C3 (+) and C1 (-) strands when mixing with negatively charged and neutral lipid vesicles. The peaks that indicate helicity of peptides shown by the CD spectra means that the peptide interacts with these vesicles and induce folding. These interactions indicate that the peptide is toxic toward cells that have membranes composed of similar lipids [73, 159].

As discussed, bacterial cell membranes were mimicked by the anionic unilamellar vesicles (AUVs) formed by the lipid mixture of either (DLPC:DLPG) or (POPC:POPG) with the mass ratios (3:1) respectively. However, mammalian membranes were modelled by forming zwitterionic unilamellar vesicles (ZUVs) using either DLPC or POPC lipids. of similar lipids [73, 159].

The CD spectrum of C3 (+) mixed with AUVs shows negative peaks at 209 nm. This typically indicates that the C3 (+) peptide folds into a helical structure upon binding to the negatively charged membrane implying toxicity toward it. However, the spectrum does not show such folding behaviour when mixing C3 (+) with the ZUVs indicating no toxicity toward human

cells. The CD data also indicates that C1 (-) does not interact and fold with both types of lipid vesicles, and no toxicity is expected toward them [17].

In addition, the antimicrobial activities of capsids were tested on bacterial cells via MIC assays [171] and their haemolytic activities were tested on human erythrocytes via LC_{50} assays. These activities were then compared with those for C3 (+) triskelions and the other known antimicrobials as listed in table 5.1.

Cell	**Peptide**[a]					
	C_3 (+)	C_3-capsid	cecropin B	daptomycin	polymyxin B	gramicidin S
	Minimum inhibitory concentrations, µM					
P. aeruginosa (ATCC27853)	3	12	<2	>100	<1	≥40
S. aureus (ATCC6538)	50	>100	>100	7.7	<50	>20
E. coli (K12)	1.5	3	<1	>100	<1	>20
B. subtilis (ATCC6633)	1.5	3	>50	7.7	1.5	≥40
S. enterica (ATCC700720)	3	3	3	>50	<1	<10
E. faecalis (OG1X)	50	>50	≥25	>100	>100	ND
K. pneumoniae (NCTC 5055)	>12	<25	<1	>50	<1	ND
(LC_{50})[b]*, µM*						
Human erythrocytes	>150[c]	>150	>150[c]	>150[c]	N/D	>20

Table 5.1: Biological activities of peptides used in the study [a:] C_1 (-) strand was inactive (>250 µM); [b:] median (50%) cell death compared with untreated cells. [c:] haemolysis of 3-10% observed at higher concentrations. Gram negative and Gram positive are highlighted in red and blue, respectively. N/D – not determined. All tests were done in triplicate.

The table shows that C3-capsids and C3 (+) triskelion exhibit strong antimicrobial effects with no apparent haemolytic activities at micro-molar concentrations. MIC values for C3-capdis and C3 (+) triskelions were typical of polypeptide antibiotics within the phenotypic tolerance of bacteria to antibiotics [205]. In comparison, the C3-capsids have shown higher MIC values of MIC over the C3 (+) triskelion, indicating a smaller antimicrobial effect. This could be as a result of the coiled coil formed with the negatively charged strand that prevent C3 (+) from binding to the membrane.

This effect was minimised, however, by having extra lysine residues exposed to liquid in the C3 (+) strand sequence which initiate binding to the negative membranes. These then will trigger the disassembly of capsids. On the other hand, C1 (-) strand was found biologically inactive, table 5.1.

Consistent with the biological results, AFM images showed that C1 (-) did not interact or disrupt negatively charged lipid bilayers. Figure 5.7 is a time-lapse AFM imaging of negatively charged membrane. The first image (-3 minutes) was acquired before injecting C1 (–) peptide, showing a flat membrane surface as a reference. At time (0) minutes, 1 µM of C1 (–) peptides was injected on the sample. Next, AFM imaging was carried out on the same area for 56 minutes with a speed of 4 minutes per frame. As expected, the membrane remained intact (images 4-56 minutes) and no effect of C1 (-) on the bacterial membrane was probed. As a control, 0.5 µM of C3 (+) peptide was injected to the same sample at 61 minutes.

Consequently, the next image (65 minutes) shows that C3 (+) disrupted the membrane confirming that the membrane is responsive to antimicrobial peptides.

Next, the effect of C3 (+) peptide on bacterial model membrane was monitored in real time by AFM. Figure 5.8.A shows time lapse AFM imaging of bacteria model membrane incubated with C3 (+). The first image, (-3 minutes) was acquired before injecting the peptide, showing a flat membrane surface as a reference. The flatness of the surface is demonstrated by the cross-section profile shown in figure 5.7.B1 for the corresponding area marked by the white dashed line.

The subsequent images (3-21 minutes) shown in figure 5.8.A, are all acquired after adding 0.5 µM C3 (+) peptide. Small pores appeared shortly after peptide injection, which continued expanding over the time of the experiment.

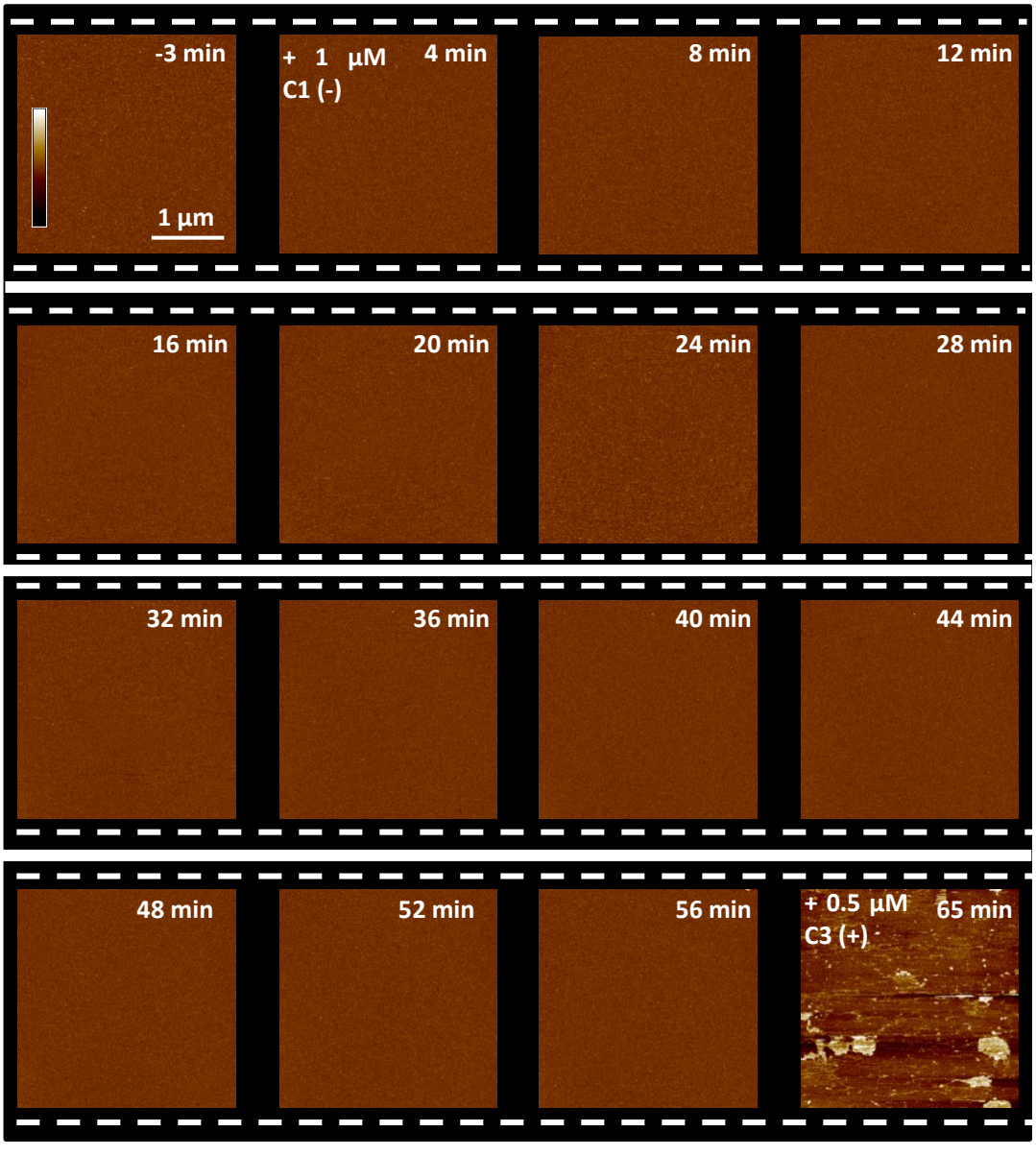

Figure 5.7: C1(-) effect on bacterial model membrane. In water AFM topography imaging of supported lipid bilayers incubated with 1 µM C1 (-) peptide for images (4 -56 minutes) and with 0.5 µM C3 (+) for image (65 minutes). Image (-3 minute) is before adding any peptide (control). Scanning rate is 4 minutes per frame. The time stamp corresponds to the final line of each AFM scan, referenced to the time (00:00) of C1 (-) peptide injection. The final image (65 min is captured after injecting 0.5 µM of C3 (+) peptide showing a big disruption of the membrane. Colour scale is 10 nm.

Figure 5.8.B2&B3 shows the cross-section profiles of expanding pores at the areas highlighted by the white dashed lines of the corresponding images. The profiles demonstrate that the pores have depths of ~ 3 nm matching the thickness of the lipid bilayer and the length of C3 (+) arms.

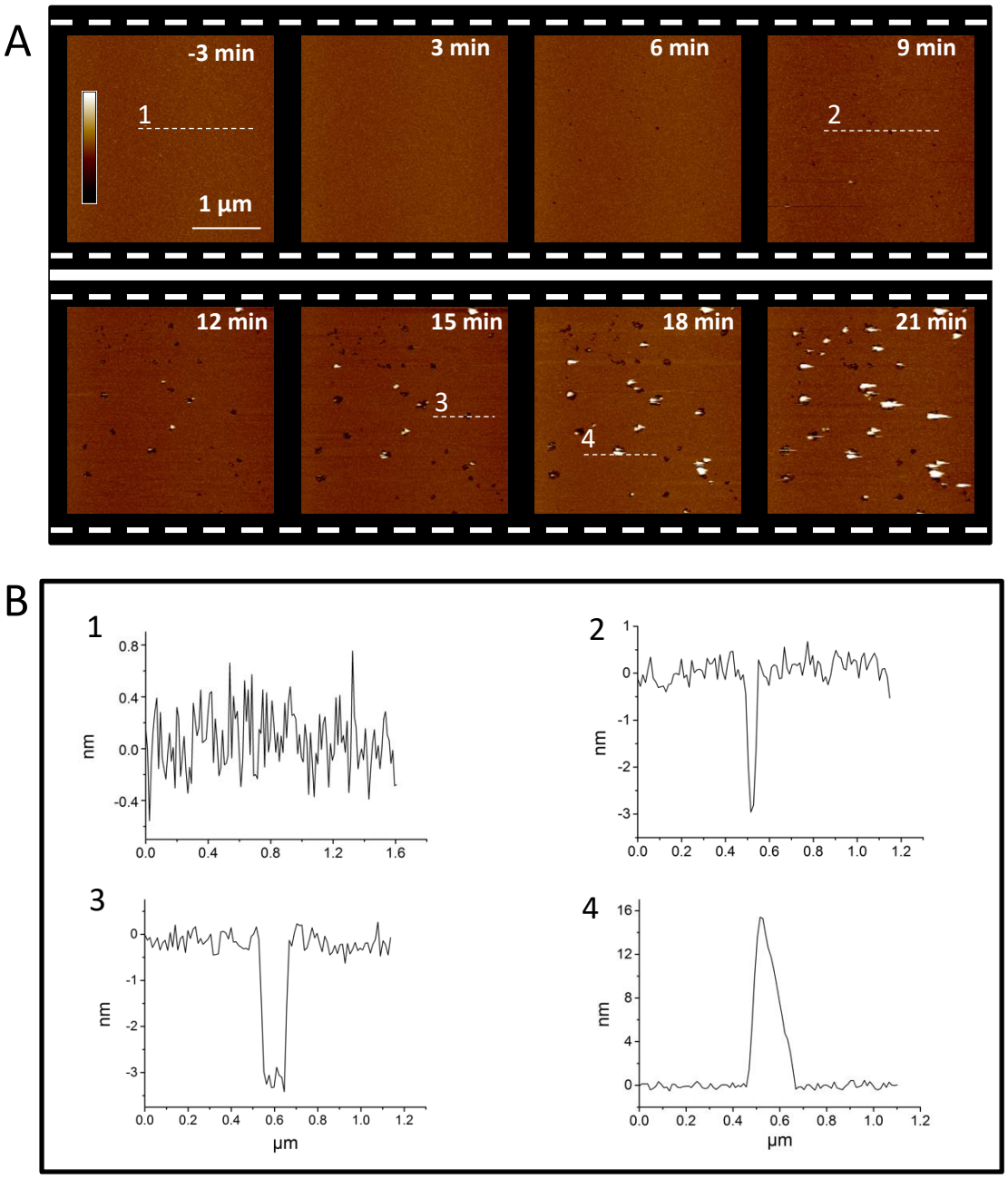

Figure 5.8: C3 (+) effect on bacterial model membrane. Time-lapse AFM images of bactewrial model membrane incubated with C3 (+) and pores characterisation. (A) In water AFM topography imaging of supported lipid bilayers incubated with 0.5 µM C3 (+) peptide for images (3 -21 minutes). Image (-3 minute) is before peptide injection (control). Scanning rate is 3 minutes per frame. The time stamp corresponds to the final line of each AFM scan, referenced to the time (00:00) of C3 (+) peptide injection. Colour scale is 10 nm. (B) Cross section profiles of areas highlighted by the white dashed lined on the images.

Noticeably, there are aggregations (yellow blobs) developed on the edges of the pores over the time of experiment. The sizes of these aggregations vary and could reach up to 20 nm in height as shown in the cross-section profile in figure 5.8.B4.

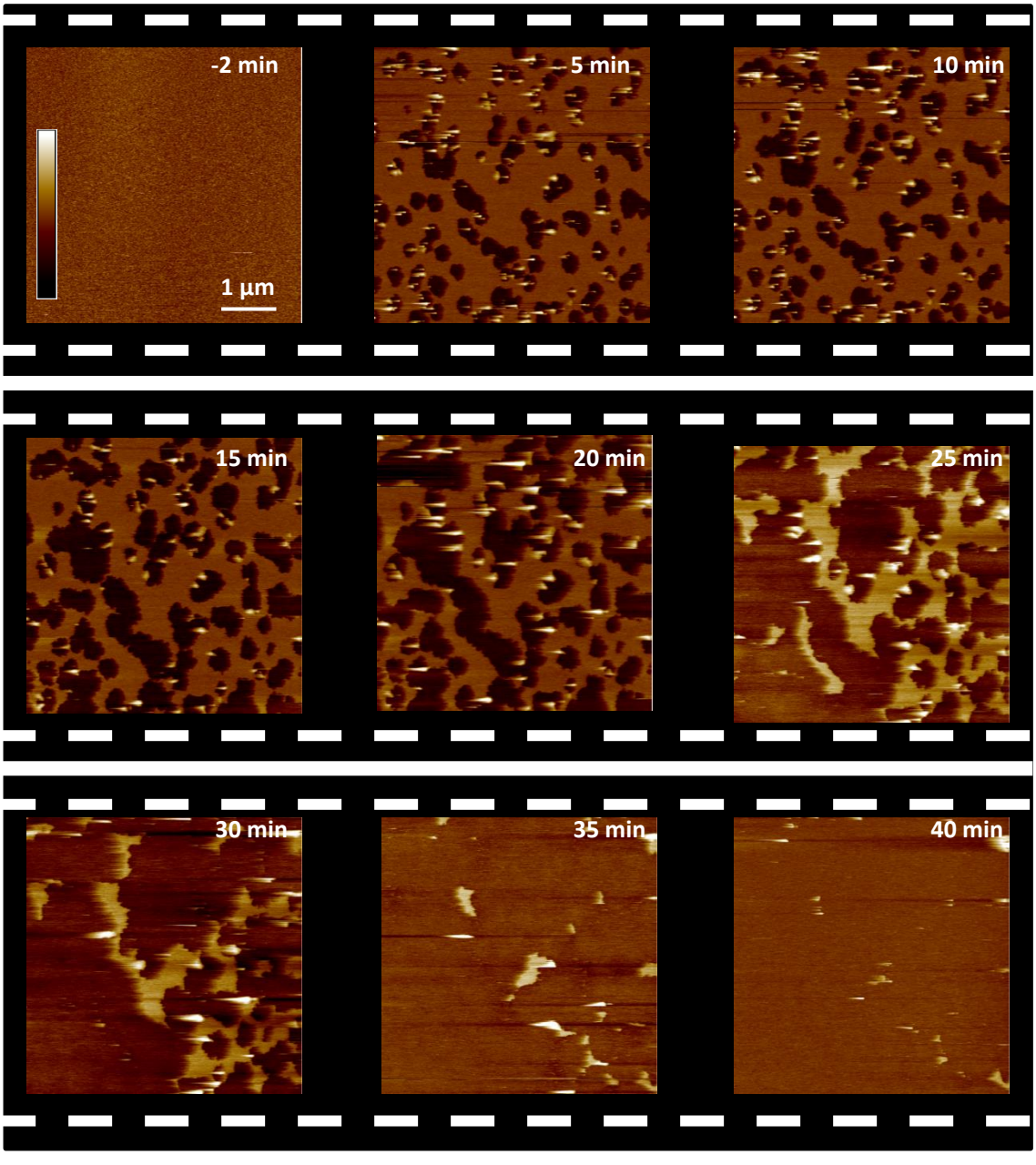

Figure 5.9 In water time lapse AFM imaging of ~ 1 µM C3-capsids porating bacterial model membranes. Topography (height) images, captured at 5 minutes per frame, are shown. The time stamp corresponds to the final line of each AFM scan, referenced to the time (00:00) of capsid injection. The first image (-2 minutes) was captured before capsids injections. Colour scale is 10 nm.

The effect of the assembled C3-capsids on the bacterial model membrane was also monitored by AFM. The aim is to track the attacking process of intact capsids followed by a gradual disassembly during the poration process within the bacterial membrane, similar to what illustrated for capzip in chapter 4. The samples of C3-capsids were prepared following the same protocol explained in section 2.

Figure 5.9 shows time-lapse AFM images of bacterial model membrane incubated with assembled C3-capsids. As usual, the first image (-2 minutes) was captured before the injection of any capsids, showing a flat membrane as a reference. At time (0 minutes), 1 µM of assembled C3-capsids were injected into the sample.

The subsequent images show expanding pores that start to form immediately after injections of the capsids. Given the time resolution of these AFM experiments (5 minutes per frame), earlier stages of pore formation could not be observed.

Since the first recorded image (5 minutes) did not show intact or dis-assembling capsids, it is assumed that capsids were completely disassembled before acquiring the first image.

As expected, the pores formed by the capsids have a depth of 3 nm, matching the thickness of the lipid bilayer and the length of C3 (+) triskelion arm. Figure 5.10 shows the cross-sectional profile of the line drawn in the second image in Figure 5.9. Here, and similar to what was observed in Figure 5.8, aggregation is noticed on the edges of the pores (yellow blobs).

Since similar aggregations appeared when membrane is attacked by capsids and by C3 (+) monomers, this demonstrates that the aggregation happens between the C3 (+) triskelion and membrane components.

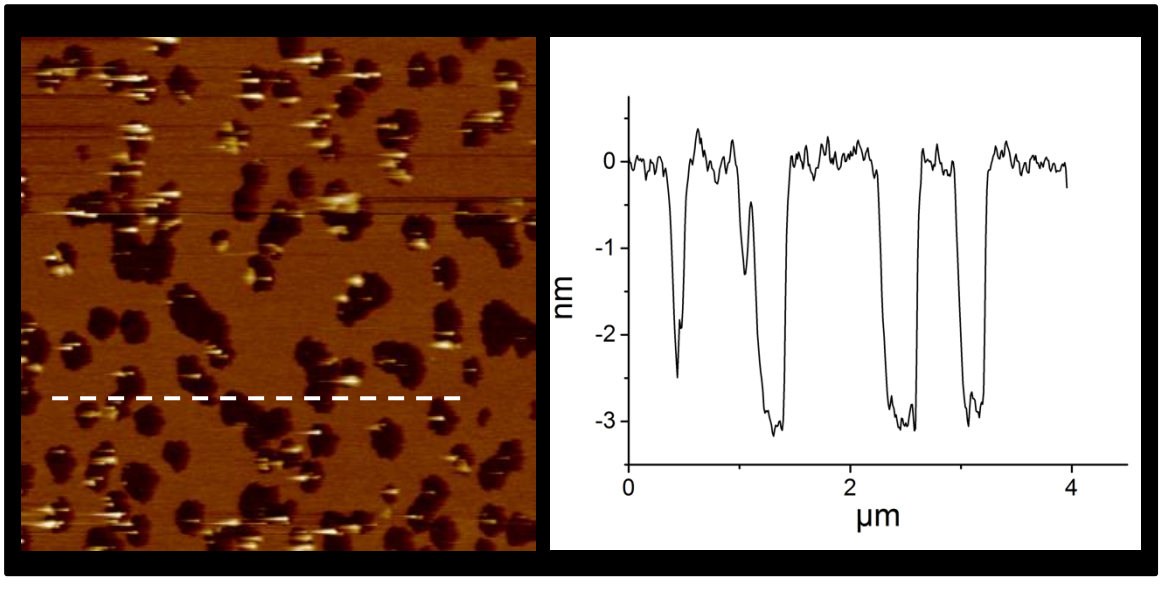

Figure 5.10: Pores sizes formed by C3-capsids in bacterial model membrane. (Left) is in liquid AFM image taken from figure (9), after 5 minutes of capsids injections. C3-capsids concentration is ~ 1 µM. (right), the cross section profile representing the area highlighted by the white dashed line on the image. Colour scale is 10 nm.

Since capsids disassembly take place during the first 5 minutes of the attack, we next improved the time resolution to image the early stages of the process, with at best 13 seconds per frame. As mentioned in chapter 2, we used a modified AFM head designed for the photothermal actuation of miniaturised cantilevers (REFS) [156].

Figure 5.11.A shows time-lapse fast-scan AFM images of bacterial membrane incubated with 3 µM capsids. Upon the addition of the capsids on the flat membrane (at 0 seconds), poration became apparent within seconds. This indicates that capsids instantaneously disassemble on the membranes. Even with the ability to acquire a frame every 13 second, intact capsids could not be imaged on the membrane. The formed pores grew in size and merged, resulting in the complete removal of the phospholipid matrix within 5 min after exposure to the C3-capsids. The depths of the pores as shown in figure 5.10.B were consistently ~3 nm, consistent with C1 (+) strands spanning the bilayer.

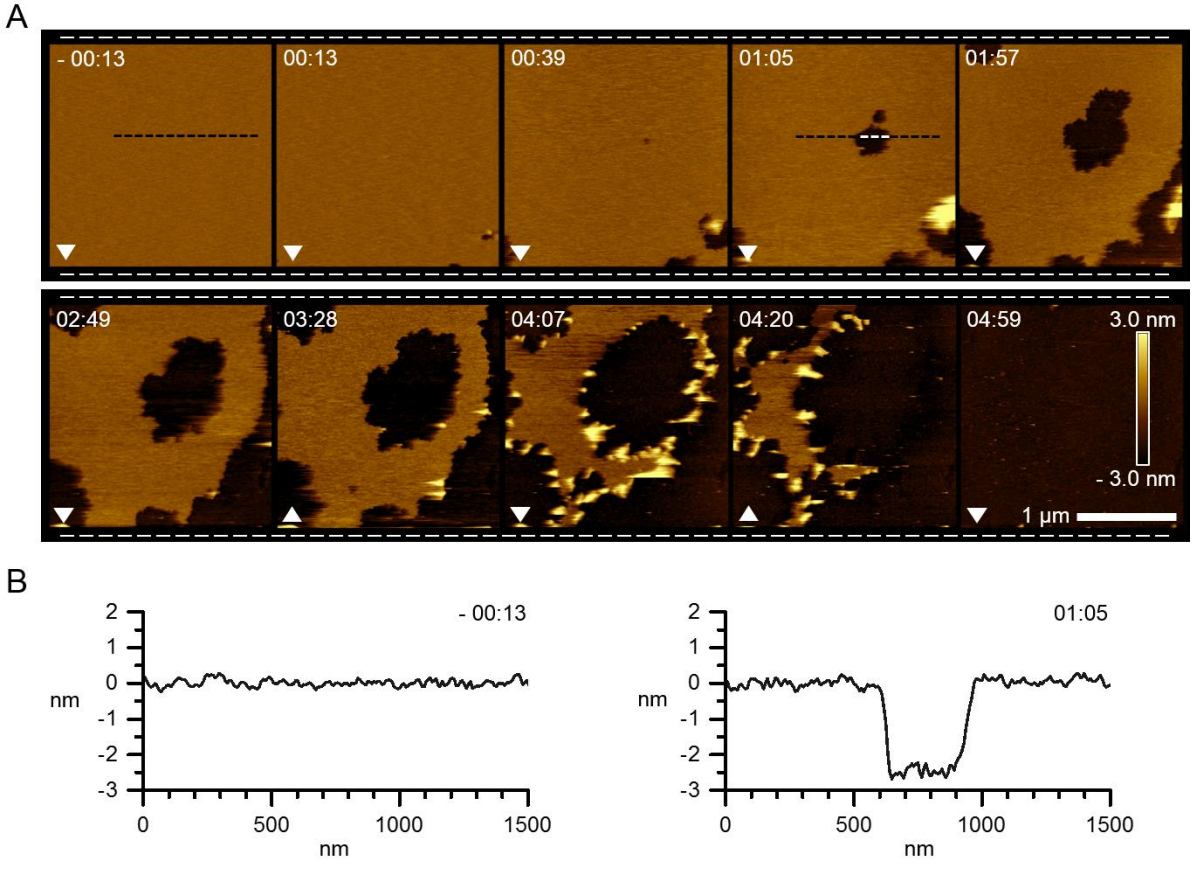

Figure 5.11: C3-capsids porating phospholipid bilayers. (A) In-liquid high speed AFM imaging of supported lipid bilayers treated with C3-capsids (~ 3 µM total capsid). Topography (height) images, captured at 13 seconds per frame, are shown. The time stamp corresponds to the middle line of each AFM scan, referenced to the time (00:00) of capsid injection. White arrowheads indicate the AFM scan direction. (B) Cross-sections along the lines marked in (A, -00:13 and 01:57) before (left) and after (right) the addition of capsids

5.7 Discussion

The capsid design has two main characteristics that each support a specific function. Firstly, the assembly is stable in solution as well as in the presence of mammalian cell membranes. This is important as the antimicrobial capsid may effectively target intracellular pathogens via the ability to traverse mammalian membranes and reach the cytoplasm without cytotoxicity.

Secondly, the capsids bind to microbial membranes followed by an immediate disassembly into their independent components, which does appear at the target membrane at a high local concentration. These components are the antimicrobial C3 (+) triskelions that fold and porate the microbial phospholipid membrane, and the anionic antagonist C1 (-) strands that convert into random coil and stay in solution.

Because all three legs in the C3 (+) triskelion are identical, each has the same ability to bind and insert in the bacterial membrane. As the length of each strand matches the thickness of the phospholipid bilayers (3-4 nm), each arm of the triskelion (C1 (+)) is designed to insert in the bilayers in a transmembrane manner. Finally, since all the strands would have the same orientational preference in the membrane, for which they compete, this non- balanced energetic state of triskelions induces them to move and diffuse to generate wider pores and disruption of the membrane until the complete removal.

Figure 5.12 is a schematic representation of the C3 (+) triskelions and possible orientations of their arms within the environment of bacterial membranes. As explained in the result section, the length of the folded arm matches the thickness of the lipid bilayer.

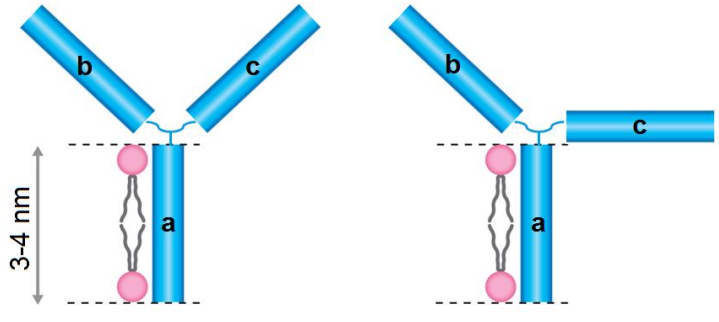

Figure 5.12: Schematic representation of pore edges with the thickness of the SLB (3-4 nm). For clarity, only one C3 (-) strand with three C1 (-) strands (blue cylinders) and one phospholipid per layer are shown (aliphatic chains in grey, headgroups in pink).

When interacting with the negatively charged lipids, all arms are expected to adopt helical structure spanning 3-4 nm. The geometric constraints make the existence of three arms inserted in the lipid bilayer improbable. The more likely scenario however is that the three arms compete with the same probability to get in the membrane and when the one of them get in the other two stay out. The inserted arms in the membrane (arms a in figure 5.12) can stablise by the same mechanism explained for the helical antimicrobial peptide (amhelin) in chapter 3. The amphipathic structure of the helix induces a transmembrane orientation in which the peptide hydrophobic side hides within the hydrophobic tails of the lipid chains while the hydrophilic side stays exposed toward the pore where the aqueous medium is.

The other two arms, if folded and not inserted, will still be amphipathic helices seeking stabilization, possibly in a way that leads to the aggregation observed on the edges of the pores, figures 5.8.A, 5.9 and 5.11. One may speculate that the lipids chains stack on these exposed arms, hiding the hydrophobic sides of the peptides from the aqueous medium. The positive and hydrophilic side preferably interact with the lipid headgroups or the aqueous solution.

5.8 Conclusion

In this chapter, a concept of a platform for engineering antimicrobial capsids is demonstrated. Capsids can be assembled from relatively short amino-acid sequences. Given that there are thousands of antimicrobial peptides reported in the literature [66], each of these may be used to construct a self-assembling capsid protomer.

Atomic force microscopy has the ability of imaging and tracking the process of antimicrobial attack on the bacterial model membranes at high resolution. The presented AFM data is consistent with the data of other techniques applied in studying the capsid system (e.g., CD and TEM).

Further experiments that could be done are imaging the effect of capsids on the human cell membranes by AFM. This could be achieved by using DLPC or POPC lipids. These experiments will not provide new information but could confirm the biological data of negative cytotoxicity of capsids which was also observed by the CD. In addition, resolving the orientation mechanism of the three arms within the membrane as well as the dynamic equilibrium could be achieved via further experiments employing linear dichroism or NMR techniques.

Chapter 6

Next Steps towards Commercialisation

6.1 Overview

As explained in chapter 1, antimicrobial resistance is considered a global challenge in the 21st century. One contributing factor to this problem is the low interest showed by the pharmaceutical companies over the last five decades to invest in developing new antibiotics. One reason is that it is as costly a development as that for other types of medicines but with a higher risk: The antibiotic market is not stable and predictable. The global demands on antibiotics fluctuate with the waves of the bacterial infections attacking particular areas at particular times. Hence, pharmaceutical industry prefers to invest in developing drugs for chronic diseases that require long term treatments [27, 29]. The demand for such drugs can be better estimated and the financial studies for such investments including, revenue, costs and profits forecasts are achievable.

Unfortunately, regardless the humanitarian need for certain drugs, investment in drug developments from the perspective of business is normally evaluated based on the profit. Investors usually have many proposed business opportunities that are run through an evaluation process to finally invest in those having the lowest risk and the highest expected profit.

In fact, since 2000, more than 20 new antibiotics have been produced and distributed to markets and more than 40 other drugs are now in active clinical development [206]. However, only few antimicrobial peptides (AMPs) are being developed and reached clinical trials [207]. This antibiotic development move is due to the recent pressure that government bodies are putting on big pharma to invest in this field [207]. In addition, governments provide support and incentives to stimulate such investments as they are in the interest of the national security.

Entrepreneurs try hard to reduce the risk of any new businesses to become more attractive opportunity for investors. Therefore, one should aim to reduce the investment risk for developing AMPs.

This chapter sheds light on how investment in developing AMPs could be a successful business opportunity. It includes a detailed business plan for an application of AMPs which is antimicrobial wound dressing business.

6.1.1 AMPs Possible Commercial Applications

As mentioned in chapter 1, AMPs could be considered as the next generation of antibiotics. However, this does not mean that medicine is the only application possible. In fact, there are many other possible and feasible applications which have big steady markets. For instance, it could be used for active packaging which requires an antimicrobial packaging system for food products to extend the products shelf life. AMPs can also be used in personal care & cosmetics products as preservatives and to deter skin pathogens. In addition, AMPs are suitable for agricultural applications as plants protection agents as well as additives within the animal nutrition system. Finally, AMPs can be used for wound management as cream and ointment or it could be embedded within the wound dressings to protect the wound from infections and accelerate healing. The last application is the one studied in detail in this commercialisation chapter.

6.1.2 Antimicrobial Wound Dressings

Unlike the pharmaceutical applications of AMPs as medicines, the market of antimicrobial wound dressings is considerably more stable and predictable. Every person and pet has a risk of being physically wounded especially during surgical operations or during heavy activities. Wounds can range from acute to chronic. Chronic wounds are those that do not heal in an orderly set of stages and in a predictable amount of time and often remain in the inflammatory stage for too long. Open wounds have to be managed in order to accelerate healing. Such management can be achieved via different methods including applying special dressings to cover the wound. There are many types of wound dressings available in the market and each is preferred for particular wound situation [208, 209]. Open wounds are usually vulnerable to bacterial infections, and therefore it is recommended in some case and necessary in other to protect the wound from bacteria during the healing time.

Wound infection increases exudate to distressing levels, causes inflammation, pain and odour, and can result in further surgical interventions for debridement or excision [210]. Yet, modern dressings and best-practice techniques can reduce wound infection from its current, unacceptably high base.

Hence, antimicrobial wound dressings are available and take up to 11% of the wound management market according to study in 2013 [211]. Such dressings are usually used frequently as consumables at hospitals, clinics and the related industries.

In addition to being a relatively stable market, the development of antimicrobial wound dressings is easier than developing a drug from the perspective of regulations. This is because such application is considered topical and cosmetic leading to fewer and quicker

steps required for clinical approvals. According to FDA, wound dressings require “510(k)” approval which is designed for class 2 medical devices [212]. This rather simpler regulatory pathway reduces the R&D costs and the overall risk of the investment.

More importantly, developing AMPs for wound dressing application will pave the way for the next steps, which could be antibiotic drug development. With similar but longer regulatory steps required for a new drug, AMPs could enter the clinical trials with lower risks from investment and safety perspectives.

Based on these rationales, we have persuaded a company to develop such new technology. The company, which is not mentioned anywhere in this thesis for reasons of confidentiality, has signed an R&D deal with the National Physical Laboratory (NPL) to develop antimicrobial wound dressings using AMPs as the active ingredient.

Here, I am presenting a business plan for such investment. The plan starts from a market study including the market evaluation and growth forecasts, the available products and the market gap. Next, I explain our product and its unique value propositions (UVPs). Then, the products development and milestones are outlined. Next, the plans for manufacturing, marketing and selling are described. Finally, I present the financial study of the project including an estimation of the investment needed, risks register and exit plans.

6.2 Wound Dressings Market

Current estimates indicate that wounds account for almost 4% of total health system costs [213]. The breakdown of wound costs in the acute setting, 15-20% material costs, 30-35% nurse time and >50% hospitalisation [213]. In a typical hospital setting today, between 25% and 40% of beds will be occupied by patients with wounds. In addition, in the community, management of wounds takes up over half of all resources [214].

A wound is defined as a disruption in the continuity of the skin or mucosa due to physical or thermal damage, or an underlying medical condition [215]. Wound healing is a complex, dynamic, and multistep process which occurs after skin damage leading to tissue repair. Although the skin normally undergoes repair after a disruption, the healing process can be affected in different conditions such as diabetes mellitus, infections, venous/arterial insufficiency, among others.

Disease states such as diabetes have a surprisingly high association with wounds. In Europe, diabetes already affects 20.2 million people, a figure predicted to rise by 37% over the next two decades [216].

To enhance healing, a wide range of wound dressings are available. However, a thorough wound assessment (e.g., wound type, size, depth, or colour) is required to choose the appropriate dressing. The emergence of new dressings has brought a new perspective of wound healing, but there is no superior product yet to treat acute and/or chronic wounds [215].

6.2.1 Market Size & Growth

Global

According to a market research report by Technavio, the global wound care market was valued at $10.9 billion in 2016. However, other studies have estimated this to be only $6.7 billion worldwide [217]. Antimicrobial dressings comprise around 11% of the wound care market. Thus, the global market size for antimicrobial dressings was $990 million in 2015, predicted to reach $1.37 billion by 2020, representing a compound annual growth rate CAGR of 6.65%. Based on this ratio, the estimated market size for 2017 is at $1.126 billion.

North America Market Share & Revenue

North America accounts for 35% of the global wound dressing market [218]. This is resulting in annual spending for antimicrobial dressing around $ 494 million in 2017.

Europe Market Share & Revenue

The Europe wound management market in 2016 was valued at $2.22 billion [219]. Therefore, Europe controls around 20.37% of the global wound care market. Assuming this percentage is consistent across the wound care products including antimicrobial dressings, then the size of Europe's antimicrobial dressing market is approximately $228.5 million in 2017.

England Market Share & Revenue

Antimicrobial dressings accounts for about £110 million per year in primary care in England, with more than £20 million spent on silver dressings alone [220].

6.2.2 Antimicrobial Dressings Available in the Market

Antimicrobial dressings can be categorised based on the active antimicrobial material used in the product. The most known materials are; honey, silver, iodine, activated carbon cloth, chlorhexidine, dialkylcarbamoyl chloride (DACC) and polyhexamethylene biguanide (PHMB). Silver antimicrobial dressings are still the most common type. This is because several pathogenic bacteria have developed resistance against various antibiotics leading

to the re-emergence of silver after it has been avoided due to the associated toxicity [221]. Antimicrobial dressings can also be categorised based on their functions and the wound type.

Tables 6.1 and 6.2 include lists of the available types of antimicrobial dressings, brand names, manufacturers' names categorised according to their function and the active antimicrobial material used respectively.

6.2.3 Competitive Landscape

The ideal wound dressing is usually chosen based on the wound type: The dressing should be made of a suitable material (textile carrier). However, there are general criteria all wound dressings should comply with. These are the ability to:

a) Provide or maintain moist environment. b) Enhance epidermal migration. c) Promote angiogenesis and connective tissue synthesis. d) Allow gas exchange between wounded tissue and environment. e) Maintain appropriate tissue temperature to improve the blood flow to the wound bed and enhances epidermal migration. f) Provide protection against bacterial infection. g) Should be non-adherent to the wound and easy to remove after healing. h) Must provide debridement action to enhance leucocytes migration and support the accumulation of enzyme. i) Must be sterile, non-toxic and non-allergic [222].

To practically compare the available dressings at the market, we set six measurable features listed below:

1- How long the wound takes to heal
2- The efficiency in protecting the wound from bacterial infection and how frequent the dressing should be changed
3- The ability to protect the wound from the resistant bacteria
4- Any toxicities or allergies to the patient
5- How easy it can be applied on the wound
6- The price

Tables 6.3 to 6.10 compare eight known brands of antimicrobial wound dressings. The comparison includes the advantages, the disadvantages, the efficiency, the toxicity and the price of each product. This information was taken from commercial websites and the safety datasheets of the products.

Types	Brand Name	Manufacturer
Bacterial Binding	Actisorb	KCI - An Acelity Company
	Bioguard	Derma Sciences, Inc.
	Cutimed	BSN medical, Inc.
	KoCarbonAg	Equinox Medical, LLC
	Leukomed	BSN medical, Inc.
	RTD	Keneric Healthcare
	Sorbact	IHT
	Suprasorb	L&R USA, Inc.
	Zorflex	Calgon Carbon
Bacterial Trapping	Aquacel	ConvaTec
	RTD	Keneric Healthcare
	Suprasorb	L&R USA, Inc.
	Zorflex	Calgon Carbon
Bactericidal	Iodofoam	Progressive Wound Care Technologies
	Promogran Prisma	KCI - An Acelity Company
	Silvercel	KCI - An Acelity Company
	Acticoat	Smith & Nephew, Inc.
	Actisorb	KCI - An Acelity Company
	Algicell	Derma Sciences, Inc.
	Allevyn	Smith & Nephew, Inc.
	Anaspet	Anacapa Technologies, Inc.
	Aquacel	ConvaTec
Bacteriostatic	Dextrosan	MPP Group LLC
	Aquacel	ConvaTec
	Curity	Medtronic
	Excilon	Medtronic
	Kendall	Medtronic
	Kerlix	Medtronic
	Simpurity	Safe n' Simple
	Suprasorb	L&R USA, Inc.
Fungicidal	Anaspet	Anacapa Technologies, Inc.
Microbicidal	Sorbact	IHT
Sporicidal	Anaspet	Anacapa Technologies, Inc.
Virucidal	Anaspet	Anacapa Technologies, Inc.

Table 6.1: Wound dressings sorted based on their function

Types	Brand Name	Manufacturer
Honey Dressing	Actilite	Advancis Medical
	Activon	Advancis Medical
	Algivon	Advancis Medical
	Medihoney	Derma Sciences, Inc.
Silver Dressing	Tegagerm	3M Healthcare
	Aquacel	ConvaTec
	Safetac Mepilex	Molnlycke Healthcare Us LLC
	Polymem	Ferris
	Biopatch	Johnson & Johnson
	SilverIon	Argentum Medical
	InterDry AG	Coloplast Corp
	Durafiber AG	Smith & Nephew, Inc.
	Acticoat	Smith & Nephew, Inc.
	Algicell	Derma Sciences, Inc.
	Algisite	Smith & Nephew, Inc.
	Askina	B.Braun Hospicare Ltd.
	Promogran Prisma	KCI - An Acelity Company
Iodine dressing	Inadine	Johnson & Johnson Medical Ltd
	Iodoflex	Smith & Nephew, Inc.
	Povitulle	CD Medical
Activated carbon cloth	Zorflex	Calgon Carbon
Chlorhexidine	Bactigras	Smith & Nephew, Inc.
Dialkylcarbamoyl chloride (DACC)	Cutimed	BSN medical, Inc.
Polyhexamethylene biguanide (PHMB)	ActivHeal	Advanced Medical Solutions
	CelluDress	Medicareplus International
	Excilon	Medtronic
	Kendall	Medtronic
	Kerlix	Medtronic

Table 6.2: Wound dressings based on types of active antimicrobial materials

Product 1	**Actilite**
Advantages	Manuka honey dressings have anti-bacterial properties. It also eliminates any odours. The combination of Manuka honey & Manuka oil has shown to be effective against major bacteria like MRSA, VRE, MSSA. The dressings are available in larger sizes, including 30x60cm. Shorter treatment periods with honey dressings are noticed as it can clear infections faster.
Disadvantages	Non-adhesive. Some people experience discomfort with honey dressings. Can be ineffective if not applied properly, as not enough honey comes into contact with the wound.
Length of effectiveness	Unspecified. Single use only. Honey dressings overall are usually changed once a day, though with heavily infected wounds, up to 3x per day may be appropriate.
Pricing	[$ 2.6/100 cm^2]
Toxicity profile	Monitor patients with diabetes. Do not use on patients who are allergic to bee venom.
Type of textile carrier	Light viscose net dressing

Table 6.3: Actilite wound dressing details including advantages, disadvantages, effectiveness, toxicity profile, price and type of carrier used.

Product 2	**Medihoney**
Advantages	"Comes in both adhesive and non-adhesive varieties. Uses 63% Maukua honey in a hydrogel dressing. Promotes removal of necrotic tissue, so appropriate for patients with advanced wounds. Good for light to moderately exuding wounds. Ideal for diabetes patients. Adhesive version does not require secondary dressing."
Disadvantages	Less economic
Length of effectiveness	Unspecified. Frequency of change determined by medical provider.
Pricing	[$ 89/100 cm^2]
Toxicity profile	Not appropriate for 3rd degree burns or those with allergy to honey, algae or seaweed.
Type of textile carrier	Super Absorbent Polymer

Table 6.4: Medihoney wound dressing details including advantages, disadvantages, effectiveness, toxicity profile, price and type of carrier used.

Product 3	**Aquacel**
Advantages	"Extra strong and extra absorbant. Lasts longer than other dressing with a controlled, slow release of ionic silver yet absorbing wound exudate at the same time. Offers adhesive and non-adhesive varieties. Comes in both ribbons and pads for all types of wounds."
Disadvantages	Some associated toxicity
Length of effectiveness	14 days
Pricing	[$ 69.5/ 100 cm^2]
Toxicity profile	No known contraidications, but not ideal for very dry wounds or those covered in black, necrotic tissue. Obviously not for use on patients allergic to the dressing's components.
Type of textile carrier	"Hydrofiber™ Technology is a soft, absorbent material that transforms into a gel on contact with wound fluid"

Table 6.5: Aquacel wound dressing details including advantages, disadvantages, effectiveness, toxicity profile, price and type of carrier used.

Product 4	**Inadine**
Advantages	"Color changes when ready to change. Non-adhesive imbedded with 10% povidone-iodine. Effective against bacteria, viruses, funghi and protezoa. "
Disadvantages	Iodine dressings come with many contraindications.
Length of effectiveness	Likely not to contain antimicrobial activity longer than 2 days. Some wounds might need changing daily or more often depending on exubance.
Pricing	[$30.7/100 cm^2]
Toxicity profile	Should not be used where there is a known iodine hypersensitivity; before and after the use of radio-iodine (until permanent healing); if the patient is being treated for kidney problems, is pregnant or breastfeeding; in cases of Duhring's herpetiform dermatitis (a rare skin disease). Must be used under medical supervision: in patients with any thyroid diseases; in newborn babies and infants up to the age of 6 months as povidone-iodine may be absorbed through unbroken skin; when treating deep ulcerative wounds, burns or large injuries.
Type of textile carrier	Knitted viscose fabric

Table 6.6: Inadine wound dressing details including advantages, disadvantages, effectiveness, toxicity profile, price and type of carrier used.

Product 5	**InterDry AG**
Advantages	"Provides moisture management to skin. Prevent and manage intertrigo (where skin touches skin creating moisture and friction that causes, redness, itching, burning, odour and/or maceration) in skin fold areas(ie: groin, abdomen, axilla, toes, fingers, buttock). May be used under compression wraps, braces or splints as well. "
Disadvantages	Not used on wounds.
Length of effectiveness	Up to 5 days
Pricing	[$ 11/100 cm^2]
Toxicity profile	Some patients might have sensitivity or allergy to silver
Type of textile carrier	Knitted polyester textile impregnated with silver.

Table 6.7: InterDry AG wound dressing details including advantages, disadvantages, effectiveness, toxicity profile, price and type of carrier used.

Product 6	**Iodoflex**
Advantages	Changes color to indicate when ready to change. Biodegradable. Highly absorbant, deslougher, range of antimicrobial action. Odor control.
Disadvantages	Iodine dressings come with many contraidications. More expensive than other iodine offerings as
Length of effectiveness	Effective for around 1/3 a week.
Pricing	[$ 9.1/100 cm^2]
Toxicity profile	Iodine is absorbed systemically especially when applied to large wounds and therefore Iodoflex should be used with care on patients who have a history of thyroid disorders. Iodoflex should not be used on children and as iodine can cross the placental barrier and is secreted into milk Iodoflex should not be applied to pregnant women or lactating mothers. There is a potential interaction of iodine with lithium and therefore co-administration is not recommended. Iodoflex should not be used concomitantly with mercurial antiseptics, e.g. mercurochrome and thiomersal, or taurolidine. A single application should not exceed 50 grams and not more than 150 grams of Iodoflex should be applied during the course of one week. A single course of treatment with Iodoflex should not exceed 3 months. Iodoflex should not be used on dry wounds.
Type of textile carrier	Gauze fabric

Table 6.8: Iodoflex wound dressing details including advantages, disadvantages, effectiveness, toxicity profile, price and type of carrier used.

Product 7	**Durafiber**
Advantages	"Effective against infection. High integral wet strength allowing easy one piece removal. Allows fluid retention under compression and minimises lateral wicking of fluid, thus reducing the potential for maceration of peri-wound skin.Provides broad spectrum antimicrobial activity at 4 hours against pathogens"
Disadvantages	Not to use on infected wounds.
Length of effectiveness	7 days
Pricing	[$ 71.5/100 cm^2]
Toxicity profile	Not intended to be used as a surgical sponge in heavily bleeding wounds, Not compatible with oil-based products such as petrolatum.
Type of textile carrier	Absorbent, non-woven silver containing antimicrobial dressing composed of cellulose ethyl sulphonate fibers.

Table 6.9: Durafiber wound dressing details including advantages, disadvantages, effectiveness, toxicity profile, price and type of carrier used.

Product 8	**Celludress – PHMB**
Advantages	Can be used at different stages of healing to promote granulation, while providing antimicrobial protection and effective exudate management. It can also be used under compression.
Disadvantages	Can't be used where bone tissue is exposed, where there is cartilage damage or there is known hypersensitivity to one of the ingredients
Length of effectiveness	Not specified but shouldn't be left for more than 3 days. Daily change is recommended for PHMB dressings.
Pricing	[$ 5.9/100 cm^2]
Toxicity profile	Should not be used for clients with known sensitivity or allergy to PHMB.
Type of textile carrier	Non-woven polyester/viscose fleece impregnated with PHMB.

Table 6.10: Celludress – PHMB wound dressing details including advantages, disadvantages, effectiveness, toxicity profile, price and type of carrier used.

6.2.4 The Main Players

There are many companies operating in the antimicrobial dressings market. The top ones include 3M Healthcare, Medtronic Plc, Smith & Nephew Plc, Medline Industries, Inc., ConvaTec, Inc., Organogenesis, Inc., Molnlycke Health Care AB, Paul Hartmann AG, Urgo Medical, Derma Sciences and Inc. J & J.

6.2.5 The Gap in the Market

Based on the market study, the gap in the market is defined from the six measurable features mentioned in the previous section. The data shows that there are contradictory reports about the efficiency of the available products. Based on conducted clinical studies for the available products, there are claims confirming the ability of the dressings to accelerate wound healing and other suggesting the ability to prevent bacterial infection. Silver dressings toxicity was reported [223, 224] and the ability to accelerate wound healing was doubted [225].

Surgeons who were consulted for this study advised that the most effective dressings available in the market can only be left on the wound for a maximum of three days and usually have to be changed daily. Their replacement causes pain and discomfort to the patient. Finally, the relatively high price of the current products accompanied with the low efficiency makes wounds treatment expensive. The Telegraph newspaper reported in 2010 that millions of pounds are being wasted by the NHS on wound dressings that contain silver amid doubts over their effectiveness.

6.3 The Product (AMP-based Wound Dressings)

For a new developed product to have a potential in the market, it has to provide an added value over the available ones. The more added values are provided, the more appealing the product will be for the market. We are proposing new antimicrobial dressings which fill a current gap in the market. The products are developed using AMPs as active agents to protect wounds from bacterial infections.

Similar to the available products, the new ones are going to be developed to suit different wounds types and sizes. There will be adhesive and non-adhesive dressings made by different textile carriers (woven or unwoven). In additions, many sizes of each product will be available with some special ones designed to cover tricky areas of the human body.

Although it has to be demonstrated during the development that these products will have added values over the current products. First, they are expected to be able to protect wounds from the resistant bacteria. In addition, the dressings will be more efficient as we expect them to last on the wound a 30 to 50 % longer comparing with the silver dressings with no

associated toxicity. Finally, our products will be more cost effective solution for wound management.

6.3.1 Unique Value Propositions (UVP)

The points below summarise the UVPs of the products

1- No toxicity.
2- Effective against the resistant bacteria.
3- The dressings last 30% longer on the wound than the usual dressings which is less pain to the patient.
4- Cost effective wound management.
5- Products are available at different shapes and sizes.
6- Different textile types to suit many types of wounds.

6.4 Product Development

The proposed products are going to be developed in three parts: The development of AMPs, the development of the textile carriers and the dressings design and finally the development of the coating technology (applying the AMPs on the textile carrier).

6.4.1 Translation Cycle

According to classic medicinal products, the development is expected to pass through clinical study, regulatory assessment and process validation before sale and distribution. The current state of the dressing development is in the proof of concept, figure 6.1. The transitional steps for antimicrobial dressings is expected as for topical and cosmetics applications and not as a drug. This makes the development quicker and less subject to intense safety regulations.

6.4.2 Basic Discovery and Proof of Concept

The product idea has immerged from the successful "*in vitro*" results of AMPs as explained in chapters 3, 4 and 5. These results show principle of antimicrobial active materials we intend to use in our dressings products. However, the effect of such peptides was not tested while they are incorporated within the dressing materials. Thus, in this stage we have to assess *in vitro* the efficiency of antimicrobial dressing using an AMP model.

6.4.3 Preclinical Development

The focus of preclinical testing is to assess whether the dressing product is safe for human volunteers and whether it exhibits pharmacological activity to merit further investigation. Such investigations could be *in vitro* and *in vivo* studies. Usually, preclinical studies are not

very large. However, these studies must provide detailed information on dosing and toxicity levels. If the investigation meets the criteria, the company files an investigational new product application with the FDA/EMA to pursue clinical testing on humans. We could also initiate patent fillings at this stage.

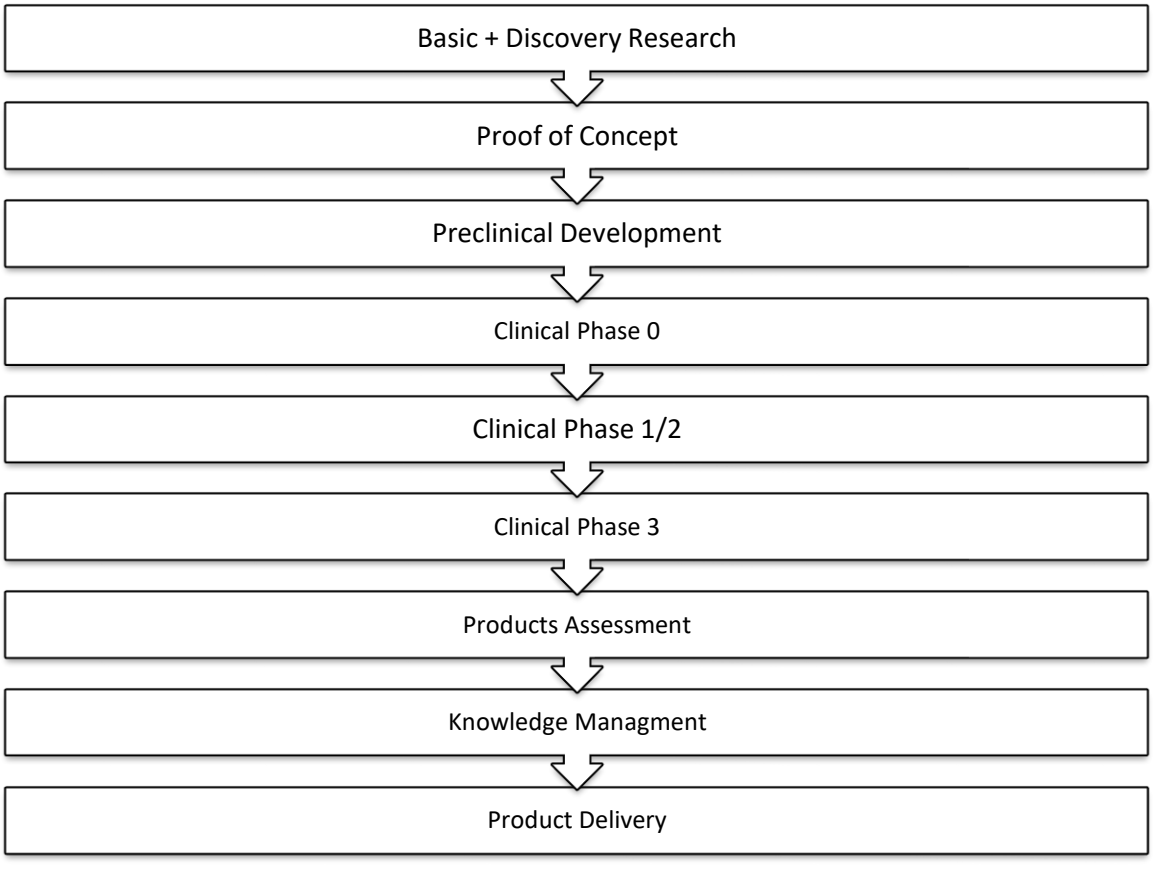

Figure 6.1: Expected development stages for drugs or medical devices.

6.4.4 Clinical Testing in Human Volunteers

Potential new drugs must undergo extensive study in human volunteers in order to demonstrate safety and efficacy to the regularity bodies. Clinical trials comprise the most lengthy and costly portion of the R&D process. The clinical trials process occurs in several phases and takes many years. However, for the topical cosmetic applications, clinical trials are significantly quicker and should cost less than a typical drug. Biopharmaceutical industry sponsored clinical trials are conducted around the country and in a variety of settings, including academic medical centres, dedicated clinical trial testing centres, and physician offices.

From enrolment to completion, these trials take many years to complete and can cost millions of pounds. These randomized, controlled trials generate large amounts of data to support submission to the regulatory bodies for approval.

Clinical trials are viewed in several distinct phases as outlined below:

Phase I clinical trials typically are conducted with a small number of healthy volunteers, typically less than 100, to determine the safety, tolerability, and pharmacokinetics and pharmacodynamics of the wound dressing (i.e., researchers assess how the dressing behaves on the body and relationship between its components' molecular structure and their effects on volunteers).

Phase II clinical trials begin if the drug successfully passes Phase I testing. This phase generally involves between 100 and 500 human volunteers to assess the efficacy and dose response of the investigational dressing in development, including identification of common, short-term potential side effects.

Phase III clinical trials are initiated if the potential new dressing is found to be both safe and efficacious through Phases I and II testing. Phase III trials may enrol 1,000 to 5,000 patients or more across numerous clinical trials sites across the country and around the world.

6.4.5 Product Assessment

This involves the assessment of the products by surgeons. The assessment aim to analyse feedbacks from surgeons and practitioners about the product design, packaging and how easy it is to use under the clinic conditions. It also aims to assess the best storage conditions of the products.

6.4.6 Knowledge Management

For the dressing products, knowledge management includes: standardized manufacturing process and clinical practice guidelines.

6.4.7 Healthcare Delivery

Health care delivery system for the wound dressings includes educational and training sessions for surgeons and practitioners if necessary. It also involves finding the right distribution channels for the products to reach the target hospitals, clinics and the related industries.

6.5 Manufacturing and Operation

6.5.1 Peptides Production

Peptides production can be done via contract manufacturing with companies specialised in this industry. We evaluate such partnership based on three principles; first, the quality of the

peptides produced in a form of powder or concentrated liquid, second, the company reliability and quality consistency, and finally the price.

Generally, peptides could be either produced chemically or via recombinant methods. Although each of these production methods has its advantages, it does not matter as long as the final product meets the criteria. Hence the choice will be based on the added value provided by either of these two manufacturing methods whether a cheaper price or a better quality.

6.5.2 Textile Carriers Production

Wound dressings are manufactured using different textile materials. The dressing can be as simple as a strip of plain textile, or as complex as an engineered composite that contains layers of different geometries and reactive materials, including medicines. A number of polymeric materials are used as films, fibres and other structures for developing wound-dressing products. Some of the primary materials employed are cotton, rayon, polyester, nylon, polyolefins, acrylic, polyurethan, chitosan and alginate. The textile made by such fibres could be woven and non-woven and both have application in wound dressings [226]. As explained in competitive landscape section, textiles used to produce wound dressings have to meet specific criteria in order to do the job.

Similar to peptide production, textile production can also be outsourced via a contract manufacturing. Textile manufacturing companies can produce according to our specific requirements. However, textile carriers could also be produced in house within an integrated production line including the AMPs coating stage. This will save time and cost as well as maintain a protected manufacturing environment needed for medical dressings.

6.5.3 Coating Process and Packaging

Textile coating is the process of absorbing materials onto the textile. Whether it is chemical or pharmaceutical nano or micro-material, the suitable coating technology should be applied based on the textile nature and coating material. The suitable technology should be efficient in absorbing the material that could be expensive such as AMPs. In fact, AMPs coating onto textile has been reported but not yet commercially invested [227]. AMPs coating technology can of course be developed in labs and then scaled up for industry.

6.6 Sales and Marketing Strategy

6.6.1 Who Are the Customers

Wound dressings are distributed and sold globally. With the rise of antimicrobial resistance, a new technology employing AMPs to protect wounds from resistant pathogens will be of interest to hospitals and clinics all over the world. For a start-up company however, it is usually difficult to set sales and marketing plans to cover the global market. In fact, we aim here to specify the sales channels in the UK and how to reach them and supply them. This plan could be replicated in each country and performed either directly by the manufacturing company or, more practically, via exclusive agents.

Hospitals and surgical clinics consume the majority of the antimicrobial dressings. According to the National Health Services (NHS) data, there are in England: 209 clinical commissioning groups, 135 acute non-specialist trusts, 17 acute specialist trusts, 54 mental health trusts, 35 community providers, 10 ambulance trusts, 7,454 GP practices, 853 for-profit and not-for-profit independent sector organisations. Although not all these health care providers consume antimicrobial dressings, it is necessary to gradually educate all of them about the new products. This will make the product widely known and acceptable within the industry.

Usually when a new product is launched, hospitals trustees are invited to a sponsored lunch to include products pitching. Such events are organised to show the advantages of the new products comparing with the existing ones. In fact, with the recent cut of the NHS funding, trustees are looking for cheaper alternatives especially for consumables. If proven to be overall a cheaper wound management option, AMPs based dressings will be attractive products for NHS hospitals. Negotiations with hospitals trustees take long time and might be mediated by brokers who understand their need and could have direct connections with the decisions makers. These events for pitching the new products can be performed not only for UK NHS hospitals but also for private sector hospitals which usually are more fixable in making decisions to stock new products.

In addition to selling to hospitals, wound dressings can be sold directly to pharmacies and healthcare shops. These could be reached via healthcare distribution companies.

Building a brand name is not an easy job for start-up companies. In order to do so, conferences and exhibitions that are related to the industry have to be attended. The trust for the company and the new products can be gradually built by exposing them to surgeons, nurses and practitioners who apply such dressings to the patients.

6.7 Financial Model

6.7.1 Estimated Costs for Products Development

The cost of each stage along the development is estimated and presented in the table below in thousands (£ 1000).

Development Stage	Expected Duration (Months)	Cost
Proof of concept	3	£ 100
Preclinical	6	£ 200
Clinical phase 1/2	9	£ 500
Clinical Phase 3	9	£ 500
Product Assessment	6	£ 50
Knowledge Management	3	£ 10
Total	36 months	£ 1,360

Table 6.11: Expected time and cost in thousands (X £1000) for each stage of the products development

6.7.2 Gross Profit Margin

The calculations of the products net costs are very difficult at this stage as they are not fully developed yet. Thus the precise calculation of the profit margin is not possible. However according to the market study, medical dressings producers expect a gross profit margin of 50 -70%. Hence, we assume that the minimum gross profit margin for our products is 50%.

6.7.3 Sales Assumptions

We assume that the sale will increase gradually each month till reaching in sales 20 % of the antimicrobial dressing market in the UK by the end of the third year. The amount of estimated sales is divided equally over 5 products. The table below shows the revenue presented in thousands (£1000) generated from each product each year and the estimated gross profit.

Year / Product	2021	2022	2023
Product 1	£780	£2,220	£3,660
Product 2	£780	£2,220	£3,660
Product 3	£780	£2,220	£3,660
Product 4	£780	£2,220	£3,660
Product 5	£780	£2,220	£3,660
Total sales (revenue)	£3,900	£11,100	£18,300
Total gross Profit (50%)	£1,950	£5,550	£9,150

Table 6.12: Sales assumptions and revenue in thousands (X £1000) over three years 2021-2023

6.7.4 Estimated Operational Cost & Overheads

The table below shows the overhead costs estimated presented in thousands (£ 1000). We assume that peptide production and all the logistics and delivery forces are out-sourced.

	2021	2022	2023
Total Salaries (Incl NI)	£250	£375	£500
Manufacturing site rent	£25	£70	£90
Marketing	£200	£300	£400
Heat & Light	£10	£20	£25
Travel	£50	£75	£10
Accounting	£2	£4	£6
Annual Other Misc Costs	£10	£15	£20
Quality Control	£100	£150	£200
R&D	£200	£400	£600
# Employees at Year End	10	15	20
Average Salary	£25	£25	£25

Table 6.13: Estimated operational costs in thousands (X £ 1000) and overheads over 3 years 2021-2023

6.7.5 Capital Equipment:

The company must purchase a production line to include machinery items for the two production stages; textile production and peptide coating. In addition, offices equipment and hardware items are needed for the management staff. The cost of these are estimated in the table below presented in thousands (£ 1000).

Machinery and equipment Purchase	£1,000
Computer Hardware	£34
Depreciation Period (Years)	5

6.7.6 Three Year Profit and Loss Estimated Account

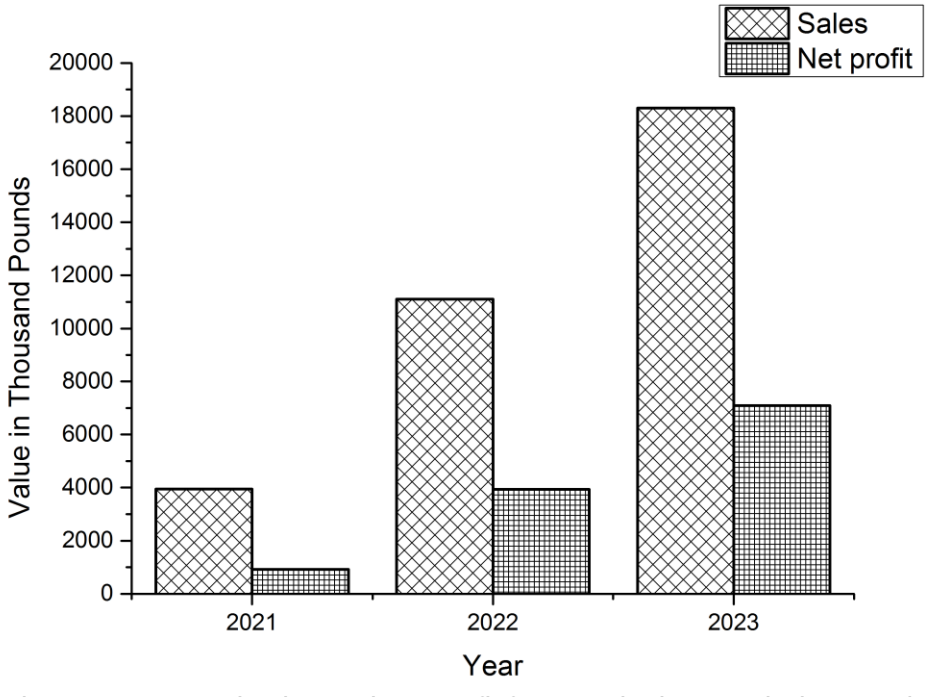

Figure 6.2: Annual sales and net profit forecast in thousands (x £1000)

6.7.7 Three Year Cash Flow Forecast

This cash flow account starts by January 2021 when the production starts. It does not include all the money invested for the products developments in the first 3 years.

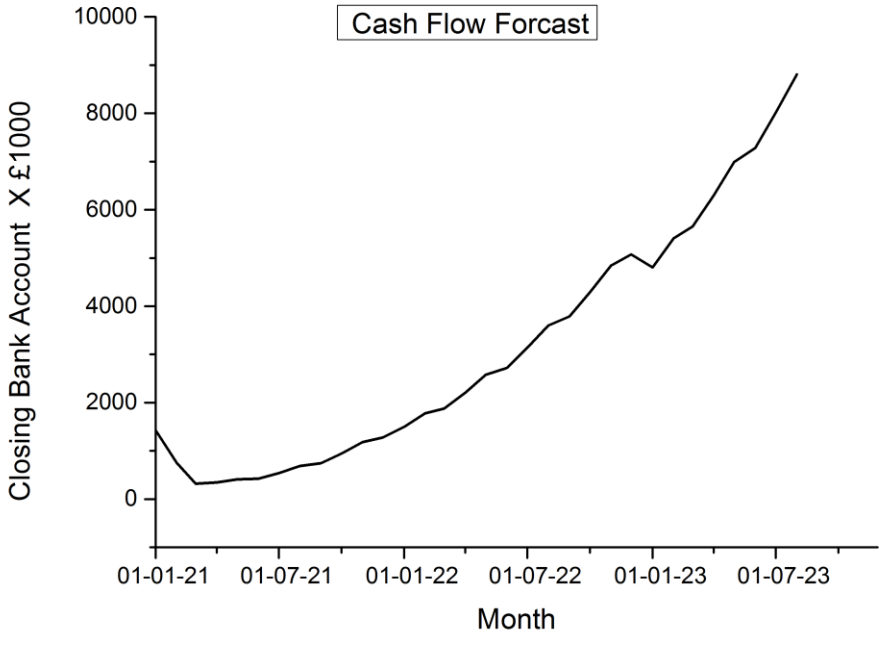

Figure 6.3: Cashflow forecast for three years in thousands (x £1000)

6.7.8 Investment Requirements

Year Start	**2018**	**2019**	**2020**	**2021**	**Total**
Amount x £ 1000	£ 500	£ 860	£ 500	£ 1,000	£ 2,860

Table 6.14: Estimated investment required over 4 years 2018-2021

6.7.9 Estimated Payback Time

Based on the financial study, the payback time of all the investment (2,860 K) is estimated to be after four and a half years. This includes the 3 years period spent on the product development.

6.8 SWOT Analysis

Strengths

- Novel technology, no competition
- Long term development is possible
- Very big global market
- Gradual investment over the development
- Easy and available exits strategy in each development stage
- No negative effects
- Large scale production is possible

Weakness

- New technology, could face unexpected problems
- Clinical trials could show the need for further optimisations
- High cost of peptide production
- Peptides stability could be an issue
- The difficulty to patent peptides sequence as they easily can be copied with little modifications

Opportunities

- Ability to open new applications using the same AMPs
- The ability to licensing the use of the peptide for other industries

Threats

- Competition from other companies
- Clinical trials not approved
- Bacteria acquire resistance against peptides

6.9 Exit Strategies

There are ways for investors to exit this investment. This could happen at the end of this plan, i.e., by the end of 2023 or it could happen after any stage of the development. Each stage of the products development is a milestone and if was done successfully, it will be an added value to the project which will be translated into a rise in the shares price.

For example, the evaluation of the company after passing the phase 1 of clinical trials is certainly higher than that before passing it. This means that the investors will most likely get their money back if not making any profit.

Potential new investors in this company will be all the big companies performing in the wound management sector. In addition, this innovative company could be made as a public company. This will give the opportunity for everybody to invest in the company especially as it could be looked at as one of the future solutions for the antimicrobial resistance

6.10 Risk Register

Every business has a risk and usually the amount of risk is proportion to the expected outcome of the business. Start-up businesses, for example, are usually risker than older running businesses. This is why investors expect a higher return when investing in a start up company comparing with investing in an old structured company.

However, studying the potential risks, minimising it and having contingency plans is very recommended for entrepreneur to be included in the business plan to be more sound to investors.

Appendix 2 shows a list of potential risks associated with this business highlighted as low (L), medium (M) and high (H). There are three high risk items within the list. First, a regulatory issue of not approving the products as safe to be marketed. This off course could be as a result of unexpected toxicity or allergy reactions during the clinical trials. This risk can't be completely eliminated, however, going through the gradual development cycle, such reactions will appear much earlier and before investing in clinical trials. In addition, the screening process during clinical trial is very important to carefully being set to exclude those who have high potential to react to peptide treatment.

Second, the potential of having unforeseen cost. This is very common when it comes to study costs well in advance of actually starting the project. In order to minimise this, the study has already included 20% extra costs in order to have enough margin for such expenses.

Finally, as this is a cutting edge innovative company, it is always of a worry for entrepreneur to lose his experienced staff. This could happen either when another company hunted them in better positions, or staff can find it possible to spin off again to found their own company. This problem can always be accommodated with strong leadership. When the experienced staff are engaged enough in the project, i.e. have shares in the company and feeling the businesses as it their own, then they won't think of fleeing.

6.11 Conclusion

In conclusion, this chapter has demonstrated a plan for a spin off business based on the antimicrobial peptide technology. As the idea has a lower risk comparing with developing drugs and promises a stable market, investors could find it attractive. Although the investment involves research and development, which is considered risky, it actually was segmented into parts to minimise this risk. In addition, the business can fit under the government's priorities and concerns which facilitate funds and incentives. Finally, the

success in this emerging product will open the doors to many other products using the same peptide technology with massive market opportunity across the world.

Chapter 7

Conclusion

In a conclusion, the work in this thesis has contributed to elucidating membrane attack mechanism employed by antimicrobial peptides (AMPs), with the long-term potential to address the global challenge of increasing antimicrobial resistance. Much previous work was done on characterising and understanding the mechanisms of these natural powerful agents. However, we *de novo* designed new peptides and tested their antimicrobial properties and mechanism of actions. The atomic force microscopy (AFM) data in this thesis have enabled us to better understand structure-function relationships, with the possibility of controlling and changing these structures for optimum antibacterial results.

In particular, four *de novo* AMPs have been compared in terms of structure, biological activities and the proposed antibacterial mechanisms to kill bacteria. As these peptides were meant to kill bacteria via interacting with the bacterial membrane followed by poration or/and disruption its intactness, atomic force microscopy (AFM) was a tool to image this process as it happens.

All the methods employed and used in this study were explained in the chapter 2. This includes peptides synthesis, sample preparations and AFM operations.

In chapter 3, two helical peptides were compared to conclude that a change in the amino acid cationic residues has led to a change in the membrane disruption mechanism. A substitution of six cationic amino acids, lysine (K) to arginine (R), led to a change from perpendicular spanning of the helices to form expanding pores within the bacterial membrane into, instead, a tilted orientation to form shallower static pores.

In chapter 4, a *de novo* triskelion with three arms of antimicrobial β-sheet peptide motifs inspired from the breast-milk protein (lactoferrin) was explained. The design was meant to co-assemble to form hollow antimicrobial capsules that can act as vehicles for gene delivery with bactericidal properties. Time-lapse AFM was used to image the capsules while attacking the membrane. The results showed that capsules descended in the membrane followed by the disassembly to form static pores on their precise landing positions.

In chapter 5, another *de novo* peptides design was explained. Two peptide monomers were devised to co-assemble and form antimicrobial hollow capsids inspired by the natural viral capsids. One monomer is a triskelion with three arms of helical cationic antimicrobial peptide motifs. The other is anionic non-antimicrobial helical peptide designed to interact with the

positive one and facilitate the co-assembly. Time-lapse AFM showed that this system attacks bacterial membranes and disassemble in a much quicker time-span compared with the capsule system explained in chapter 4. The disassembled cationic monomers were shown to disrupt the bacterial membrane via expanding pores until a complete removal.

These AMPs hold a promise to be feasibly transferred towards medical applications. Some of these applications were explained in chapter 6 with a complete business plan for antimicrobial wound dressings as a potential application of the AMPs studied within the framework of this thesis.

However, medical products including drugs have to go through lengthy and costly regulatory investigations to demonstrate their safety and suitability for humans. Although the concept of synthetically produced antimicrobial peptides has been sufficiently demonstrated, additional work on the same peptides could help to gain further understanding and to facilitate the path to medical applications. For example, the methods of AFM imaging can be improved to enable imaging the attacking mechanism on live bacteria instead of model membranes. In addition, to confirm the non-cytotoxicity probed by the other employed techniques, AFM can be used to image mammalian cell membranes as a negative control. Furthermore, improving the resolution of imaging and sample preparations could enable resolving the fine details of the assembly for the capsules and capsids explained in chapter 4&5 respectively.

Yet, these demonstrated *in vitro* experiments as a proof of concept are only the first step for moving towards commercial application. Further *in vivo* validation would involve testing the AMPs on animals, followed by extensive clinical testing on human volunteers to demonstrate the safety and efficacy to the regularity bodies.

References

1. Leung, C., et al., *Atomic Force Microscopy with Nanoscale Cantilevers Resolves Different Structural Conformations of the DNA Double Helix.* Nano Letters, 2012. **12**(7): p. 3846-3850.
2. Castelletto, V., et al., *Structurally plastic peptide capsules for synthetic antimicrobial viruses.* Chemical Science, 2016. **7**(3): p. 1707-1711.
3. Pyne, A.L.B., *High Resolution Atomic Force Microscopy of Functional Biological Molecules*, in *London Centre for Nanotechnology*. 2015, University College London.
4. Powers, J.-P.S. and R.E. Hancock, *The relationship between peptide structure and antibacterial activity.* Peptides, 2003. **24**(11): p. 1681-1691.
5. Bella, A., *Synthetic Disintegrins as Mediators of Cell-Matrix Interactions: Implication for Cancer and Regenerative Therapies*, in *Department of Chemistry*. 2011, University of Leicester: UK.
6. Allen, H.K., et al., *Call of the wild: antibiotic resistance genes in natural environments.* Nature Reviews Microbiology, 2010. **8**(4): p. 251-259.
7. Han, S.-Y. and Y.-A. Kim, *Recent development of peptide coupling reagents in organic synthesis.* Tetrahedron, 2004. **60**(11): p. 2447-2467.
8. Li, C., et al., *Computational characterization of parallel dimeric and trimeric coiled-coils using effective amino acid indices.* Molecular BioSystems, 2015. **11**(2): p. 354-360.
9. Lee, T.-K., et al., *Preparation of MBHA resin by benzotriazole-mediated amidoalkylation.* Tetrahedron Letters, 2008. **49**(37): p. 5380-5382.
10. Li, A., et al., *Atomic force microscopy study of the antimicrobial action of Sushi peptides on Gram negative bacteria.* Biochimica et Biophysica Acta (BBA)-Biomembranes, 2007. **1768**(3): p. 411-418.
11. Binnig, G., C.F. Quate, and C. Gerber, *ATOMIC FORCE MICROSCOPE.* Physical Review Letters, 1986. **56**(9): p. 930-933.
12. Fantner, G.E., et al., *Kinetics of antimicrobial peptide activity measured on individual bacterial cells using high-speed atomic force microscopy.* Nature nanotechnology, 2010. **5**(4): p. 280-285.
13. Ouberai, M., et al., *The Pseudomonas aeruginosa membranes: A target for a new amphiphilic aminoglycoside derivative?* Biochimica et Biophysica Acta (BBA)-Biomembranes, 2011. **1808**(6): p. 1716-1727.
14. Peters, B.M., M.E. Shirtliff, and M.A. Jabra-Rizk, *Antimicrobial Peptides: Primeval Molecules or Future Drugs?* Plos Pathogens, 2010. **6**(10).
15. Su, C., et al., *Quantitative Mechanical Mapping of Biomolecules in Fluid.* MRS Proceedings, 2011. **1261**.
16. Alves, C.S., et al., *Escherichia coli cell surface perturbation and disruption induced by antimicrobial peptides BP100 and pepR.* Journal of Biological Chemistry, 2010. **285**(36): p. 27536-27544.
17. Santis, E., et al., *Antimicrobial peptide capsids of de novo design.* Nature communications, 2017. **8**(1): p. 2263.
18. Oshaben, K.M., et al., *The native GCN4 leucine-zipper domain does not uniquely specify a dimeric oligomerization state.* Biochemistry, 2012. **51**(47): p. 9581-91.
19. Day, C.L., et al., *STRUCTURE OF THE RECOMBINANT N-TERMINAL LOBE OF HUMAN LACTOFERRIN AT 2.0-ANGSTROM RESOLUTION.* Journal of Molecular Biology, 1993. **232**(4): p. 1084-1100.
20. Hwang, P.M., et al., *Three-dimensional solution structure of lactoferricin B, an antimicrobial peptide derived from bovine lactoferrin.* Biochemistry, 1998. **37**(12): p. 4288-98.

21. O'Shea, E.K., et al., *X-ray structure of the GCN4 leucine zipper, a two-stranded, parallel coiled coil.* Science, 1991. **254**(5031): p. 539-44.
22. Pyne, A., et al., *Engineering monolayer poration for rapid exfoliation of microbial membranes.* Chemical Science , 8 (2) pp. 1105-1115. (2017), 2017.
23. Grayson, M.L., et al., *The evolving threat of antimicrobial resistance Introduction*

The Evolving Threat of Antimicrobial Resistance : Options for Action. 2012. 2-+.
24. World Health Organization, W.H. *Antimicrobial resistance*. 2015 [cited 2015; Available from: http://www.who.int/mediacentre/factsheets/fs194/en/.
25. world Health Organization, W.H., *Antimicrobial resistance global report on surveillance*. 2014.
26. Cansizoglu, M.F. and E. Toprak, *Fighting against evolution of antibiotic resistance by utilizing evolvable antimicrobial drugs.* Current Genetics, 2017. **63**(6): p. 973-976.
27. Projan, S.J. and P.A. Bradford, *Late stage antibacterial drugs in the clinical pipeline.* Current Opinion in Microbiology, 2007. **10**(5): p. 441-446.
28. Tillotson, G.S., *Antibiotic development: A victim of market forces?* Idrugs, 2008. **11**(5): p. 340-345.
29. Projan, S.J. and D.M. Shlaes, *Antibacterial drug discovery: is it all downhill from here?* Clinical Microbiology and Infection, 2004. **10**: p. 18-22.
30. Moellering, R.C., *Discovering new antimicrobial agents.* International Journal of Antimicrobial Agents, 2011. **37**(1): p. 2-9.
31. Schloss, P.D. and J. Handelsman, *Status of the microbial census.* Microbiology and Molecular Biology Reviews, 2004. **68**(4): p. 686-691.
32. Ray, J., *Ryan K. Sherris Medical Microbiology*. 2003, New York: McGraw-Hill Medical.
33. Porta, D., et al., *Structural and ultrastructural characterization of Symploca atlantica Gomont, strain PCC 8002 (Oscillatoriales, Cyanophyta, Cyanobacteria).* Algological Studies, 2003. **109**(1): p. 509-524.
34. Miao, J., et al., *Imaging whole Escherichia coli bacteria by using single-particle x-ray diffraction.* Proceedings of the National Academy of Sciences, 2003. **100**(1): p. 110-112.
35. Gram, C., *Ueber die isolirte Farbung der Schizomyceten in Schnitt-und Trockenpraparaten.* Fortschritte der Medicin, 1884. **2**: p. 185-189.
36. Silhavy, T.J., D. Kahne, and S. Walker, *The Bacterial Cell Envelope.* Cold Spring Harbor Perspectives in Biology, 2010. **2**(5): p. 16.
37. Glauert, A.M. and M.J. Thornley, *The topography of the bacterial cell wall.* Annual Reviews in Microbiology, 1969. **23**(1): p. 159-198.
38. Mitchell, P., *Approaches to the analysis of specific membrane transport.* Biological structure and function, 1961. **2**: p. 581-599.
39. Kamio, Y. and H. Nikaido, *Outer membrane of Salmonella typhimurium: accessibility of phospholipid head groups to phospholipase c and cyanogen bromide activated dextran in the external medium.* Biochemistry, 1976. **15**(12): p. 2561-2570.
40. Beveridge, T.J., *Structures of gram-negative cell walls and their derived membrane vesicles.* Journal of bacteriology, 1999. **181**(16): p. 4725-4733.
41. Hwang, P.M., et al., *Solution structure and dynamics of the outer membrane enzyme PagP by NMR.* Proceedings of the National Academy of Sciences, 2002. **99**(21): p. 13560-13565.
42. Nikaido, H., *Molecular basis of bacterial outer membrane permeability revisited.* Microbiology and molecular biology reviews, 2003. **67**(4): p. 593-656.
43. Vollmer, W., D. Blanot, and M.A. De Pedro, *Peptidoglycan structure and architecture.* FEMS microbiology reviews, 2008. **32**(2): p. 149-167.
44. Mullineaux, C.W., et al., *Diffusion of green fluorescent protein in three cell environments in Escherichia coli.* Journal of bacteriology, 2006. **188**(10): p. 3442-3448.
45. Oliver, J.D. and R.R. Colwell, *Extractable lipids of gram-negative marine bacteria: phospholipid composition.* Journal of bacteriology, 1973. **114**(3): p. 897-908.

46. Merchante, R., H.M. Pooley, and D. Karamata, *A periplasm in Bacillus subtilis.* Journal of bacteriology, 1995. **177**(21): p. 6176-6183.
47. Neuhaus, F.C. and J. Baddiley, *A continuum of anionic charge: structures and functions of D-alanyl-teichoic acids in gram-positive bacteria.* Microbiology and Molecular Biology Reviews, 2003. **67**(4): p. 686-723.
48. Dramsi, S., et al., *Covalent attachment of proteins to peptidoglycan.* FEMS microbiology reviews, 2008. **32**(2): p. 307-320.
49. Goldfine, H., *Lipids of Prokaryotes–Structure and Distribution*, in *Current Topics in Membranes and Transport*, F. Bronner and A. Kleinteller, Editors. 1982, Academic Press. p. 1-43.
50. Sievers, S., et al., *Changing the phospholipid composition of Staphylococcus aureus causes distinct changes in membrane proteome and membrane-sensory regulators.* PROTEOMICS, 2010. **10**(8): p. 1685-1693.
51. Qiao, Y., et al., *Highly dynamic biodegradable micelles capable of lysing Gram-positive and Gram-negative bacterial membrane.* Biomaterials, 2012. **33**(4): p. 1146-1153.
52. Beceiro, A., M. Tomás, and G. Bou, *Antimicrobial Resistance and Virulence: a Successful or Deleterious Association in the Bacterial World?* Clinical Microbiology Reviews, 2013. **26**(2): p. 185-230.
53. Wilson, J.W., et al., *Mechanisms of bacterial pathogenicity.* Postgraduate Medical Journal, 2002. **78**(918): p. 216-224.
54. Martínez, J.L. and F. Baquero, *Interactions among strategies associated with bacterial infection: pathogenicity, epidemicity, and antibiotic resistance.* Clinical microbiology reviews, 2002. **15**(4): p. 647-679.
55. Aminov, R.I., *A brief history of the antibiotic era: lessons learned and challenges for the future.* Frontiers in microbiology, 2010. **1**.
56. Walsh, C., *Antibiotics: actions, origins, resistance*. 2003: American Society for Microbiology (ASM).
57. Baltz, R.H., *Daptomycin: mechanisms of action and resistance, and biosynthetic engineering.* Current opinion in chemical biology, 2009. **13**(2): p. 144-151.
58. Kohanski, M.A., D.J. Dwyer, and J.J. Collins, *How antibiotics kill bacteria: from targets to networks.* Nature Reviews Microbiology, 2010. **8**(6): p. 423-435.
59. Baker-Austin, C., et al., *Co-selection of antibiotic and metal resistance.* Trends in microbiology, 2006. **14**(4): p. 176-182.
60. Guo, L., et al., *Lipid A acylation and bacterial resistance against vertebrate antimicrobial peptides.* Cell, 1998. **95**(2): p. 189-198.
61. Salyers, A.A., A. Gupta, and Y. Wang, *Human intestinal bacteria as reservoirs for antibiotic resistance genes.* Trends in microbiology, 2004. **12**(9): p. 412-416.
62. Czaplewski, L., et al., *Alternatives to antibiotics—a pipeline portfolio review.* The Lancet Infectious Diseases, 2016. **16**(2): p. 239-251.
63. Zasloff, M., *Antimicrobial peptides of multicellular organisms.* nature, 2002. **415**(6870): p. 389-395.
64. Mookherjee, N. and R. Hancock, *Cationic host defence peptides: innate immune regulatory peptides as a novel approach for treating infections.* Cellular and molecular life sciences, 2007. **64**(7-8): p. 922.
65. Hancock, R.E. and M.G. Scott, *The role of antimicrobial peptides in animal defenses.* Proceedings of the national Academy of Sciences, 2000. **97**(16): p. 8856-8861.
66. Wang, G., X. Li, and Z. Wang, *APD3: the antimicrobial peptide database as a tool for research and education.* Nucleic Acids Research, 2016. **44**(Database issue): p. D1087-D1093.
67. Jenssen, H., P. Hamill, and R.E. Hancock, *Peptide antimicrobial agents.* Clinical microbiology reviews, 2006. **19**(3): p. 491-511.
68. Phoenix, D.A., S.R. Dennison, and F. Harris, *Anionic antimicrobial peptides.* Antimicrobial Peptides, 2013: p. 83-113.

69. Huang, Y., J. Huang, and Y. Chen, *Alpha-helical cationic antimicrobial peptides: relationships of structure and function.* Protein & cell, 2010. **1**(2): p. 143-152.
70. Hancock, R.E.W. and H.G. Sahl, *Antimicrobial and host-defense peptides as new anti-infective therapeutic strategies.* Nature Biotechnology, 2006. **24**(12): p. 1551-1557.
71. Findlay, B., G.G. Zhanel, and F. Schweizer, *Cationic amphiphiles, a new generation of antimicrobials inspired by the natural antimicrobial peptide scaffold.* Antimicrobial Agents and Chemotherapy, 2010. **54**(10): p. 4049-4058.
72. Nguyen, L., E. Haney, and H. Vogel, *The expanding scope of antimicrobial peptide structures and their modes of action.* Trends in biotechnology, 2011. **29**(9): p. 464-472.
73. Avitabile, C., L.D. D'Andrea, and A. Romanelli, *Circular Dichroism studies on the interactions of antimicrobial peptides with bacterial cells.* 2014. **4**: p. 4293.
74. Bürck, J., et al., *Oriented circular dichroism: a method to characterize membrane-active peptides in oriented lipid bilayers.* Accounts of chemical research, 2016. **49**(2): p. 184-192.
75. Ennaceur, S.M., et al., *Peptide Adsorption to Lipid Bilayers: Slow Processes Revealed by Linear Dichroism Spectroscopy.* Biophysical Journal, 2009. **96**(4): p. 1399-1407.
76. Haney, E.F. and H.J. Vogel, *NMR of antimicrobial peptides.* Annual reports on NMR spectroscopy, 2009. **65**: p. 1-51.
77. Bhunia, A., et al., *NMR structure of pardaxin, a pore-forming antimicrobial peptide, in lipopolysaccharide micelles mechanism of outer membrane permeabilization.* Journal of biological chemistry, 2010. **285**(6): p. 3883-3895.
78. Fjell, C.D., et al., *Designing antimicrobial peptides: form follows function.* Nature reviews Drug discovery, 2012. **11**(1): p. 37-51.
79. Yang, L., et al., *Barrel-stave model or toroidal model? A case study on melittin pores.* Biophysical Journal, 2001. **81**(3): p. 1475-1485.
80. Wu, M., et al., *Mechanism of interaction of different classes of cationic antimicrobial peptides with planar bilayers and with the cytoplasmic membrane of Escherichia coli.* Biochemistry, 1999. **38**(22): p. 7235-7242.
81. Oren, Z. and Y. Shai, *Selective lysis of bacteria but not mammalian cells by diastereomers of melittin: structure− function study.* Biochemistry, 1997. **36**(7): p. 1826-1835.
82. Gennaro, R. and M. Zanetti, *Structural features and biological activities of the cathelicidin-derived antimicrobial peptides.* Peptide Science, 2000. **55**(1): p. 31-49.
83. Martin, N.I. and E. Breukink, *The expanding role of lipid II as a target for lantibiotics.* 2007.
84. Bierbaum, G. and H.-G. Sahl, *Induction of autolysis of staphylococci by the basic peptide antibiotics Pep 5 and nisin and their influence on the activity of autolytic enzymes.* Archives of microbiology, 1985. **141**(3): p. 249-254.
85. Brogden, K.A., *Antimicrobial peptides: Pore formers or metabolic inhibitors in bacteria?* Nature Reviews Microbiology, 2005. **3**(3): p. 238-250.
86. Haney, E.F., S.C. Mansour, and R.E.W. Hancock, *Antimicrobial Peptides: An Introduction*, in *Antimicrobial Peptides: Methods and Protocols*, P.R. Hansen, Editor. 2017, Springer New York: New York, NY. p. 3-22.
87. Mor, A., et al., *Isolation, amino acid sequence and synthesis of dermaseptin, a novel antimicrobial peptide of amphibian skin.* Biochemistry, 1991. **30**(36): p. 8824-8830.
88. Dürr, U.H., U. Sudheendra, and A. Ramamoorthy, *LL-37, the only human member of the cathelicidin family of antimicrobial peptides.* Biochimica et Biophysica Acta (BBA)-Biomembranes, 2006. **1758**(9): p. 1408-1425.
89. Sørensen, O.E., et al., *Human cathelicidin, hCAP-18, is processed to the antimicrobial peptide LL-37 by extracellular cleavage with proteinase 3.* Blood, 2001. **97**(12): p. 3951-3959.
90. Behrendt, R., P. White, and J. Offer, *Advances in Fmoc solid-phase peptide synthesis.* Journal of Peptide Science, 2016. **22**(1): p. 4-27.
91. Jahnsen, R.D., N. Frimodt-Møller, and H. Franzyk, *Antimicrobial activity of peptidomimetics against multidrug-resistant Escherichia coli: a comparative study of different backbones.* Journal of medicinal chemistry, 2012. **55**(16): p. 7253-7261.

92. de la Fuente-Núñez, C., et al., *D-enantiomeric peptides that eradicate wild-type and multidrug-resistant biofilms and protect against lethal Pseudomonas aeruginosa infections.* Chemistry & biology, 2015. **22**(2): p. 196-205.
93. Hilchie, A.L., et al., *Enhanced killing of breast cancer cells by a d-amino acid analog of the winter flounder-derived pleurocidin NRC-03.* Experimental and molecular pathology, 2015. **99**(3): p. 426-434.
94. Whitesides, G.M. and D.J. Lipomi, *Soft nanotechnology: "structure" vs. "function".* Faraday Discussions, 2009. **143**(0): p. 373-384.
95. Whitesides, G.M. and B. Grzybowski, *Self-assembly at all scales.* Science, 2002. **295**(5564): p. 2418-2421.
96. Herzog, R.W., O. Cao, and A. Srivastava, *Two decades of clinical gene therapy–success is finally mounting.* Discovery medicine, 2010. **9**(45): p. 105.
97. Torcato, I.M., et al., *Design and characterization of novel antimicrobial peptides, R-BP100 and RW-BP100, with activity against Gram-negative and Gram-positive bacteria.* Biochimica et Biophysica Acta (BBA)-Biomembranes, 2013. **1828**(3): p. 944-955.
98. Li, A., et al., *Use of Atomic Force Microscopy as a Tool to Understand the Action of Antimicrobial Peptides on Bacteria*, in *Antimicrobial Peptides: Methods and Protocols*, A. Giuliani and A.C. Rinaldi, Editors. 2010, Humana Press Inc: Totowa. p. 235-247.
99. Rosa Teixeira, K.I., et al., *Ultrastructural changes in bacterial membranes induced by nano-assemblies β-cyclodextrin chlorhexidine: SEM, AFM, and TEM evaluation.* Pharmaceutical Development and Technology, 2013. **18**(3): p. 600-608.
100. Zdybicka-Barabas, A., et al., *Synergistic action of Galleria mellonella anionic peptide 2 and lysozyme against Gram-negative bacteria.* Biochimica et Biophysica Acta (BBA)-Biomembranes, 2012. **1818**(11): p. 2623-2635.
101. Roes, S., U. Seydel, and T. Gutsmann, *Probing the properties of lipopolysaccharide monolayers and their interaction with the antimicrobial peptide polymyxin B by atomic force microscopy.* Langmuir, 2005. **21**(15): p. 6970-6978.
102. Chao, Y. and T. Zhang, *Optimization of fixation methods for observation of bacterial cell morphology and surface ultrastructures by atomic force microscopy.* Applied microbiology and biotechnology, 2011. **92**(2): p. 381.
103. Tong, J. and T.J. McIntosh, *Structure of Supported Bilayers Composed of Lipopolysaccharides and Bacterial Phospholipids: Raft Formation and Implications for Bacterial Resistance.* Biophysical Journal, 2004. **86**(6): p. 3759-3771.
104. Stuart, L.J., et al., *Configurational analysis of cyclopropyl fatty acids isolated from Escherichia coli.* Organic letters, 2006. **8**(1): p. 79-81.
105. Paglia, G. and G. Astarita, *Metabolomics and lipidomics using traveling-wave ion mobility mass spectrometry.* Nature Protocols, 2017. **12**(4): p. 797-813.
106. Bishop, D., L. Rutberg, and B. Samuelsson, *The chemical composition of the cytoplasmic membrane of Bacillus subtilis.* The FEBS Journal, 1967. **2**(4): p. 448-453.
107. Clejan, S., et al., *Membrane lipid composition of obligately and facultatively alkalophilic strains of Bacillus spp.* Journal of bacteriology, 1986. **168**(1): p. 334-340.
108. Den Kamp, J.O., I. Redai, and L. Van Deenen, *Phospholipid composition of Bacillus subtilis.* Journal of bacteriology, 1969. **99**(1): p. 298-303.
109. Kawai, F., et al., *Cardiolipin domains in Bacillus subtilis marburg membranes.* Journal of bacteriology, 2004. **186**(5): p. 1475-1483.
110. Hiraoka, S., H. Matsuzaki, and I. Shibuya, *Active increase in cardiolipin synthesis in the stationary growth phase and its physiological significance in Escherichia coli.* FEBS letters, 1993. **336**(2): p. 221-224.
111. Uran, S., et al., *Analysis of phospholipid species in human blood using normal-phase liquid chromatography coupled with electrospray ionization ion-trap tandem mass spectrometry.* Journal of Chromatography B: Biomedical Sciences and Applications, 2001. **758**(2): p. 265-275.

112. Balhara, V., et al., *Membrane selectivity and biophysical studies of the antimicrobial peptide GL13K.* Biochimica Et Biophysica Acta-Biomembranes, 2013. **1828**(9): p. 2193-2203.
113. Epand, R.M. and R.F. Epand, *Lipid domains in bacterial membranes and the action of antimicrobial agents.* Biochimica et Biophysica Acta (BBA)-Biomembranes, 2009. **1788**(1): p. 289-294.
114. Ravi, J., et al., *Supramolecular amphipathicity for probing antimicrobial propensity of host defence peptides.* Physical Chemistry Chemical Physics, 2015. **17**(24): p. 15608-15614.
115. Ryan, L., et al., *Anti-antimicrobial Peptides FOLDING-MEDIATED HOST DEFENSE ANTAGONISTS.* Journal of Biological Chemistry, 2013. **288**(28): p. 20162-20172.
116. Merrifield, R.B., *Solid Phase Peptide Synthesis. I. The Synthesis of a Tetrapeptide.* Journal of the American Chemical Society, 1963. **85**(14): p. 2149-2154.
117. Dirscherl, G. and B. König, *The Use of Solid-Phase Synthesis Techniques for the Preparation of Peptide–Metal Complex Conjugates.* European Journal of Organic Chemistry, 2008. **2008**(4): p. 597-634.
118. Zikos, C., et al., *Comparative evaluation of four trityl-type amidomethyl polystyrene resins in Fmoc solid phase peptide synthesis.* Journal of Peptide Science, 2003. **9**(7): p. 419-429.
119. Pugh, K.C., E.J. York, and J.M. Stewart, *Effects of resin swelling and substitution on solid phase synthesis.* International Journal of Peptide and Protein Research, 1992. **40**(3-4): p. 208-213.
120. Kent, S.B.H., *Chemical Synthesis of Peptides and Proteins.* Annual Review of Biochemistry, 1988. **57**(1): p. 957-989.
121. Kuipers, B.J.H. and H. Gruppen, *Prediction of molar extinction coefficients of proteins and peptides using UV absorption of the constituent amino acids at 214 nm to enable quantitative reverse phase high-performance liquid chromatography-mass spectrometry analysis.* Journal of Agricultural and Food Chemistry, 2007. **55**(14): p. 5445-5451.
122. Ostendorf, F., et al., *How flat is an air-cleaved mica surface?* Nanotechnology, 2008. **19**(30).
123. Javadpour, M.M., et al., *De Novo Antimicrobial Peptides with Low Mammalian Cell Toxicity.* Journal of Medicinal Chemistry, 1996. **39**(16): p. 3107-3113.
124. Op den Kamp, J.A.F., *Lipid Asymmetry in Membranes.* Annual Review of Biochemistry, 1979. **48**(1): p. 47-71.
125. Rigoletto, T.D., et al., *Effects of extrusion, lipid concentration and purity on physico-chemical and biological properties of cationic liposomes for gene vaccine applications.* Journal of Microencapsulation, 2012. **29**(8): p. 759-769.
126. Mingeot-Leclercq, M.P., et al., *Atomic force microscopy of supported lipid bilayers.* Nature Protocols, 2008. **3**(10): p. 1654-1659.
127. Garcia-Manyes, S., G. Oncins, and F. Sanz, *Effect of temperature on the nanomechanics of lipid bilayers studied by force spectroscopy.* Biophysical Journal, 2005. **89**(6): p. 4261-4274.
128. Egawa, H. and K. Furusawa, *Liposome adhesion on mica surface studied by atomic force microscopy.* Langmuir, 1999. **15**(5): p. 1660-1666.
129. Anderson, T.H., et al., *Formation of Supported Bilayers on Silica Substrates.* Langmuir, 2009. **25**(12): p. 6997-7005.
130. Macdonald, P.M. and J. Seelig, *CALCIUM-BINDING TO MIXED PHOSPHATIDYLGLYCEROL-PHOSPHATIDYLCHOLINE BILAYERS AS STUDIED BY DEUTERIUM NUCLEAR-MAGNETIC-RESONANCE.* Biochemistry, 1987. **26**(5): p. 1231-1240.
131. Gaber, B.P. and J.P. Sheridan, *KINETIC AND THERMODYNAMIC STUDIES OF THE FUSION OF SMALL UNILAMELLAR PHOSPHOLIPID-VESICLES.* Biochimica Et Biophysica Acta, 1982. **685**(1): p. 87-93.
132. Alexander, S., et al., *AN ATOMIC-RESOLUTION ATOMIC-FORCE MICROSCOPE IMPLEMENTED USING AN OPTICAL-LEVER.* Journal of Applied Physics, 1989. **65**(1): p. 164-167.
133. Moreno-Herrero, F. and J. Gomez-Herrero, *AFM: Basic Concepts*, in *Atomic Force Microscopy in Liquid*. 2012, Wiley-VCH Verlag GmbH & Co. KGaA. p. 1-34.

134. Hansma, P.K., et al., *TAPPING MODE ATOMIC-FORCE MICROSCOPY IN LIQUIDS.* Applied Physics Letters, 1994. **64**(13): p. 1738-1740.
135. Muller, D.J., et al., *Electrostatically balanced subnanometer imaging of biological specimens by atomic force microscope.* Biophysical Journal, 1999. **76**(2): p. 1101-1111.
136. Zhong, Q., et al., *FRACTURED POLYMER SILICA FIBER SURFACE STUDIED BY TAPPING MODE ATOMIC-FORCE MICROSCOPY.* Surface Science, 1993. **290**(1-2): p. L688-L692.
137. Schaffer, T.E., et al., *Studies of vibrating atomic force microscope cantilevers in liquid.* Journal of Applied Physics, 1996. **80**(7): p. 3622-3627.
138. Minne, S., et al., *NanoScale Quantitative Mechanical Property Mapping Using Peak Force Tapping Atomic Force Microscopy*. Vol. 16. 2010. 464-465.
139. Hu, S.Q., et al., *High-Speed Atomic Force Microscopy and Peak Force Tapping Control*, in *Metrology, Inspection, and Process Control for Microlithography Xxvi, Pts 1 and 2*, A. Starikov, Editor. 2012, Spie-Int Soc Optical Engineering: Bellingham.
140. Su, C., et al., *Quantitative Mechanical Mapping of Biomolecules in Fluid.* MRS Online Proceedings Library, 2010. **1261**: p. null-null.
141. Picas, L., F. Rico, and S. Scheuring, *Direct Measurement of the Mechanical Properties of Lipid Phases in Supported Bilayers.* Biophysical Journal, 2012. **102**(1): p. L1-L3.
142. Pyne, A., et al., *Single-Molecule Reconstruction of Oligonucleotide Secondary Structure by Atomic Force Microscopy.* Small, 2014. **10**(16): p. 3257-3261.
143. Leitner, M., et al., *Increased imaging speed and force sensitivity for bio-applications with small cantilevers using a conventional AFM setup.* Micron, 2012. **43**(12): p. 1399-1407.
144. Ando, T., T. Uchihashi, and N. Kodera, *High-Speed AFM and Applications to Biomolecular Systems*, in *Annual Review of Biophysics, Vol 42*, K.A. Dill, Editor. 2013. p. 393-414.
145. Hoogenboom, B.W., et al., *A Fabry-Perot interferometer for micrometer-sized cantilevers.* Applied Physics Letters, 2005. **86**(7).
146. Yang, J.L., et al., *Miniaturized single-crystal silicon cantilevers for scanning force microscopy.* Applied Physics Letters, 2005. **86**(13).
147. Viani, M.B., et al., *Small cantilevers for force spectroscopy of single molecules.* Journal of Applied Physics, 1999. **86**(4): p. 2258-2262.
148. Fukuma, T., et al., *Atomic-resolution imaging in liquid by frequency modulation atomic force microscopy using small cantilevers with megahertz-order resonance frequencies.* Nanotechnology, 2012. **23**(13).
149. Zhao, M.H., et al., *Ultrasharp and high aspect ratio carbon nanotube atomic force microscopy probes for enhanced surface potential imaging.* Nanotechnology, 2008. **19**(23).
150. Garcia, R. and R. Perez, *Dynamic atomic force microscopy methods.* Surface Science Reports, 2002. **47**(6-8): p. 197-301.
151. Wilson, N.R. and J.V. Macpherson, *Carbon nanotube tips for atomic force microscopy.* Nature Nanotechnology, 2009. **4**(8): p. 483-491.
152. Barnes, J.R., et al., *A FEMTOJOULE CALORIMETER USING MICROMECHANICAL SENSORS.* Review of Scientific Instruments, 1994. **65**(12): p. 3793-3798.
153. Ratcliff, G.C., D.A. Erie, and R. Superfine, *Photothermal modulation for oscillating mode atomic force microscopy in solution.* Applied Physics Letters, 1998. **72**(15): p. 1911-1913.
154. Ramos, D., et al., *Photothermal excitation of microcantilevers in liquids.* Journal of Applied Physics, 2006. **99**(12): p. 8.
155. Yamashita, H., et al., *Tip-sample distance control using photothermal actuation of a small cantilever for high-speed atomic force microscopy.* Review of Scientific Instruments, 2007. **78**(8).
156. Nievergelt, A.P., et al., *High-frequency multimodal atomic force microscopy.* Beilstein Journal of Nanotechnology, 2014. **5**: p. 2459-2467.
157. Adams, J.D., et al., *High-speed imaging upgrade for a standard sample scanning atomic force microscope using small cantilevers.* Review of Scientific Instruments, 2014. **85**(9): p. 7.

158. Lévy, R. and M. Maaloum, *Measuring the spring constant of atomic force microscope cantilevers: thermal fluctuations and other methods.* Nanotechnology, 2002. **13**(1): p. 33.
159. Rakowska, P.D., et al., *Nanoscale imaging reveals laterally expanding antimicrobial pores in lipid bilayers.* Proceedings of the National Academy of Sciences of the United States of America, 2013. **110**(22): p. 8918-8923.
160. Howland, M.C., et al., *Characterization of Physical Properties of Supported Phospholipid Membranes Using Imaging Ellipsometry at Optical Wavelengths.* Biophysical Journal, 2007. **92**(4): p. 1306-1317.
161. Kučerka, N., M.-P. Nieh, and J. Katsaras, *Fluid phase lipid areas and bilayer thicknesses of commonly used phosphatidylcholines as a function of temperature.* Biochimica et Biophysica Acta (BBA) - Biomembranes, 2011. **1808**(11): p. 2761-2771.
162. Jacobson, K. and D. Papahadjopoulos, *Phase transitions and phase separations in phospholipid membranes induced by changes in temperature, pH, and concentration of bivalent cations.* Biochemistry, 1975. **14**(1): p. 152-161.
163. Segrest, J.P., et al., *Amphipathic helix motif: Classes and properties.* Proteins: Structure, Function, and Bioinformatics, 1990. **8**(2): p. 103-117.
164. Tossi, A., L. Sandri, and A. Giangaspero, *Amphipathic, alpha-helical antimicrobial peptides.* Biopolymers, 2000. **55**(1): p. 4-30.
165. J. Bond, P. and S. Khalid, *Antimicrobial and Cell-Penetrating Peptides: Structure, Assembly and Mechanisms of Membrane Lysis via Atomistic and Coarse-Grained Molecular Dynamic Simulations.* Protein and Peptide Letters, 2010. **17**(11): p. 1313-1327.
166. Ryadnov, M.G., *Biofunctional peptide design*, in *Amino Acids, Peptides and Proteins: Volume 38*. 2014, The Royal Society of Chemistry. p. 79-121.
167. Bulheller, B.M., A. Rodger, and J.D. Hirst, *Circular and linear dichroism of proteins.* Physical Chemistry Chemical Physics, 2007. **9**(17): p. 2020-2035.
168. Greenfield, N.J., *Using circular dichroism spectra to estimate protein secondary structure.* Nature Protocols, 2006. **1**(6): p. 2876-2890.
169. Hicks, M.R., J. Kowalski, and A. Rodger, *LD spectroscopy of natural and synthetic biomaterials.* Chemical Society Reviews, 2010. **39**(9): p. 3380-3393.
170. Berney, M., et al., *Assessment and interpretation of bacterial viability by using the LIVE/DEAD BacLight Kit in combination with flow cytometry.* Applied and environmental microbiology, 2007. **73**(10): p. 3283-3290.
171. Hasselmann, C., *Determination of minimum inhibitory concentrations (MICs) of antibacterial agents by broth dilution.* Clinical Microbiology and Infection, 2003. **9**(8).
172. Ebbensgaard, A., et al., *Comparative Evaluation of the Antimicrobial Activity of Different Antimicrobial Peptides against a Range of Pathogenic Bacteria.* Plos One, 2015. **10**(12).
173. Ryadnov, M.G., et al., *RE Coil: An Antimicrobial Peptide Regulator.* Angewandte Chemie-International Edition, 2009. **48**(51): p. 9676-9679.
174. Whitmore, L. and B.A. Wallace, *Protein secondary structure analyses from circular dichroism spectroscopy: methods and reference databases.* Biopolymers, 2008. **89**(5): p. 392-400.
175. Brattwall, C.E., P. Lincoln, and B. Nordén, *Orientation and conformation of cell-penetrating peptide penetratin in phospholipid vesicle membranes determined by polarized-light spectroscopy.* Journal of the American Chemical Society, 2003. **125**(47): p. 14214-14215.
176. Li, L., I. Vorobyov, and T.W. Allen, *The Different Interactions of Lysine and Arginine Side Chains with Lipid Membranes.* The Journal of Physical Chemistry B, 2013. **117**(40): p. 11906-11920.
177. Yoo, J. and Q. Cui, *Does Arginine Remain Protonated in the Lipid Membrane? Insights from Microscopic pK(a) Calculations.* Biophysical Journal, 2008. **94**(8): p. L61-L63.
178. Strömstedt, A.A., et al., *Interaction between amphiphilic peptides and phospholipid membranes.* Current Opinion in Colloid & Interface Science, 2010. **15**(6): p. 467-478.
179. Edelstein, M.L., M.R. Abedi, and J. Wixon, *Gene therapy clinical trials worldwide to 2007 - an update.* Journal of Gene Medicine, 2007. **9**(10): p. 833-842.

180. Lamarre, B. and M.G. Ryadnov, *Self-Assembling Viral Mimetics: One Long Journey with Short Steps.* Macromolecular Bioscience, 2011. **11**(4): p. 503-513.
181. Zuber, G., et al., *Towards synthetic viruses.* Advanced Drug Delivery Reviews, 2001. **52**(3): p. 245-253.
182. Yacoby, I. and I. Benhar, *Antibacterial nanomedicine.* Nanomedicine, 2008. **3**(3): p. 329-341.
183. Kanyshkova, T.G., V.N. Buneva, and G.A. Nevinsky, *Lactoferrin and its biological functions.* Biochemistry-Moscow, 2001. **66**(1): p. 1-7.
184. Schibli, D.J., P.M. Hwang, and H.J. Vogel, *The structure of the antimicrobial active center of lactoferricin B bound to sodium dodecyl sulfate micelles.* Febs Letters, 1999. **446**(2-3): p. 213-217.
185. Douglas, T. and M. Young, *Viruses: Making friends with old foes.* Science, 2006. **312**(5775): p. 873-875.
186. Cochran, A.G., N.J. Skelton, and M.A. Starovasnik, *Tryptophan zippers: Stable, monomeric beta-hairpins.* Proceedings of the National Academy of Sciences of the United States of America, 2001. **98**(10): p. 5578-5583.
187. Arnott, S., S.D. Dover, and A. Elliott, *Structure of β-poly-l-alanine: Refined atomic co-ordinates for an anti-parallel beta-pleated sheet.* Journal of Molecular Biology, 1967. **30**(1): p. 201-208.
188. Huang, H.W., *Action of antimicrobial peptides: Two-state model.* Biochemistry, 2000. **39**(29): p. 8347-8352.
189. Johnson, J.E. and J.A. Speir, *Quasi-equivalent viruses: a paradigm for protein assemblies11Edited by T. Richmond.* Journal of Molecular Biology, 1997. **269**(5): p. 665-675.
190. Perlmutter, J. and M. Hagan, *Mechanisms of Virus Assembly.* Annual Review of Physical Chemistry, 2015. **66**(1): p. 217-239.
191. Caspar, D.L.D. and A. Klug, *Physical principles in the construction of regular viruses.* Cold Spring Harbor Symposia on Quantitative Biology, 1962. **27**: p. 1-24.
192. Bale, J.B., et al., *Accurate design of megadalton-scale two-component icosahedral protein complexes.* Science, 2016. **353**(6297): p. 389-394.
193. Matsuura, K., *Construction of spherical virus-inspired peptide nanoassemblies.* Polym J, 2012. **44**(6): p. 469-474.
194. Lupas, A., *Coiled coils: New structures and new functions.* Trends in Biochemical Sciences, 1996. **21**(10): p. 375-382.
195. Lupas, A.N. and J. Bassler, *Coiled Coils - A Model System for the 21st Century.* Trends in Biochemical Sciences, 2017. **42**(2): p. 130-140.
196. Aupič, J., et al., *Towards designing new nano-scale protein architectures.* Essays In Biochemistry, 2016. **60**(4): p. 315-324.
197. Ryan, L., et al., *Anti-antimicrobial Peptides FOLDING-MEDIATED HOST DEFENSE ANTAGONISTS.* Journal of Biological Chemistry, 2013. **288**(28): p. 20162-20172.
198. Ebenhan, T., et al., *Antimicrobial Peptides: Their Role as Infection-Selective Tracers for Molecular Imaging.* BioMed Research International, 2014. **2014**: p. 867381.
199. Su, J.Y., R.S. Hodges, and C.M. Kay, *Effect of Chain Length on the Formation and Stability of Synthetic .alpha.-Helical Coiled Coils.* Biochemistry, 1994. **33**(51): p. 15501-15510.
200. Fjell, C.D., et al., *Designing antimicrobial peptides: form follows function.* Nat Rev Drug Discov, 2012. **11**(1): p. 37-51.
201. Monera, O.D., et al., *Formation of parallel and antiparallel coiled-coils controlled by the relative positions of alanine residues in the hydrophobic core.* Journal of Biological Chemistry, 1996. **271**(8): p. 3995-4001.
202. Nagano, N., M. Ota, and K. Nishikawa, *Strong hydrophobic nature of cysteine residues in proteins.* FEBS letters, 1999. **458**(1): p. 69-71.
203. Noble, J.E., et al., *A De Novo Virus-Like Topology for Synthetic Virions.* Journal of the American Chemical Society, 2016. **138**(37): p. 12202-12210.

204. Brych, S.R., et al., *Characterization of antibody aggregation: Role of buried, unpaired cysteines in particle formation.* Journal of Pharmaceutical Sciences, 2010. **99**(2): p. 764-781.
205. Corona, F. and J. Martinez, *Phenotypic Resistance to Antibiotics.* Antibiotics, 2013. **2**(2): p. 237.
206. Butler, M.S. and M.A. Cooper, *Antibiotics in the clinical pipeline in 2011.* Journal of Antibiotics, 2011. **64**(6): p. 413-425.
207. Fox, J.L., *Antimicrobial peptides stage a comeback.* 2013. **31**: p. 379.
208. Spiteri, K. *Effect Dressing Type Wound Healing*. November 2013.
209. Jiang, Q., et al., *Comparative effectiveness of different wound dressings for patients with partial-thickness burns: study protocol of a systematic review and a Bayesian framework network meta-analysis.* BMJ Open, 2017. **7**(3).
210. Mudge E, O.H. *Wound infection & Pain management*. 2010. **1**.
211. By Geoffrey C Gurtner, P.C.N., *Plastic Surgery E-Book: Volume 1 Principles*. 2018, London: Elsevier Health Sciences.
212. *Guidance for industry and FDA staff [electronic resource] : how to write a request for designation (RFD)*, ed. F. United States and P. Drug Administration. Office of Combination. 2005, Rockville, MD: U.S. Dept. of Health and Human Services, Food and Drug Administration, Office of the Commissioner, Office of Combination Products.
213. Drew, P., J. Posnett, and L. Rusling, *The cost of wound care for a local population in England.* Int Wound J, 2007. **4**(2): p. 149-55.
214. Posnett, J., et al., *The resource impact of wounds on health-care providers in Europe.* J Wound Care, 2009. **18**(4): p. 154-161.
215. Borda, L.J., F.E. Macquhae, and R.S. Kirsner, *Wound Dressings: A Comprehensive Review.* Current Dermatology Reports, 2016. **5**(4): p. 287-297.
216. Wild, S., et al., *Global prevalence of diabetes: estimates for the year 2000 and projections for 2030.* Diabetes Care, 2004. **27**(5): p. 1047-53.
217. Gwak, J.H. and S.Y. Sohn, *Identifying the trends in wound-healing patents for successful investment strategies.* PLOS ONE, 2017. **12**(3): p. e0174203.
218. research, c., *Wound Care Market By Product Type, Application - Growth, Share, Opportunities & Competitive Analysis, 2016 - 2022*. 2016, credence research: USA.
219. Intelligence, M., *Europe Wound Management Market - Industry Analysis and Market Forecast (2017 - 2022)*. 2017, careers@mordorintelligence.com: USA.
220. Excellence, N.I.f.H.a.C., *Chronic wounds: advanced wound dressings and antimicrobial dressings*, D.o. Health, Editor. 2016, National Institute for Health and Care Excellence: UK.
221. Leaper, D.J., *Silver dressings: their role in wound management.* Int Wound J, 2006. **3**(4): p. 282-94.
222. Dhivya, S., V.V. Padma, and E. Santhini, *Wound dressings – a review.* BioMedicine, 2015. **5**(4): p. 22.
223. LaRiviere, C.A., A.B. Goldin, and J. Avansino, *Silver Toxicity With the Use of Silver-Impregnated Dressing and Wound Vacuum-Assisted Closure in an Immunocompromised Patient.* The Journal of the American College of Certified Wound Specialists, 2011. **3**(1): p. 8-12.
224. Paddle-Ledinek, J.E., Z. Nasa, and H.J. Cleland, *Effect of Different Wound Dressings on Cell Viability and Proliferation.* Plastic and Reconstructive Surgery, 2006. **117**(7S): p. 110S-118S.
225. Atiyeh, B.S., et al., *Effect of silver on burn wound infection control and healing: Review of the literature.* Burns, 2007. **33**(2): p. 139-148.
226. EDWARDS, B.S.G.J.V., *textile materials and structures for wound care products* in *Advanced Textiles for Wound Care*, S. Rajendran, Editor. 2009, Elsevier: USA.
227. Antunes, L., et al., *Bioactive microsphere-based coating for biomedical-textiles with encapsulated antimicrobial peptides (AMPs).* Ciência & Tecnologia dos Materiais, 2014. **26**(2): p. 118-125.

Appendices

Appendix 1—Amino Acids

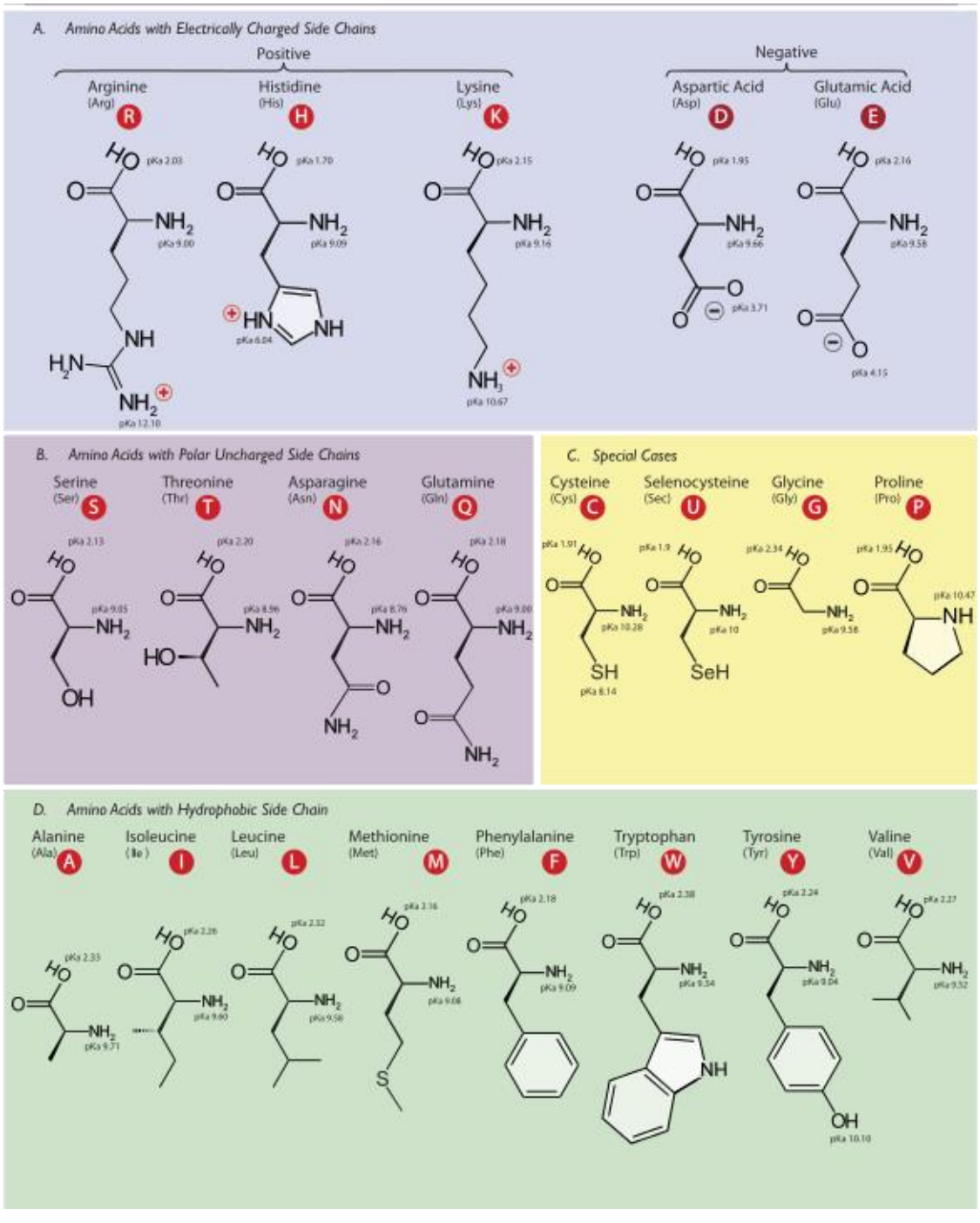

Amino acids structures prepared by Dan Cojocari working at Princess Margaret Cancer Centre, University of Toronto. Source: Wikipedia.

Appendix 2—Risk Register

Risk Area	Risk Description	Likelihood	Impact	Risk Score	Mitigation Strategies
Manufacturing	Manufacturing bottleneck leads to short distribution capacity.	L	H	L	• Expanding the company if the manufacturing model was successful. • Out-source from more than one company
Manufacturing	Dependence on quality control of suppliers could end up with low quality products.	L	H	L	• Dealing only with trusted companies which perform GMP. • Safety and quality control checks before accepting materials into the production line
Manufacturing/ Market	Staff may be poached by competitors	M	H	M	• Pay bonuses based on performance. • Include perks such as providing health insurance. • Have back-up trained staffs for critical roles
Manufacturing/ Market	Staff may leave to pursue different/competing projects	M	H	H	• Provide staff with company shares. • Implement strong contracts with confidentiality agreements.
Market	Advances in other wound treatment therapy	L	M	L	• The key challenge is the bacterial resistance which is not likely to be

					overcome easily with other therapy in a period of 5 years.
Regulatory	Regulatory issues (Clinical phase 2 and on-going FDA check during the manufacturing)	H	H	H	• Have an experienced QC team and Chief medical officer to mitigate problems and ensure maintaining high standards. • Follow all guidelines established by regulatory agencies. • Collaborate with consultant companies.
Finance	Unforeseen cost	H	M	H	• Allocate a budget in business plan for unforeseen costs.
Finance	Insufficient funding	M	H	M	• Adjust the size of spinning company. • Make a thorough business and economy plan. • Get multiple funding cooperation.
Finance	Misuse of available cash	H	M	M	• Filing documents of other quotes for all purchases. • Hiring experienced financial team and accountants.

END